INAUGURAL - DISSERTATION

A CCD BASED CURVATURE WAVEFRONT SENSOR FOR ADAPTIVE OPTICS IN ASTRONOMY

zur
Erlangung der Doktorwürde
der Naturwissenschaftlichen-Mathematischen Gesamtfakultät
der Ruprecht-Karls-Universität Heidelberg

Vorgelegt
von
Reinhold Josef Dorn
aus München

Tag der mündlichen Prüfung: 21. November 2001

DISSERTATION

submitted to the
Combined Faculties for Natural Sciences and Mathematics
of the Ruperto – Carola University of Heidelberg, Germany
for the degree of
Doctor of Natural Sciences

presented by

Reinhold Josef Dorn

born in Munich

Oral examination: 21. November 2001

A CCD BASED CURVATURE WAVEFRONT SENSOR

FOR ADAPTIVE OPTICS IN ASTRONOMY

Referees: Professor Dr. Immo Appenzeller
                Professor Dr. Josef Bille

ZUSAMMENFASSUNG

Adaptive Optik (AO) ist eine Technik, um Störungen in der Abbildung von Objekten im Teleskop auszugleichen. Diese Störungen werden von Fluktuationen des Brechungsindexes in der Erdatmosphäre hervorgerufen. Zum Messen dieser Störungen gibt es eine Reihe verschiedener Wellenfrontsensoren. Einer davon ist der "Curvature"- Wellenfrontsensor, was soviel wie "Krümmungs"- Wellenfrontsensor bedeutet. An der Europäischen Südsternwarte (ESO) in Garching werden für das Very Large Telescope (VLT) und das VLT Interferometer (VLTI) eine Reihe von adaptiven Optiksystemen entwickelt, die den Curvature - Wellenfrontsensor verwenden. Bisher wurden in Curvature AO-Systemen Avalanche Photodioden (APDs) als Detektoren verwendet, da sehr kurze Belichtungszeiten (200 Mikrosekunden) und ein sehr niedriges Ausleserauschen des Detektors nötig sind.

Aufgrund von Fortschritten in der Herstellungstechnologie von Charge Coupled Devices (CCDs) entwickelten wir ein spezielles CCD und untersuchten dessen Leistungsfähigkeit für ein 60 Element Curvature AO System, das mit sehr schwachen Lichtsignalen arbeitet. Hier wurde erstmals ein CCD als Wellenfrontsensor verwendet. Diese Dissertation zeigt, daß ein CCD annähernd die gleiche Leistungsfähigkeit wie APDs bietet, jedoch zu einem Bruchteil der Kosten und geringerer Komplexität. Weiter hat das CCD eine höhere Quantenausbeute und einen größeren dynamischen Bereich als APDs. Ein Ausleserauschen von weniger als 1,5 Elektronen bei 4000 Bildern pro Sekunde wurde erreicht. Für AO Systeme, die Wellenfrontkorrekturen mit vielen Elementen durchführen, können dünne, von hinten beleuchtete CCDs, APDs als bessere Detektoren ersetzen.

Diese Dissertation präsentiert das Konzept, das Design und die Bestimmung der Leistungsfähigkeit dieses CCDs. Erste (von vorne beleuchtete) CCDs wurden erfolgreich getestet und die Leistungsfähigkeit in einem Laborexperiment nachgewiesen.

ABSTRACT

Adaptive Optics (AO) is a technique for compensating the distortions introduced by atmospheric turbulence in astronomical imaging. To measure the distortions a wavefront sensor is needed. There are a number of fundamentally different types of wavefront sensors, one of which is the curvature wavefront sensor. At the European Southern Observatory (ESO) in Garching, Germany, several adaptive optics systems using curvature wavefront sensors are being developed for the Very Large Telescope (VLT) and the VLT interferometer (VLTI). Curvature AO-systems have traditionally used avalanche photodiodes (APDs) as detectors due to strict requirements of very short integration times (200 microsec) and very low readout noise.

Advances in charge-coupled device (CCD) technology motivated an investigation of the use of a specially designed CCD as the wavefront sensor detector in a 60-element curvature AO system. A CCD has never been used before as the wavefront sensor in a low light level curvature adaptive optics system. This thesis shows that a CCD can achieve nearly the same performance as APDs at a fraction of the cost and with reduced complexity for high order wavefront correction. Moreover the CCD has higher quantum efficiency and a greater dynamic range than APDs. A readout noise of less than 1.5 electrons at 4000 frames per second was achieved. A back-illuminated thinned version of this CCD can replace APDs as the best detector for high order curvature wavefront sensing.

This thesis presents the concept, the design and the evaluation of the CCD. The first frontside devices were successfully evaluated and the performance of the detector was proven in a laboratory experiment.

TABLE OF CONTENTS

LIST OF FIGURES AND TABLES

Chapter 5

Chapter 6

Chapter 7

Appendices

ACKNOWLEDGMENTS

Chapter 1

INTRODUCTION

The quality of images and spectra taken at ground-based astronomical observatories is degraded by distortions in the Earth's atmosphere. Rather than achieving diffraction-limited resolution, large ground-based telescopes at the best sites seldom achieve image quality better than the diffraction-limit of a 20 cm diameter telescope (0.5 arcsec in the visible, 0.5 µm wavelength). This blurring, which is due to temperature inhomogeneities in the atmosphere, is called atmospheric **seeing**. If the seeing could be eliminated, an 8 m telescope would be able to achieve 0.013 arcsec resolution in the visible and 0.057 arcsec resolution in the K-band of the infrared (2.2 µm). Compensation of the atmospheric seeing can be achieved using the technology of **adaptive optics** (AO), [Babcock, 1953], a technique which is being pursued by every major ground-based observatory. A good general reference is a recent book published by F. Roddier [Roddier, 1999].

1.1 Adaptive optics in Astronomy

As it is more difficult to correct distortions at shorter wavelengths, astronomical observatories are presently only attempting to implement AO for infrared wavelengths. Atmospheric turbulence and especially its high spatial frequencies have weaker effect on longer wavelengths for adaptive optics correction. Also a larger isoplanetic angle at infrared wavelength, 25 arcsec at 2500 nm compared to 5 arcsec for visible wavelength, makes AO correction easier than at visible wavelength [Roddier, 1999].

The main components for an adaptive optics system are: (1) a tip/tilt mirror to correct the large image translations that can be not corrected with the dynamic range of the deformable mirror, (2) the deformable mirror to correct the distortions, (3) a real time computer for the reconstruction of the wavefront and calculating the algorithms needed to send signals to the correcting adaptive optics elements, (4) a wavefront sensor that measures the atmospheric distortions using the light either from a natural or laser guide star. These modules produce a corrected beam that is imaged by the science camera usually detecting the light at infrared wavelength. Figure 1 presents a simplified schematic of an adaptive optics system.
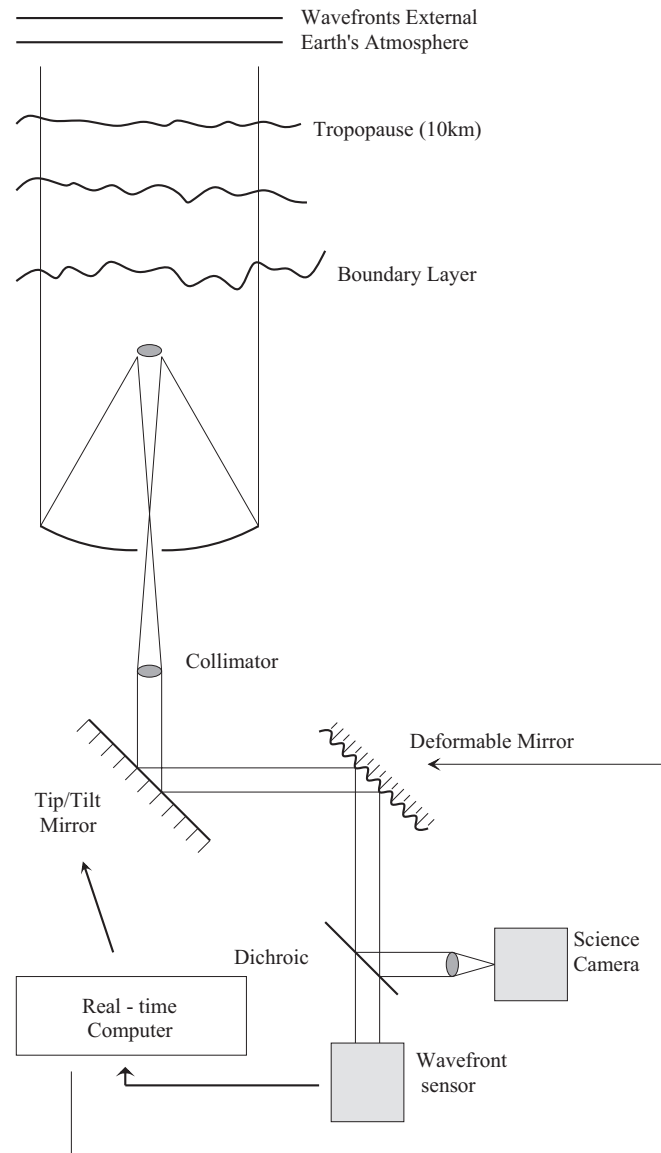
Figure 1-1 Schematic diagram of an adaptive optics system.

Today a number of astronomical AO systems are routinely working on 4-m class or larger telescopes and a short overview of the most successful systems is as follows:

o   The ADONIS system on the ESO-La Silla 3.6 m telescope was one of the first Shack Hartmann AO-systems [Merkle et al., 1989].   The wavefront sensor channel is equipped with two intensified cameras, one for low flux and one for high flux natural guide star sources. The high flux Shack Hartmann wavefront sensor is a intensified Reticon chip and the low flux Shack Hartmann, dedicated to reference stars between 8 and 13, is an Electron Bombarded CCD (EBCCD). Strehl ratios of 10 to 50% are achieved.

o   The 19 element Adaptive Optics Bonnette (AOB), also called PUEO, the curvature system installed on the 3.6-m CFH telescope (Mauna Kea/Hawaii) and the 36 element Hokupa'a system, observing at the University of Hawaii 2.2 m telescope and on the 8 m Gemini North telescope. These systems use avalanche photodiodes from Perkin Elmer (formerly EG&G) as the wavefront sensor [Roddier and Rigaut, 1999].

o   ADOPT on the 100 inch Hooker telescope on Mount Wilson. A Shack Hartmann 240 subaperture system achieving Strehl ratios of 10 to 20%. The wavefront sensor is a high frame rate, small format, low noise CCD designed by James Janesick. It is a front-side illuminated 32 x 32 x 2 frame-transfer device with poor quantum efficiency of 40% at 600 nm and 32 skipper output amplifiers.

o   The Shack Hartmann system ALFA with its 97 element actuator deformable mirror on the Calar Alto 3.5 m telescope, the first one which used "routinely" a laser guide star (LGS) (not operating presently). The wavefront sensor is a thinned MIT Lincoln Lab 64 x 64 frame transfer CCD with a frame rate of more than 1000 frames per second, with readout noise of 3.5 electrons and a quantum efficiency of 80% at 600 nm [Kasper et al., 2000].

o   The adaptive optics program of Lawrence Livermore National Laboratory (LLNL) at the 3.5 m Shane telescope (Lick Observatory). In the past this system operated with natural guide stars only, but now features a LGS. The wavefront sensor camera, built by Adaptive Optics Associates, uses the same fast-framing low-noise 64 x 64 CCD, designed by MIT/Lincoln Laboratory as ALFA. This CCD camera has a read noise of 7 electrons per pixel at a readout rate of 1200 frames per second. A separate tip-tilt sensor is necessary when the wavefront sensing is performed using the laser guide star. The tip-tilt sensor, designed and built at LLNL, uses four photon-counting avalanche photo-diodes operated as a quad cell.

o   The Keck I and II AO facilities at Mauna Kea with a wavefront sensor from Adaptive Optics Associates with a MIT/LL 64 x 64 pixel CCD, 21 µm pixels, 6-7 e-/pixel readout noise and frame rate selectable between 80 and 670 Hz.

1.2 Adaptive optics at the European Southern Observatory

The systems at ESO will include the NAOS adaptive optics system and systems for the instruments SINFONI and CRIRES. Up to 4 curvature systems for the ESO VLT interferometer (VLTI). Descriptions of those systems can be found in more detail on the ESO web pages.

The NAOS adaptive optics system, to be installed at the Nasmyth focus of the VLT, is the AO system for the infrared camera of CONICA. NAOS has been designed and manufactured by a French consortium; the visible wavefront sensor has been developed by ESO. A deformable mirror with 185 useful actuators compensates the atmospheric disturbance measured by two Shack Hartman wavefront sensors. One covers the visible wavelengths and the other one the infrared [Rousset et al, 2000]. The visible WFS for NAOS uses a 128 x 128 pixels split frame transfer low noise CCD fabricated by Marconi. 16 output ports allow a high frame rate (500 frames/sec) and low noise (3 electrons at a conversion factor of 0.3 electrons/ADU), [Feutrier and Dorn, 2000].

ESO is also developing a 60 element curvature AO systems called MACAO, [Donaldson et al., 2000]. This system is planned for several instruments (SINFONI, CRIRES) and up to four curvature systems are planned for the (VLTI). For the VLTI, the systems are operating at the Coudé foci feeding the VLTI delay lines with a corrected IR beam with up to 50% Strehl at 2.2 microns. The first MACAO-VLTI unit is scheduled for installation in Paranal in 2003 and the final unit will be installed by early 2004. The

corrective optics consists of a deformable mirror with 60 actuators mounted on a tip/tilt stage situated at mirror 8 in the Coudé train. The curvature wavefront sensor is based on a 60 element lenslet array feeding fibers connected to 60 APD modules.

MACAO is an ESO in-house developed curvature adaptive optics system and the design of the detector presented in this thesis is based on this development.

1.3 Wavefront sensor requirements

The most precious signal in an AO system is the signal detected by the wavefront sensor (WFS). In many cases, the quality of the WFS signal determines the quality of the entire AO system operation. The WFS is located in the light path after the deformable mirror (DM), so that the WFS measures the residual wavefront distortion. The WFS signal is processed by the real-time computer and commands are sent to the DM so as to produce a flat wavefront at the WFS. Since the atmospheric distortion changes on timescales of 10 to 30 msec, the WFS must measure the wavefront distortion in a very short time; exposure times as short as 1 msec are desired. Due to the short exposure time, there is a limited number of photons available to the WFS in each frame, especially for the distant and faint objects that are studied by large telescopes. Thus, the primary limit to the performance of an adaptive optics system is the photon noise of the signal at the wavefront sensor. Ideally, the only limit to the WFS performance is photon noise. Readout noise of the WFS should be minimized, and if possible, completely eliminated.   Thus, the two most basic requirements for adaptive optics wavefront sensors are:

o   High quantum efficiency
o   Low readout noise

There are two other very important requirements for wavefront sensors:

o   Ability to take very short exposures
o   Fast readout speed

Ideally, the only phase lag in an AO system is the time needed for the WFS exposure. For photon counting detectors, such as avalanche photodiodes (APDs), there is effectively no delay due to readout time. Thus, when designing a CCD for wavefront sensing, it is very important to reduce the readout time so as to minimize phase delay errors.

There are several ways to measure the wavefront distortions, including Shack-Hartmann, shearing and Mach-Zender interferometry, pyramidic and curvature [Rousset 1999, Tyson 1991, Ragazzoni 1996, Ragazzoni and Farinato 1999]. At this time, only two approaches are widely used for WFS in ground-based astronomical AO systems: Shack-Hartmann and curvature. Pyramidic wavefront sensors are still in the experimental phase.

To understand the requirements and basic principles of wavefront sensors one first needs to understand the fundamental concepts of atmospheric turbulence, the basic properties, common functions and statistics used in the modal control approach. These will be discussed briefly in the following chapter.

C h a p t e r   2

FUNDAMENTAL CONCEPTS

A keypoint in the development of new concepts and methods for adaptive optics systems is a basic understanding of the effects and the influence of turbulence on the optical image formation. Wavefront errors which change slowly, i.e. time scales longer then several units, are usually compensated by **active optics** implemented on most modern telescopes. One of the first fully active telescope used in astronomy, the ESO 3.5 m New Technology Telescope (NTT), entered into operation at La Silla Observatory in Chile in 1989.

Active optics is very much at the heart of the segmented 10 m Keck primary mirror, in operation since 1992 on Mauna Kea, Hawaii and all four 8.2 m mirrors at the Very Large Telescope in Paranal. This compensation is usually done by active control of the primary mirror and optimized automatically by a constant adjustments of in-built corrective optical elements operating at fairly low temporal frequency ~ 0.05 Hz or less [Noethe, 2000]. Active optics compensates deformation of the optics due to gravity as well as residual aberrations in the optical path due to non-perfect optics.

2.1 Seeing and angular resolution

Ground based telescopes suffer even under the best seeing conditions from the effects of atmospheric turbulence that cause a wavefront degradation. We can observe the effect of distortions even with the naked eye at night. The stars twinkle due to intensity fluctuations. This phenomenon is known as **scintillation**. In space, where the light does not have to travel though the atmosphere, the image of a point source is limited only by the optics of the telescope and the diffraction of light. A perfect telescope would have a theoretical **diffraction limited angular resolution** of

$$\Delta\alpha = 1.22\frac{\lambda}{D},\qquad(2\text{-}1)$$

where λ is the wavelength and D the diameter of the telescope. $\Delta\alpha$ is the radius of the first dark ring of the airy disk in radians. Atmospheric turbulence degrades the image primarily by phase fluctuation over the aperture of the telescope. For short exposures these aberrations fluctuating will cause the light to scatter and form a **speckle pattern** in the image plane as seen in Figure 2-2, where the individual speckles are diffraction-limited.

5

Figure 2-1 Diffraction-limited PSF of an 8 m telescope at a wavelength of 1000 nm with 0.65"
seeing.

Figure 2-2 Speckle pattern of an 8 m telescope at a wavelength of 1000 nm with 0.65" seeing.
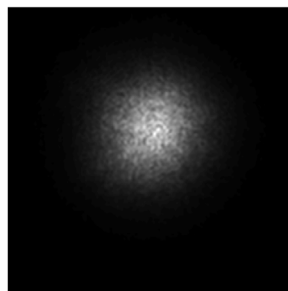
Figure 2-3 Seeing disk of an 8 m telescope at a wavelength of 1000 nm with 0.65" seeing.

Over a long exposure, this speckle pattern evolves and a point source is blurred into
a fuzzy disk called the **seeing disk**, which can be 10 to 100 times larger in diameter than the
diffraction limit, depending on the seeing conditions. Figure 2-3 shows a seeing disk for an
8 m telescope operating at a wavelength of 1000 nm with 0.65" seeing. This condition is

valid for all telescope sizes and larger telescopes are limited in resolution not by diffraction, but by the turbulence of the atmosphere.

Due to the turbulence, the angular resolution is described as:

$$\Delta\alpha' = 1.22 \frac{\lambda}{r_0(\lambda)},$$
(2.2)

where $\Delta\alpha'$ is the seeing angle and r_0 is the Fried parameter, which is the phase coherence length across the turbulent wavefront, i.e. the distance over which the wavefront is not significantly perturbed. The larger r_0, the better the seeing limited resolution. The Fried parameter is an important parameter for a modeling the turbulent wavefront and will be explained in more detail in the next section.

2.2 Imaging through atmospheric turbulence and the Fried parameter

There are many models describing atmospheric turbulence, but the most commonly used one is the **structure function** introduced by Kolmogorov in 1961 [Kolmogorov, 1961]. These structure functions describe the random functions used in turbulence theory.

Light from a point source or star traveling to the earth, due to the large distance, preserves a plane wavefront. In the earths atmosphere these wavefronts are distorted randomly by moving through different layers or cells of air with differences in the refractive index. This is illustrated in the Figure 2-4. These variations in the refractive index arise from variations in density, which are caused by temperature fluctuations [Roddier, 1999].

The structure function $D(r)$, which describes the properties of the atmospheric turbulence gives the variation in refractive index (n) between two points on the wavefront separated by a distance (r_1-r_2) and can be written as following:

$$D_n(r) = \left\langle \left| n(r_1) - n(r_2) \right|^2 \right\rangle = C_n^2 r^{2/3},$$
(2-3)

where the result $C_n^2 r^{2/3}$ was derived by Obukhov in 1949 and is known as Obukhov´s law [Obukhov, 1949].

Scintillation contributes much less to the image degradation than distortions of the phase of the wavefront. The vector r represents the positions of those points in the 3 dimensions. The phase structure function $D_\phi(r)$ across the diameter of the telescope is given by

$$D_\phi(r) = 6.88 \left(\frac{r}{r_0} \right)^{5/3} rad^2,$$
(2-4)

in the Kolmogorov model. This equation uses the Fried parameter as introduced by Fried in 1965 [Fried, 1965].

The Fried parameter r_0 is given by

$$r_0(\lambda,\xi) = 0.185 \lambda^{6/5} \cos^{3/5} \xi \left(\int C_n^2(h)dh \right)^{-3/5},$$
(2-5)

also written as

$$r(\lambda) = \left(\frac{\lambda}{\lambda_0} \right)^{6/5} r_0.$$
(2-6)

Atmospheric Turbulence
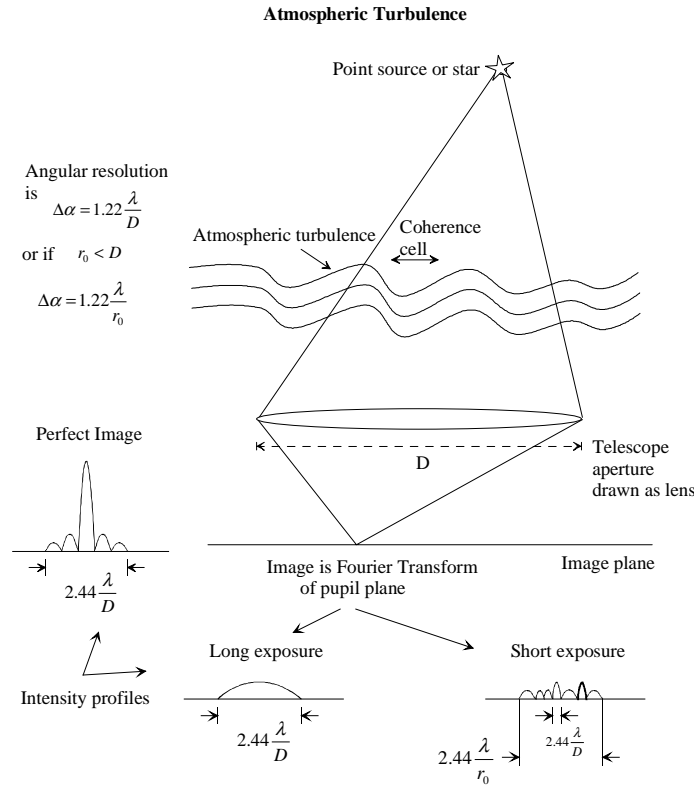
Figure 2-4 Resolution of a telescope with turbulence.

where λ is the wavelength of the light, ξ the zenith distance (angle of observation measured from the zenith) and C_n the structure constant for the refractive index variations which is integrated through the turbulence, i.e. the optical path through the turbulence.   The refractive index is also a function of altitude or height above the ground and is explained in more detail in a paper by Fried [Fried, 1966].

At optical wavelength (500 nm), the Fried parameter is typically around 10 to 15 cm, but also much larger values are possible at excellent sites like Paranal and Mauna Kea. Referring to Figure 2-4 if the Fried parameter is bigger than the diameter of the telescope aperture, the resolution is not affected by atmospheric turbulence.   For 8 or 10 m class telescopes a Fried parameter of 0.5 m would be much smaller than the telescope.   Since r_0 increases as $\lambda^{6/5}$, image quality is better at longer wavelengths (Roddier, 1999).

Equation (2-3) describes the spatial distribution of the turbulence.   For a further analysis one also needs to know how fast these fluctuation evolve with time.   The speed of the turbulence varies with height; the temporal variations are often described by an average velocity v_a, which is typically around 10 m per second.   The temporal variations τ_0 are given by

$$\tau_0 \approx 0.314 \frac{r_0}{v_a} , \qquad (2\text{-}7)$$

which are on the order of a few milliseconds.   These temporal variations are also called the **coherence time** τ_0.   Roughly τ_0 is the time in which the mean RMS phase-variation at a

point is one radian. To quantify the relationship between the phase aberrations and the image quality the Strehl ratio is used.

2.3 The Strehl ratio (SR)

To quantify the performance of an AO-system, the **Strehl ratio** of the point spread function (PSF) is used. The PSF $s(\vec{x})$ is interpreted as the image plane intensity distribution that results from imaging a point source. The point spread function is a very useful performance measure since the resolution of an adaptive optics system be determined directly from the width of the PSF (if the signal is infinite). The Strehl ratio is defined as the ratio of the central intensities of the aberrated PSF and the diffraction-limited PSF of the instrument.

$$ SR = \frac{s(\vec{x}=0)_{aberrated}}{s(\vec{x}=0)_{diffraction\lim ited}} \ , \qquad\qquad (2\text{-}8) $$

where $s(\vec{x})$ is the intensity point spread function and $\vec{x}$ defines a point in the image plane [Roggemann and Welsh, 1996].

Strehl ratios can be measured instantaneously or, averaged over time, the integrated Strehl. The instantaneous Strehl is the Strehl ratio of a short exposure PSF (such as the speckle pattern seen in Figure 2-2), while the integrated Strehl is the Strehl ratio of a long exposure PSF (such as Figure 2-3). Usually long exposures are used to see fainter objects. Comparing the instantaneous and integrated Strehl will however prove to reveal some interesting information about the performance of the AO-system. Figure 2-5 shows a few examples of computer generated integrated PSFs with different Strehl ratios for an 8 m class telescope. A system is said to be well corrected when the Strehl is greater than 80%. This is also called the **Marechal limit** [Born and Wolf, 1970].

(a)   (b)

(c)
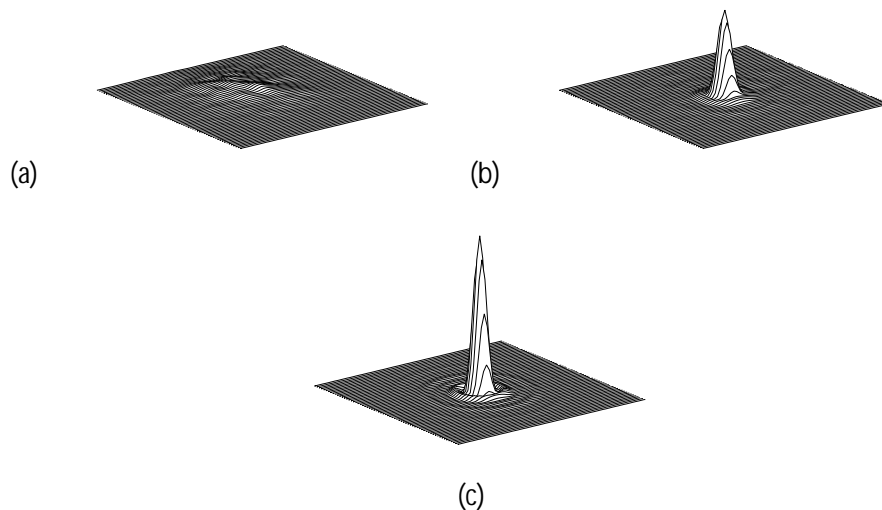
Figure 2-5 Integrated uncorrected PSF with a Strehl ratio of 8% (a), integrated corrected PSF with a Strehl ratio of 49% (b), and diffraction-limited PSF (c).

2.4 Wavefront correction and Zernike polynominals

To correct the wavefront, light from a bright star (located close to the object in the field of view) is measured by a wavefront sensor. This star is called a **natural guide star.** However, if the science object and guide star are too far apart in the sky, the atmosphere will disturb their wavefronts differently and the correction of the science object will be degraded. The patch in the sky around the guide star where the atmospheric influence on the light is essentially the same is called the **isoplanatic patch**.

The effects of turbulence are usually corrected with a tip/tilt and a deformable mirror as shown in Figure 1-1 in the introduction. This is required because of the limited stroke of the deformable mirror. The first correction applied is to compensate the random wandering of the center of the seeing disk with a tip/tilt mirror. The principle of tip/tilt sensing will be more discussed in the next chapter in context with the Shack Hartmann principle and the curvature sensor. To correct the higher order errors of the wavefront a deformable mirror is used. There are various types of deformable mirrors but the most common are **Piezo stack** and **Bimorph mirrors**.

Piezo stack mirrors follow the principle of "push and pull" with a local influence function. Those mirrors have a stroke of a few microns and are usually used with the Shack Hartmann principle, which measures the first derivative of the wavefront. Bimorph mirrors follow the principle of bend and torsion and have a global influence function. Those mirrors are only used for curvature wavefront sensing. In bimorph mirrors, by applying a local pressure, the local curvature is changed and hence those mirrors solve the Poisson equation opto-mechanically. There are also other types of mirror technologies such as liquid crystal modulators and micro mirrors which are still in the development phase. A good reference paper, which describes mirrors used in astronomical AO was published by Marc Sechaud [Sechaud, 1999].

Principle of deformable mirrors used
for astronomical Adaptive Optics
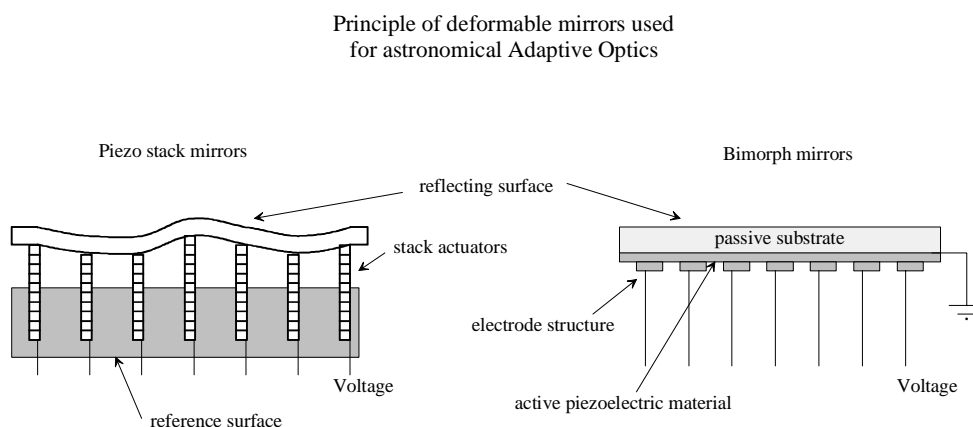
Figure 2-6 Main types of deformable mirrors used in astronomical adaptive optics.

To apply the correct signals to the mirrors the phase variations of the wavefront need to be described in terms of some algebraic quantities. These quantities are called **Zernike**

polynomials, $Z_j(n,m)$ where n is the degree of radial polynomial and m is the azimuthal frequency of a sinusoidal term [Zernike, 1934]. The numbering convention of those polynomials is that the first one is j=1.

NoII proposed to normalize Zernike polynomials such that the rms value of each polynomial over a circle is unity [NoII, 1976]. Zernike polynomials are orthogonal and defined as [Mahajan, 1994]:

$$Z_{jeven} = \sqrt{n+1}R_n^m(r)\sqrt{2}\cos m\theta \text{ , for } m \neq 0$$
$$Z_{jodd} = \sqrt{n+1}R_n^m(r)\sqrt{2}\sin m\theta \text{ , for } m \neq 0 \qquad (2.9)$$
$$Z_j = \sqrt{n+1}R_n^0(r) \text{ , for } m = 0 \text{ ,}$$

where

$$R_n^m(r) = \sum_{s=0}^{(n-m)/s} \frac{(-1)^s (n-s)!}{s![n+m)/2-s]![(n-m)/2-s]!}r^{n-2s} \text{ .} \qquad (2.10)$$

The following Table lists the first eleven low order terms and explains their meaning.

j	n	m	Zernike polynomial	Description	Δ_j/S
1	0	0	1	Constant	1.030
2	1	1	$2r\sin\theta$	tilt	0.582
3	1	1	$2r\cos\theta$	tilt	0.134
4	2	1	$\sqrt{3}(2r^2-1)$	defocus	0.111
5	2	2	$\sqrt{6}r^2\sin 2\theta$	astigmatism	0.088
6	2	2	$\sqrt{6}r^2\cos 2\theta$	astigmatism	0.0648
7	3	1	$\sqrt{8}(3r^3-2r)\sin\theta$	coma	0.0587
8	3	1	$\sqrt{8}(3r^3-2r)\cos\theta$	coma	0.0525
9	3	3	$\sqrt{8}r^3\sin 3\theta$	trifol	0.0463
10	3	3	$\sqrt{8}r^3\cos 3\theta$	trifol	0.0401
11	4	0	$\sqrt{5}(6r^4-6r^2+1)$	spherical	0.0377

Table 2-1 Modified Zernike polynomials after NoII and the mean square residual errors for Kolmogorov turbulence after removal of the first j terms.

An arbitrary phase function $\phi(r,\theta)$ over a unit circular aperture can be expanded as

$$\phi(r,\theta) = \sum_0^\infty a_j Z_j(r,\theta) \text{ ,} \qquad (2\text{-}11)$$

where the amplitudes a_j of the Zernike components are given by

$$a_j = \int d^2 r \phi(r,\theta) Z_j(r,\theta). \qquad (2\text{-}12)$$

When Zernike modes are used as the basis to compensate turbulence, the lowest modes, such as tilt and defocus are compensated first. If the first N modes are corrected the phase correction can be written as

$$\phi_{corrected} = \sum_{j=1}^{N} a_j Z_j . \qquad (2\text{-}13)$$

Noll showed [Noll, 1976], that the mean square residual error Δ_j may be expressed as

$$\Delta_j = A_N \left(\frac{D}{r_0} \right)^{5/3} . \qquad (2\text{-}14)$$

The last column in Table 2-1 gives the mean square residual error Δ_j in the phase variations at the telescope pupil caused by Kolmogorov turbulence after the removal of the first j terms. These terms, also called the residual phase variations, are normalized by a factor of $S = (D/r_0)^{5/3}$. If j is large (for j>10), Noll derived the value of Δ_j by the approximate expression:

$$\Delta_j \approx 0.29 j^{-\frac{\sqrt{3}}{2}} \left(\frac{D}{r_0} \right)^{5/3} rad^2 \text{, for j >10.} \qquad (2\text{-}15)$$

Figure 2-7 shows three examples of Zernike polynomials such as defocus, astigmatim and coma.

Examples of Zernike polynominals

$Z_4(defocus)\ \Delta_j / S = 0.111$ $Z_6(astigmatism)\ \Delta_j / S = 0.0648$ $Z_8(coma)\ \Delta_j / S = 0.0525$
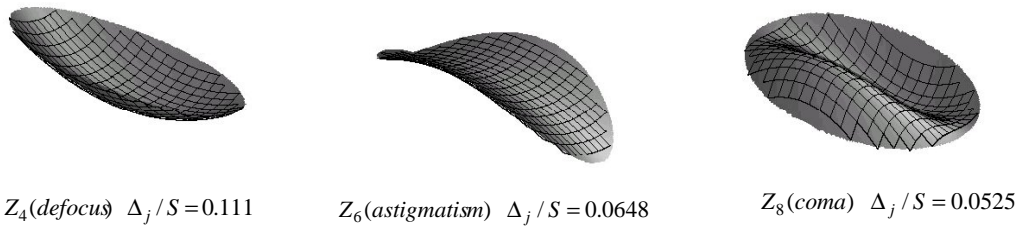
Figure 2-7 Examples of Zernike polynominals.

Using the **Strehl ratio (SR),** which is the ratio of the central intensities of the aberrated point spread function and the diffraction limited point spread function as explained above, for small wavefront disturbances the following relation is given:

$$1 - SR \approx \Delta \approx 1 - e^{-\Delta} . \qquad (2\text{-}16)$$

Note the large effect on the residual variance of the correction of tip and tilt ($\Delta_3 = 0.134$, see Table 2-1). Approximately 87% of the wavefront variance is contained in these terms. However, the degree to obtain a certain Strehl ratio depends very strongly upon D/r_0. For example if $D/r_0 = 40$, (a typical value for a 4 m telescope in the visible), then more than 1000 Zernike terms must be corrected to reach the Marechal criterion. According to this a large number of corrections is needed to achieve a Strehl ratio as high as 80% under average seeing conditions on a 4 or 8 m class telescope. For another numerical example, we assume an adaptive optics system that perfectly corrects the first 10 Zernike modes. The Fried parameter is r_0 =60 cm which is typical in the near infrared and corresponds to a seeing value of 0.76". On a 3.5 m telescope the residual variance equals $0.0401 \left(\dfrac{D}{r_0} \right)^{5/3}$ =0.76 rad ^{2}

and the Strehl ratio is 47% [Glindemann, 1997]. However this also implies a large number of subapertures and actuators in the deformable mirror in an AO system.

WAVEFRONT SENSORS–OVERVIEW AND BASIC PRINCIPLES

In astronomical adaptive optics the wavefront sensors are required to use as much light from the reference star as possible. These may be either the brightest star in the vicinity of the observed object, or, a laser guide star. Most natural guide stars emit wide-band thermal radiation that is temporally incoherent and emit photons with peak radiation at wavelength between blue and infrared. Hence astronomical wavefront sensors are required to measure broadband light and usually measure wavefront characteristics in the pupil plane. Most sensors measure the wavefront gradients (the spatial first derivative) or the curvature (the Laplacian) of the wavefront over an array of subapertures in the incoming beam. Figure 3-1 shows schematics of a distortion free image.

DISTORTION FREE IMAGE
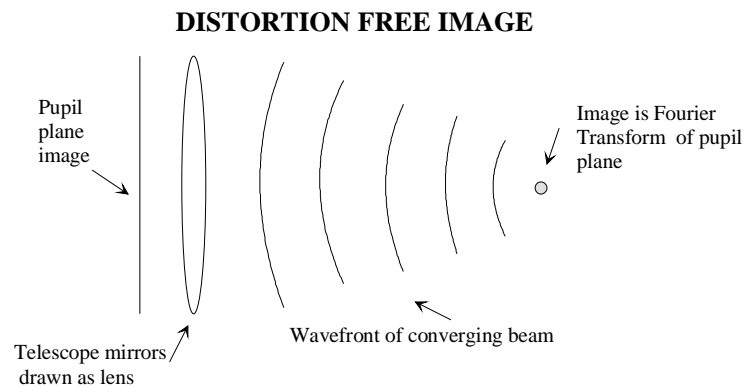
Figure 3-1 Distortion free image.

The resulting image is the Fourier transform of the wavefront in the pupil plane. The two main techniques for gradient sensing are Shack-Hartmann sensor and the shearing interferometer. The local gradients of each subaperture are then reconstructed into a map of the wavefront error over the full aperture. This chapter will give an overview of the most common wavefront sensors used in astronomical adaptive optics and outline the principles behind them.

3.1 Shack Hartmann wavefront sensor

Figure 3-2 presents a schematic diagram of Shack-Hartmann wavefront sensing. Shack-Hartmann divides the wavefront into a two-dimensional array of square or hexagonal subapertures and places a lenslet in each subaperture to produce an array of images, one image from each subaperture. The location of the centroid of the image is a function of the tip and tilt of the wavefront in the subaperture.

**SHACK-HARTMANN
WAVEFRONT SENSING**
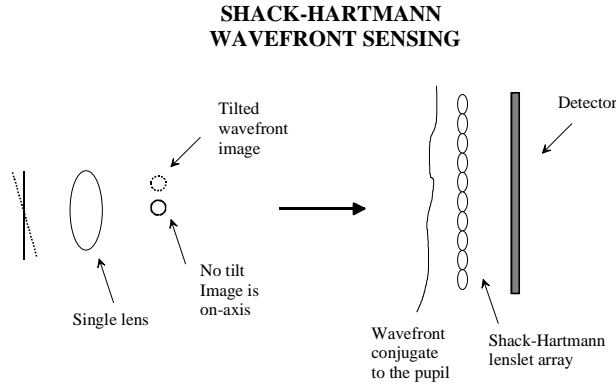
Figure 3-2 A schematic diagram of the principles of Shack-Hartmann.

The direction and magnitude of the two-dimensional wavefront gradient is shown in the angular displacement of the spots. To determine the centroid of the spot, its center of gravity (g_x, g_y) can be calculated as outlined in a article by Rousset [Rousset, 1999] simply as:

$$g_x = \frac{\sum_{l,m} x_{l,m} I_{l,m}}{\sum_{l,m} I_{l,m}} , \tag{3.1}$$

for the x-axis and

$$g_y = \frac{\sum_{l,m} y_{l,m} I_{l,m}}{\sum_{l,m} I_{l,m}} , \tag{3.2}$$

for the y-axis.

$I_{l,m}$ are the signals and (l,m) the coordinates of the pixels on the detector. Since the equation is normalized, the sensor is relatively insensitive to scintillation. Taking the relation between the wavefront and the phase:

$$W(x, y) = \frac{\lambda}{2\pi} \phi(x, y) , \tag{3.3}$$

and not taking into account the scintillation and replacing the discrete sum by a continuous integral, the average wavefront slope α_x in the x-axis (the angle of arrival on the sky) over the subaperture area A_{sub} can be written as

$$\alpha_x = \frac{g_x}{fM} = \frac{\lambda}{2\pi A_{sub}} \int_{sub} \frac{\partial \phi}{\partial x} dx dy , \tag{3.4}$$

for the angle of arrival for the x-axis and

$$\alpha_y = \frac{g_y}{fM} = \frac{\lambda}{2\pi A_{sub}} \int_{sub} \frac{\partial \phi}{\partial y} dxdy ,$$ (3.5)

for the angle of arrival for the y-axis, where *M* is the magnification between the telescope entrance plane and the plane of the lenslet array. *f* the focal length of the lenslet array.

Usually, a CCD is used to detect the images of a Shack-Hartmann lenslet array. A minimum of 2 by 2 pixels, a quad cell, is needed to detect the image of each subaperture. To prevent optical "crosstalk" between subapertures, a "guard ring" of at least one pixel (as done at Keck) is placed between subapertures. Thus, some Shack-Hartmann systems use 3 by 3 pixels per subaperture. Another common arrangement (e.g. Starfire Optical Range) is to have 4 by 4 pixels per subaperture.

Some systems use 8 by 8 pixels in each subaperture [Rousset et al, 2000]. Having more pixels gives more dynamic range to the WFS (i.e. greater tilts can be measured) and allows for more extended objects, but this is at the expense of the greater noise due to more pixels read out as well as longer readout time. To increase readout speed and lower the effect of readout noise, the 8 by 8 pixels can be binned into "superpixels" to mimic a smaller number of (larger) pixels [Feautrier and Dorn, 1999].

Figure 3-3 shows the CCD of the visible wavefront sensor for the Shack Hartman adaptive optics system (NAOS) described by P. Feautrier and R. Dorn et al, 1999. The CCD used is a 16-port split frame transfer CCD with a light sensitive area of 128×128 pixels. With the 16 readout ports, the CCD is partitioned into 16 sections, each being read out from one amplifier only.

Two movable microlens arrays are used to focus the light of the individual subapertures on the CCD. The lenslet arrays, with 7×7 and 14×14 subapertures respectively, are integrated inside the cryostat (not shown in this picture). Figure 3-4 shows a CCD frame with spots of the 14x14 lenslet array configuration and diagram of the computed spot locations with this configuration.
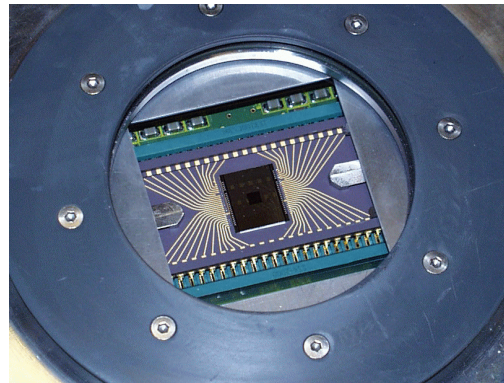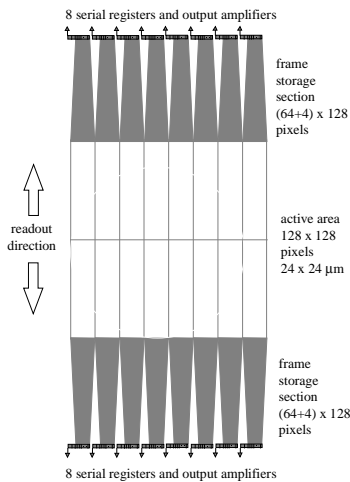
Figure 3-3 EEV CCD-50 used for the NAOS visible wavefront sensor.
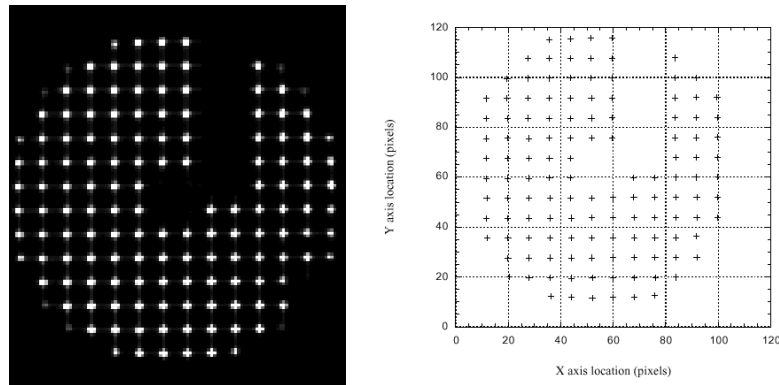
Figure 3-4 Left: Spot image of the 14 x 14 lenslet array of the NAOS adaptive optics system. Right: Computed spot locations of this image. Note that one amplifier in the upper left corner is not working due to defect amplifier on the engineering grade CCD detector.

3.2 Shearing interferometer

The principle of a shearing interferometry (SI) is to split the incoming wavefront into two replicas i.e. two beams that are mutually displaced or sheared by a small distance and then recombined. By making the two optical paths equal, an interference pattern with incoherent light is formed. The intensity of the interference pattern is proportional to the wavefront gradient in the direction of shear. An objective lens generates the Fourier transform of the incoming wavefront at its focal plane and the lens in front of the detector produces an image of the pupil, which contains the disturbance at the detector plane. Hence, an array of photoelectric-detectors or a CCD is used to measure the fringe pattern. The amount of shear is usually adjustable.
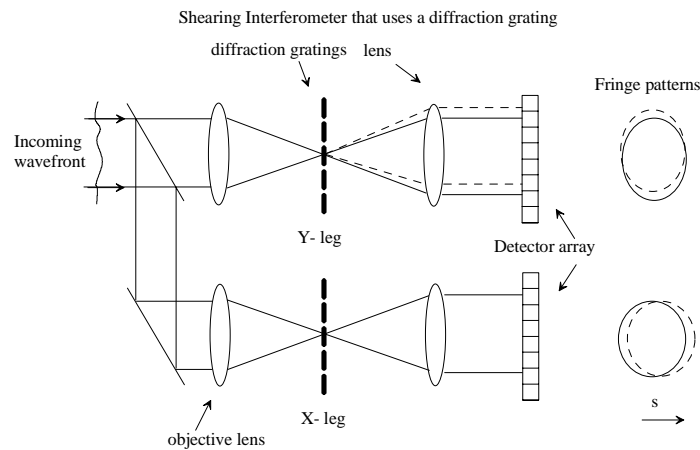
Figure 3-5 Shearing interferometer that uses a diffraction grating.

Either a diffraction grating [Wyant, 1974 and Horwitz, 1990] or polarization [Hardy and MacGovern, 1987] is used to obtain the two beams. Figure 3-5 shows a schematic drawing of a rotation grating lateral shearing interferometer described by Hardy et al. One advantage of using a grating to produce the shear is that it enables the detector signal to be chopped or modulated simply by moving the grating and thus eliminating errors due to

calibration and drift, i.e. generated by the detectors. Two such interferometers are normally used, making wavefront gradient measurements in two orthogonal directions X and Y as seen in Figure 3-5. The intensity or signal measured from the incoming wavefront $\psi(\vec{r})$ is given by the sum of the complex amplitudes as:

$$I(\vec{r}) = \frac{1}{2}\left|e^{i\psi(\vec{r})} + e^{i\psi(\vec{r}+\vec{s})}\right|^2 = 1 + \cos\left[\psi(\vec{r}) - \psi(\vec{r}+\vec{s})\right], \qquad (3.6)$$

where $\vec{s}$ is the distance of displacement or shear in the detector plane between the zero and first diffraction orders. $\psi(\vec{r}) - \psi(\vec{r}+\vec{s})$ is called the phase difference. In the case for the diffraction grating, there is another advantage because the shear distance becomes proportional to wavelength, in which case the interference fringes coincide at all wavelengths so that the sensor operates with white light. For small shears s, the wavefront slope is proportional to the phase difference and can be expressed in a Taylor series for the x and y leg of the interferometer [Koliopoulos, 1980]. For the x - direction the phase difference can be calculated as

$$\psi(\vec{r}) - \psi(\vec{r}+\vec{s}) = s\frac{\partial \psi(\vec{r})}{\partial x} + \varepsilon_x(s) \, , \qquad (3.7)$$

in which case the y shear is zero and for the y- direction as

$$\psi(\vec{r}) - \psi(\vec{r}+\vec{s}) = s\frac{\partial \psi(\vec{r})}{\partial y} + \varepsilon_y(s) \, , \qquad (3.8)$$

in which case the shear in x is zero. $\varepsilon_x(s)$ and $\varepsilon_y(s)$ represent the higher order terms of the Taylor approximation. Two detectors are needed measure and reconstruct the wavefront slopes and this leads to a complex system in terms of hardware and implementation. Therefore shearing interferometers are not widely used in adaptive optics in astronomy.

3.3 Pyramid wavefront sensors

The concept of the pyramid wavefront sensor is a fairly new concept in adaptive optics and is based on a modification of the Foucault knife-edge test used in optics to evaluate qualitatively the aberrations of an optical system. Pyramid wavefront sensing was first proposed by Ragazzoni in 1996 [Ragazzoni, 1996]. Like a Shack Hartmann sensor it measures the first derivative of the wavefront, the wavefront slope or gradient.
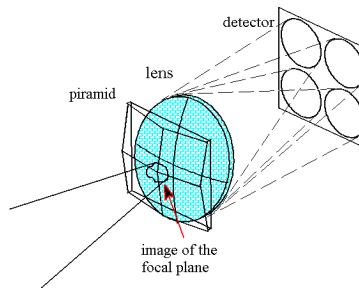
Figure 3-6 Principle of the pyramid wavefront sensing.

A pyramid lens with four equal faces is placed with its vertex on the nominal focus point of the optical system. The four faces deflect the beam in four different directions, depending on which face of the prism gets hit by the incoming ray. A field lens is then used to re-image the pupil of the telescope. In the pupil plane a detector is used to measure the individual signals of the four faces. The principle is illustrated in Figure 3-6.

In this configuration a ray of the incoming beam with wavefront error $\psi(\vec{r})$, originating from a generic point $\vec{r} = (x, y)$ on the pupil plane, is aberrated and reaches the pyramid displaced by a vector $\vec{p}$ from the vertex. The amount of displacement is:

$$\vec{p} = f \frac{\partial \psi(\vec{r})}{\partial \vec{r}} ,\qquad (3-9)$$

where f is the effective telescope focal length.

Hence one face will refract the ray and only in the corresponding pupil the region conjugated to the point $\vec{r}$ in the pupil plane will be bright. The other three pupils will show a dark region in the same point. Although it is not possible to obtain the value of the aberration, its sign can be retrieved.
Ragazzoni (1996) proposed to oscillate the pyramid (parallel to its base plane in "dx" and "dy" direction as illustrated in Figure 3-7) to allow all the aberrated rays to sweep over the four faces.

Pyramid wavefront sensing - Principle operation
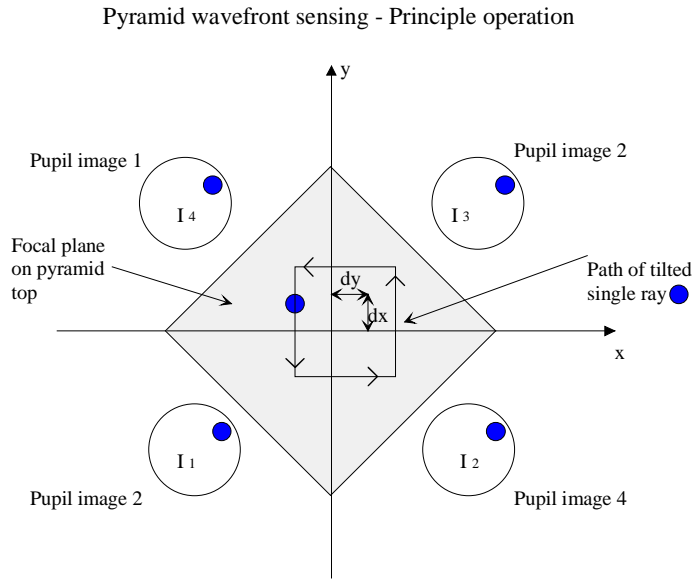
Figure 3-7 Pyramid wavefront sensing - principle operation.

If the introduced modulation $\delta\theta_x$ in the x and $\delta\theta_y$ in y direction satisfies the requirement

$$\delta\theta > \left| \frac{\partial \psi(\vec{r})}{\partial \vec{r}} \right| .\qquad (3.10)$$

Each pupil will receive a particular intensity of illumination that will be proportional to the displacement of the rays with respect to the pyramid vertex.

After an integer number of oscillation cycles, the four pupil signals I_1, I_2, I_3 and I_4 are combined and normalized by the sum. Hence it is possible to retrieve the first derivatives or slopes $\frac{\partial \psi(x,y)}{\partial x}$ and $\frac{\partial \psi(x,y)}{\partial y}$ of the wavefront along two orthogonal axes:

$$\frac{\partial \psi(x,y)}{\partial x} = \delta\theta_x \frac{(I_1 + I_4) - (I_2 + I_3)}{I_1 + I_2 + I_3 + I_4} ,$$ (3-11)

and

$$\frac{\partial \psi(x,y)}{\partial y} = \delta\theta_y \frac{(I_1 + I_2) - (I_3 + I_4)}{I_1 + I_2 + I_3 + I_4} .$$ (3-12)

The oscillation of the pyramid can be also done by tilting a mirror in the pupil plane as suggested by Riccardi [Riccardi, 1996]. More details on the calculations and the implementation of the tip/tilt mirror are outlined in that paper.

The pyramid wavefront sensor shows some advantages with respect to a Shack Hartmann one. The gain is variable by adjusting the amount of the movement or oscillation of the pyramid in x and y. The amplitude can be increased when the image tilt is too large (for example during closing the loop), or to maintain an as high as possible signal to noise ratio during the measurements.

A zoom lens can be used in order to modify the spatial sampling on the detector and optimize the wavefront sensing for the different wavelengths, the seeing conditions, and the brightness of the guide star.

As mentioned before for the Shack Hartmann sensor often a guard ring around each subaperture is used to avoid cross talk between the subapertures. In the case of pyramid wavefront sensor the problem of wandering spots does not exist so the guard ring area can be eliminated and the detector can be smaller than in the Shack Hartmann sensor.

The pyramid wavefront sensor has also another important property pointed out by Ragazzoni and Farinato [Ragazzoni and Farinato, 1999]. The signal to noise ratio is increased once the loop is closed, similarly to the curvature sensor explained in the next section and contrasting with the Shack Hartmann wavefront sensor. In the Shack Hartmann wavefront sensor the pupil sampling is provided by the lenslet array and the typical projected size of each lens on the pupil is of the order of r_o.

Once the loop is closed and the star has a diffraction limited FWHM the spots angular size on the detector still remains λ/r_o (λ is the effective wavelength of the wavefront sensor). If, for example, a tilt of λ/D (D is the telescope diameter) is introduced by the atmosphere the spots will move only by a fraction of their size. In the PWS the spot size on the pyramid vertex will be roughly λ/D when the loop is closed successfully, and a tilt of λ/D will change drastically the illumination of the pupils on the detector because the whole spot has moved to one or two faces of the pyramid.

Although a first laboratory pyramid wavefront sensor prototype has been tested at the Observatory of Arcetri giving promising results [Riccardi et al., 1996 and 1998] and the same group is now working on loop closure with the PWS and a high order deformable mirror, it has never been fully implemented at a telescope.

Most recently relevant result where obtained with a system mounted on the adaptive optics module of the National Telescope Galileo (AdOpt@TNG) for testing purposes. During the commissioning phase, the high order loop has been closed first on the optical bench with an artificial source and after November 1999 on the sky with a natural guide star.

3.4 The curvature wavefront sensor

Although curvature WFS is used in two of the most successful astronomical AO systems [Roddier and Rigaut 1999], the operation of a curvature WFS is not widely understood. To understand the requirements for the new CCD design, one must first understand curvature wavefront sensing. Therefore a more detailed section is included which gives an overview of curvature WFS.

Curvature wavefront sensing takes an entirely different approach then Shack Hartmann wavefront sensors. In curvature AO, the WFS measures an "image" at a location between the pupil plane and the image plane. If this image is before focus, it is called the **intrafocal image**; the image after focus is the **extrafocal image**, as shown in Figure 3-8. The intrafocal image will be brighter in regions which have a positive curvature and the image will be darker in regions with negative curvature. The intensity of the extrafocal image will be reversed relative to the intensities measured in the intrafocal image. In principal, only one out of focus image is needed to measure wavefront curvature.

**CURVATURE
WAVEFRONT SENSING**
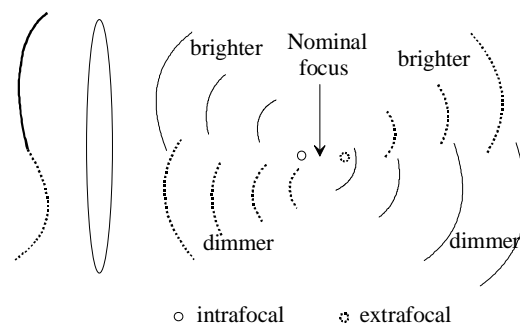
Curvature wavefront sensing looks at intensity between pupil image and image plane. Curved wavefront comes to focus before and after nominal focal plane and thus is brighter or dimmer in out-of-focus image. Must sense on both sides of focus to calibrate scintillation.

Figure 3-8 A schematic diagram of the principles of curvature wavefront sensing.

However, using both the intrafocal and extrafocal images makes a curvature system work better for several reasons: (a) there is automatic compensation of systematic errors - variation in quantum efficiency, electronic gain, etc., (b) there is compensation of atmospheric scintillation, and (c) the control signal is simple – move the deformable mirror so that the intensity difference is zero. In a curvature AO system, the goal is to make the intensities equal on both sides of focus – this will occur when the wavefront is flat.
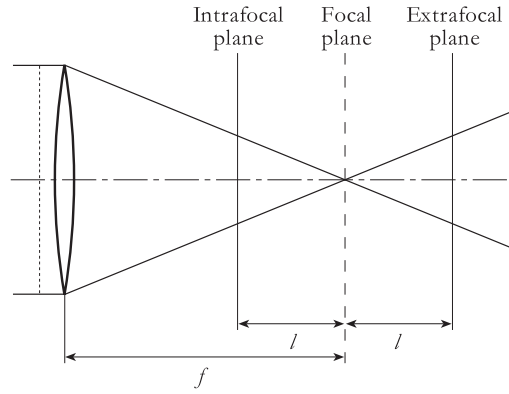
Figure 3-9 A flat wavefront focused by a lens, showing the intrafocal and extrafocal image planes on either side of the focal plane. Note that in actual implementation in curvature AO systems, the intra- and extrafocal planes are very close to the image plane, about 0.1% of the distance from the image plane to the pupil plane.

In order to derive the signal measured by the intrafocal and extrafocal images, we must look at the propagation of the electric field of the wavefront. Defining the direction of propagation from the pupil plane to the image plane as the direction z and the two orthogonal directions as x and y, the complex amplitude $U(x,y,z)$ of the field in a z-plane is the square root of the intensity $I(x,y,z)$ multiplied by the complex phasor of the wavefront phase $\phi(x,y,z)$:

$$U(x, y, z) = \sqrt{I(x, y, z)}e^{ik\phi(x,y,z)} \, ,$$ (3-13)

where k is the wavenumber ($2\pi/\lambda$) and λ is the wavelength of the light. The propagation of this field over short distances, i.e. in the near field, is defined by the **irradiance transport equation** [Teague, 1982 and 1983 and Ichikawa et al., 1988]:

$$\nabla I \cdot \nabla \phi + I \nabla^2 \phi + \frac{\partial I}{\partial z} = 0 \, ,$$ (3-14)

where the gradient $\nabla = \dfrac{\partial}{\partial x} + \dfrac{\partial}{\partial y}$ and the Laplacian $\nabla^2 = \dfrac{\partial^2}{\partial x^2} + \dfrac{\partial^2}{\partial y^2}$. The last term in the Eq.

(3-14), $\dfrac{\partial I}{\partial z}$, is the change in intensity as a function of propagation in the direction z. The change in intensity is the result of two terms:

$\nabla^2 \phi$ is the second derivative of the wavefront, i.e. the wavefront curvature
$\nabla I \cdot \nabla \phi$ is the tilt of the wavefront – this term is only significant where the intensity is rapidly varying, which is at the edge of the pupil.

The change in intensity from intrafocal to extrafocal planes is due to the curvature of the wavefront over the pupil and the tilt of the wavefront at the pupil edge. The usefulness of this signal for adaptive optics was first recognized by Francois Roddier in 1987 [Roddier, 1987] and he first presented a system concept for wavefront sensing [Roddier, 1988]. Using the vector r for the location x,y in a z-plane, I_1, I_2 for the intrafocal and extrafocal images,

and l for the intra- and extrafocal distances, Roddier used the geometrical optics approximation to derive the curvature signal as,

$$S(\vec{r}) = \frac{I_2(\vec{r}) - I_1(-\vec{r})}{I_2(\vec{r}) + I_1(-\vec{r})} = \frac{\lambda f(f-l)}{2\pi l}\left[\nabla^2\phi\left(\frac{f\vec{r}}{l}\right) - \frac{\partial\phi}{\partial n}\left(\frac{f\vec{r}}{l}\right)\delta_c\right] ,\tag{3-15}$$

where f is the telescope focal length, $\dfrac{\partial}{\partial n}$ is the derivative in the outward pointing radial direction and δ_c is a linear impulse function at the edge of the pupil (both at the outer edge of the primary and the inner edge due to secondary obscuration). The radial wavefront tilts provide the boundary conditions necessary to determine the phase from the curvature signal. Normally, in an operating curvature AO system, the phase is never computed as the Poisson equation is solved automatically by the bimorph mirror response function. Since tilt is only sensed at the pupil edge and the curvature signal is sensed over the entire pupil, this approach of sensing wavefront distortions is called **curvature wavefront sensing**.

It is important to emphasize that Eq. (3-15) is only strictly correct if the geometrical optics approximation is valid. Geometrical optics is valid if the blur of the defocused pupil is smaller than the size of the wavefront aberrations we wish to measure.

A physical way to understand the geometrical optics approximation is as follows. As the light propagates from the pupil plane to the image plane, any wavefront that is tilted will propagate into the path of neighboring areas of the wavefront, causing blurring and concentration of the light in regions of curvature. This is what we wish to measure, but we don't want the light from one subaperture to interfere too much with the light from another subaperture. The amount of light that travels "sideways" into a neighboring subaperture is given by the seeing angle, $\dfrac{\lambda}{r_0}$, propagated over the distance $(f - l)$. We want this blurring to be smaller than the subaperture d (scaled by the reduction in size of the pupil due to propagation to the image plane, i.e. $d\,l/f$). Thus, for geometrical optics to be valid, we require that

$$\frac{\lambda}{r_0}(f-l) < d\left(\frac{l}{f}\right).\tag{3-16}$$

Since f is much larger than l, we can approximate $(f-l)$ as equal to f, and rearrange to isolate l, resulting in

$$l > \frac{\lambda f^2}{r_0 d} .\tag{3-17}$$

Since most curvature AO systems are designed to sense in the visible but achieve good correction in the infrared, the subaperture size d is usually significantly larger than the r_0 of the sensing wavelength. For the 60 element curvature AO systems being developed for the VLT, the subaperture diameter is about 80 cm and the wavefront sensor will see an f/50 beam from the 8 m telescope, thus the effective focal length f is 400 m. The VLT median seeing of 0.66 arcsec (defined at 500 nm) gives an r_0 of about 19 cm at the 700 nm (middle of bandpass of red-optimized silicon based wavefront sensor detectors). Using these numbers, Eq. (3-17) states that the geometrical optics approximation is valid for out of focus distances greater than 74 cm.

But, ESO's 60 element curvature AO systems plan to use out of focus distances of 25 to 50 cm. How does this work? The geometrical approximation only defines when Eq. (3-15) is strictly valid. When l is too small and the curvature signal is nonlinear, the curvature signal still gives the correct sign, i.e. which way to push the deformable mirror. Once the loop is closed and the diffraction-limited core of the infrared images are 60 milliarcsec diameter, the "effective r_0" is much larger and Eq. (3-15) becomes valid. Note that it takes only about 5 cycles of the AO loop, about 15 msec, to achieve closure - the curvature wavefront sensor signal is in the nonlinear regime for a negligible period of time.

The reason that the out of focus distance is set to 25-50 cm is to increase the sensitivity of the signal. As l is made smaller, the curvature signal becomes larger. In optimizing a curvature AO system, a critical parameter is the out of focus distance l. ESO's prediction of best out of focus distance of 25 to 50 cm is based on the results of computer simulations. As the parameter l is set via software, it can be easily changed if laboratory tests and commissioning at the telescope define a more optimal value.

An example of the way that a curvature wavefront sensor senses tilt is shown in Figure 3-10, a schematic drawing that shows the propagation of a flat, but tilted wavefront. The example is exaggerated since l is shown to be about 30% of the focal length, 250 to 500 times greater than an actual implementation.
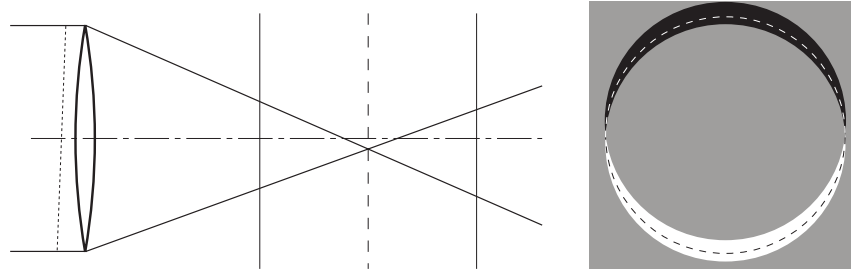
Figure 3-10   Propagation of a flat but tilted wavefront, shown left and the resulting curvature signal, shown right - grey is a curvature signal of zero, white is positive and black is negative. The dashed line in the right picture shows the outline of the pupil.

A more realistic curvature signal is shown in Figure 3-11, which presents a Kolmogorov atmospheric wavefront distortion, the infrared focal plane image, intrafocal and extrafocal images and the curvature signal.

These signals were generated using a computer simulation. In Figure 3-11, the AO loop is not running and thus the curvature signal extends well beyond the pupil. The speckle structure of the out of focus images is partially due to the single wavelength, and integration over the 400-1000 nm bandpass of a silicon sensor would have a smoother structure.
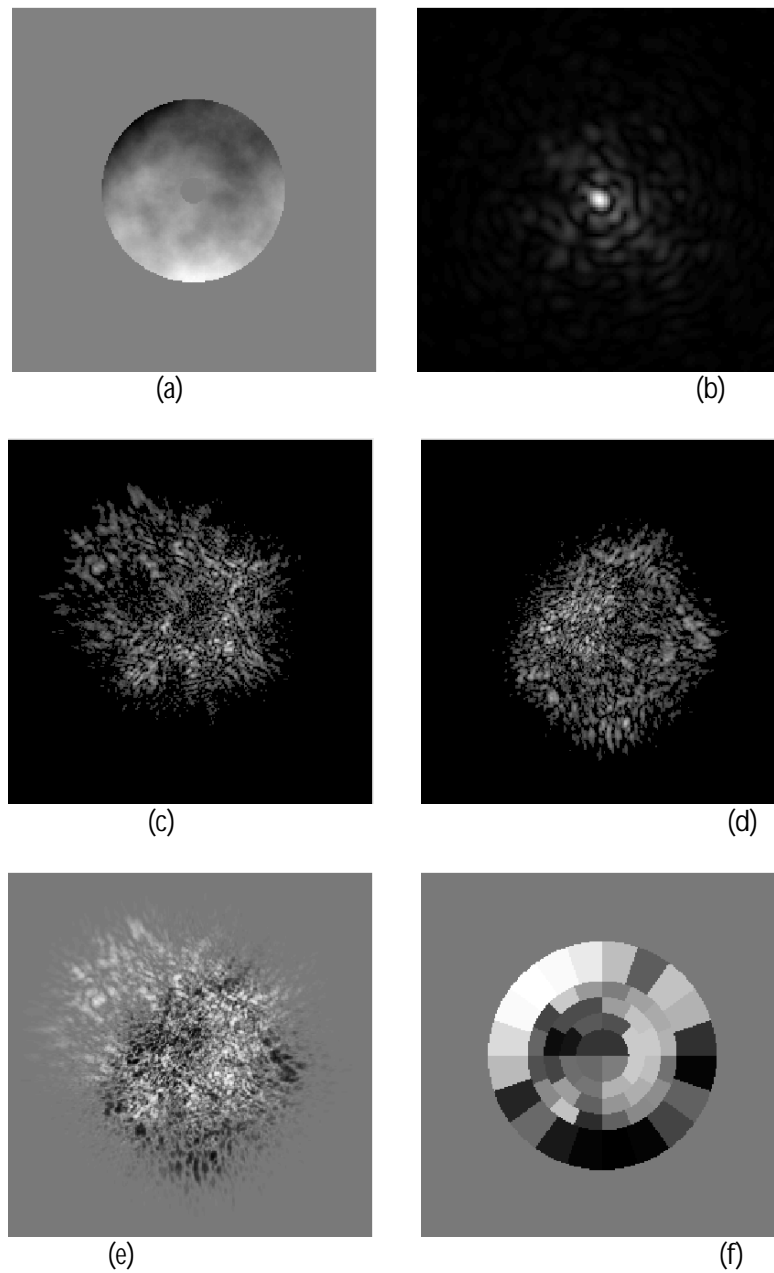
Figure 3-11 Computer simulation of curvature wavefront sensing.

(a) wavefront distortion, (b) infrared focal plane image, (c) intrafocal image, (d) extrafocal image (e) curvature signal at high resolution, (f) curvature signal binned into 60 subapertures. Simulation parameters: 0.66 arcsec seeing (at 500 nm), sensing wavelength = 700 nm (monochromatic), infrared image wavelength = 2.2 μm, out of focus distance = 25 cm, telescope focal length = 400 m, telescope diameter = 8 m with 14% obscuration from 1.12 m diameter secondary. Photon noise has not been simulated – all signals are "infinite" light level.

Chapter 4

IMPLEMENTATION AND COMPUTER SIMULATION FOR A CURVATURE WAVEFRONT SENSOR

4.1 Implementation of the curvature sensor

One way to implement a curvature WFS would be to split the light into two halves and send one-half to a detector before focus and one-half to a detector after the focal plane. However, it would be better to have the same pixel sense the light from each subaperture on both sides of focus. This would remove all systematic errors such as pixel quantum efficiency and electronic gain from the curvature signal. However, if the same pixel is to be used on both sides of focus, it must sample both sides of focus "simultaneously", defined as "faster than the wavefront distortion or the scintillation changes". For correction in the infrared, sample times as short as 1 msec are required. For fainter objects, WFS frame rates as slow as 50 Hz may be useful, but it is important to remember that, even in these cases, the curvature WFS must be able to sample on both sides of focus at 1 kHz rate.

It would be impractical to attempt to physically move a detector the 50 cm between the intrafocal and extrafocal images at a 1 kHz rate. Instead most curvature AO systems in astronomy have adopted the approach pioneered by the U. Hawaii group [Graves and McKenna, 1991 and Graves et al., 1994], which is shown in Figure 4-1. In this arrangement a membrane mirror oscillates in the image plane at 2 to 4 kHz rate, which makes the "detector plane" of the WFS detector alternately conjugate to the intrafocal and extrafocal images. (In Figure 4-1, the "detector plane" is the location of the lenslet array – the lenslet array is explained later on).

The relationship between the detector plane and the out of focus images is most easily explained via geometrical optics, using Figure 4-2, which corresponds directly to Figure 4-1; the telescope mirror in Figure 4-2 is same as the parabolic mirror after the deformable mirror in Figure 4-1.

Focal plane

f_{P}

Converging beam
from main mirror
of telescope

Deformable mirror
in the pupil plane

Parabolic
mirror

Membrane mirror
in the focal plane

f

Re-imaging lens

Optical fibres

f

Detector

Lenslet array
in the pupil plane
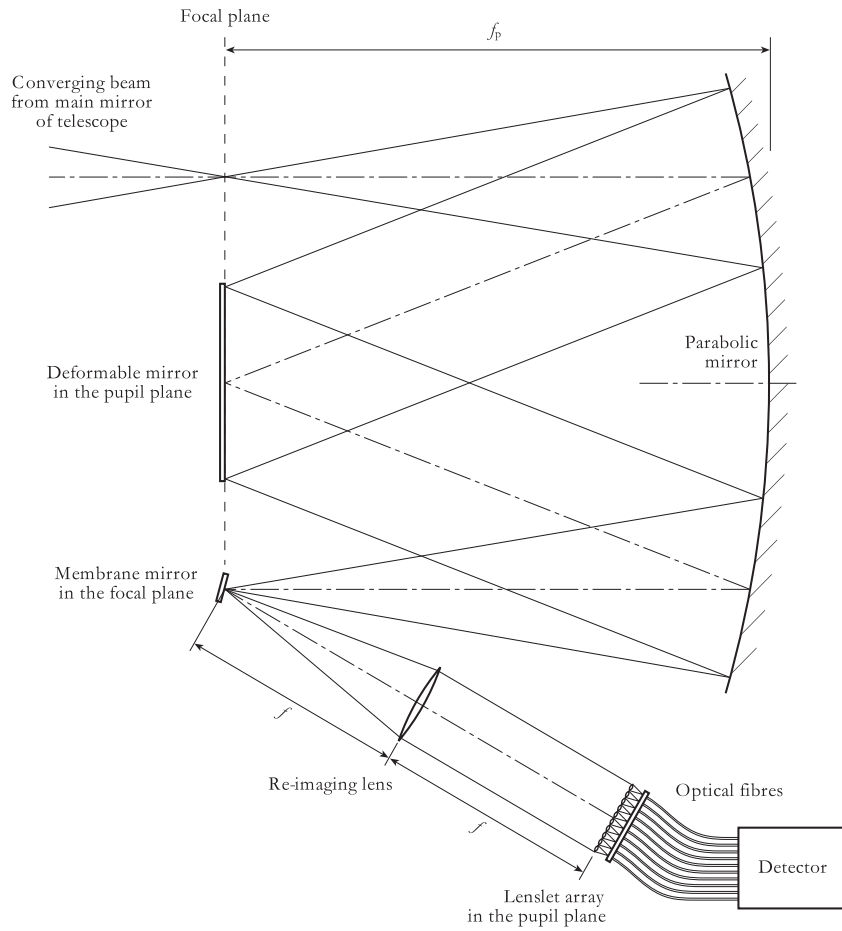
Figure 4-1 Schematic diagram of the typical optical layout of a low light level astronomical AO curvature wavefront sensor.

Figure 4-2 (a) shows the curvature WFS when the membrane is flat. Tracing the rays backwards from a point in the detector plane, we find that the detector plane is exactly conjugate to the pupil plane. With the membrane concave, and thus acting as a converging lens with focal length f_m, as shown in Figure 4-2 (b), the detector plane is conjugate to the intrafocal plane located a distance f_m before focus. Similarly, in Figure 4-2 (c), a convex membrane acts a diverging lens, making the detector plane conjugate to a distance f_m after the focal plane. Thus, the conjugate of the detector plane is defined by the focal length of the membrane.

The membrane is simply an acoustic speaker with reflective coating. It takes on a spherical shape with an amplitude of deformation that is a sinusoid as a function of time. It is important to compute how this sinusoid deformation converts to the membrane focal length.

Pupil plane   Telescope mirror   Membrane   Re-imaging lens   Detector plane

(a)

(b)

(c)
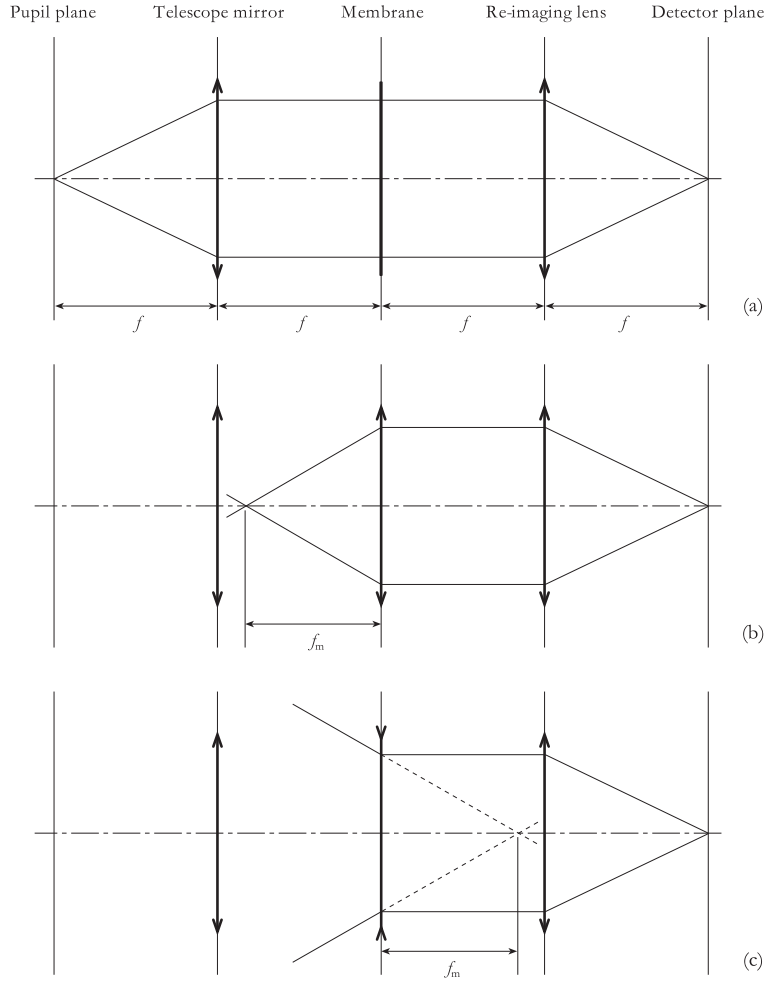
Figure 4-2 Geometrical optics analysis of the curvature wavefront sensor showing (a) case of flat membrane, (b) concave membrane and (c) convex membrane.
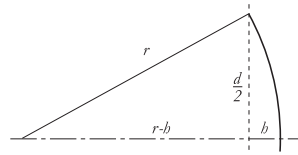
Figure 4-3 Geometry of the membrane mirror in a curvature AO system.

Referring to Figure 4-3, which shows the geometry of the membrane mirror, we see that

$$r^2 = (r-h)^2 + (\frac{d}{2})^2 ,$$ (4-1)

where r is the radius of curvature of the membrane, d is the diameter of the membrane and h is the instantaneous amplitude of the membrane bow. Eq. (4-1) can be rewritten as:

$$r = \frac{h}{2} + \frac{d^2}{8h} .$$ (4-2)

The focal length of the membrane is twice its radius of curvature, thus

$$f_{\mathrm{m}} = h + \frac{d^2}{4h}.$$ (4-3)

Because h is typically much smaller than both d and f_m, the first term in Eq. (4-2) can be neglected. If the maximum amplitude of the membrane vibration is denoted A and the frequency at which it vibrates υ, then $h(t) = A\sin(2\pi\upsilon t)$ and the focal length of the membrane as a function of time is,

$$f_{\mathrm{m}}(t) = \frac{d^2}{4A\sin(2\upsilon\pi t)},$$ (4-4)

where $f_{min} = d^2/4A$, is the minimal focal length of the membrane.

Figure 4-4 plots the membrane amplitude and focal length as a function of time. The focal length function is radically different from a sinusoid. The detector plane literally "zooms" very quickly from the pupil plane, which is 400 m from the image plane, to the minimal focal distance.
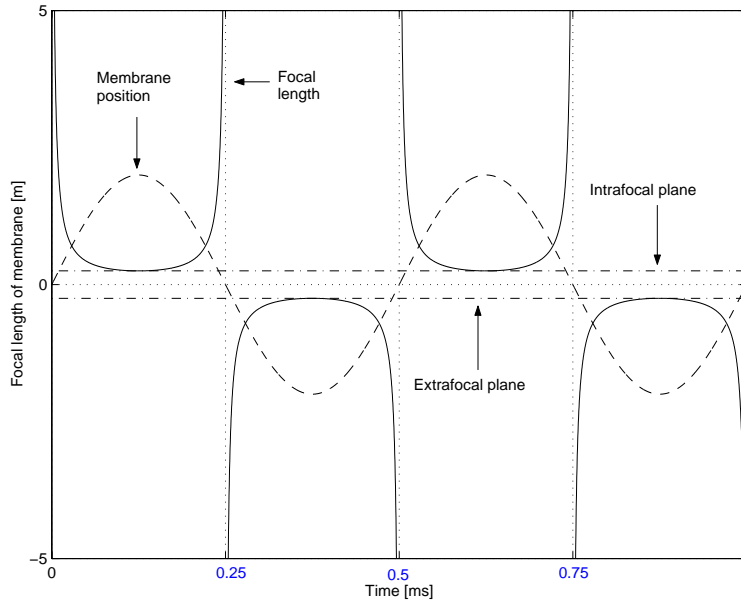
Figure 4-4 Membrane amplitude (dashed line) and membrane focal length (solid line) as a function of time for a 2 kHz membrane frequency with the minimum focal length set to 25 cm.

Viewing out of focus images, one readily sees that there is not much difference between the pupil plane and the out of focus image for $f_m > 3$ m. For a 2 kHz membrane oscillation and $f_{min} = 25$ cm, there is 13 µsec during each half cycle when $|f_m(t)| > 3$ m. Thus, there is at least 10 µsec each half-cycle to allow a detector to switch between intrafocal and extrafocal integration states in the curvature WFS. This is an important parameter to remember when designing a CCD for curvature WFS.

Typical parameters for a membrane are: $d = 10$ mm, $f_{min} = 25$ cm, $A = 100$ µm. It is amazing what an oscillation of a small mirror by the width of a human hair can do!

The operation of a curvature WFS is easily explained in the language of Fourier optics. Referring to Figure 4-1, at the membrane, the complex image field is multiplied by

the membrane function. Since the membrane is purely reflective, the complex membrane function is unit amplitude with a centrally symmetric spherical phase term. At the detector plane, the field is given by the convolution of the pupil plane with the Fourier transform of the membrane function. If the membrane is flat, the membrane function at the detector plane is a delta function and the detector plane is exactly conjugate to the pupil plane. As the membrane increases its curvature, the Fourier transform of the membrane function grows in width so that the convolution integrates over a portion of the pupil. When the membrane curvature switches from concave to complex, the direction of the parabolic phase at the detector plane reverses. Thus, on one side of focus, positive wavefront curvature gives above average intensity at the detector plane and on the other side of focus, the intensity is weaker than average. The amplitude of the membrane oscillation is usually set so that the Fourier transform of the membrane has an effective width, which is approximately the size of a single subaperture.

In this thesis it is assumed that the membrane will oscillate at a frequency of 2 kHz. Due to the relatively low resonance frequency of the bimorph mirrors used for curvature AO, the fastest update rate to a mirror will be 1 kHz. However, at the lowest light levels, there may be as few as 1 photon per subaperture for every 2 cycles of the oscillating membrane and the curvature WFS may need to operate as slow as 50 Hz frame rate. Thus, a curvature WFS detector will need to integrate the light on each half-cycle for 2 to 40 cycles of the membrane. Each half cycle lasts 250 µsec and to minimize time delay, it is highly desirable to be able to read out the detector within 250 µsec.

4.2 ESO's curvature WFS design and detector issues

An APD detector is a good match to these requirements if only a small number of pixels is desired. APD modules achieve 70% quantum efficiency, can detect up to a few million photons per sec, and the APD module outputs a digital pulse 100 nsec after photon detection. The dark current of an APD module can be specified to be less than 100 counts per sec, but a 250 dark count/sec device is sufficient for all but the very darkest nights.
In order to use the smallest number of APD modules, a lenslet array is used to concentrate the light from each subaperture onto an optical fiber, which guides the light to the APD modules, shown as the "detector" in Figure 4-1. The geometry of the subapertures is defined by the lenslet array – the geometry that ESO is using for the 60 element curvature systems is shown in Figure 4-5 [Donaldson et al, 2000].

Manufacture of such a complicated lenslet array is quite difficult and modern laser writing technology can only achieve a sag of 20 µm if one wants to maintain an excellent surface roughness to prevent from straylight or light losses. In order to deal with this strong constraint ESO utilized the following design as shown in Figure 4-6. A pupil diameter of 14 mm was chosen and a division of converging power between 2 lenslets arrays was done. Instead of the field of view, it is now the sub-pupils of the first lenslets array, which are now imaged by the second lenslets array on the fiber entrance. This concept has the advantage to provide a spot diameter, which does not depend on the field of view. The following Figures show the principle of that design.
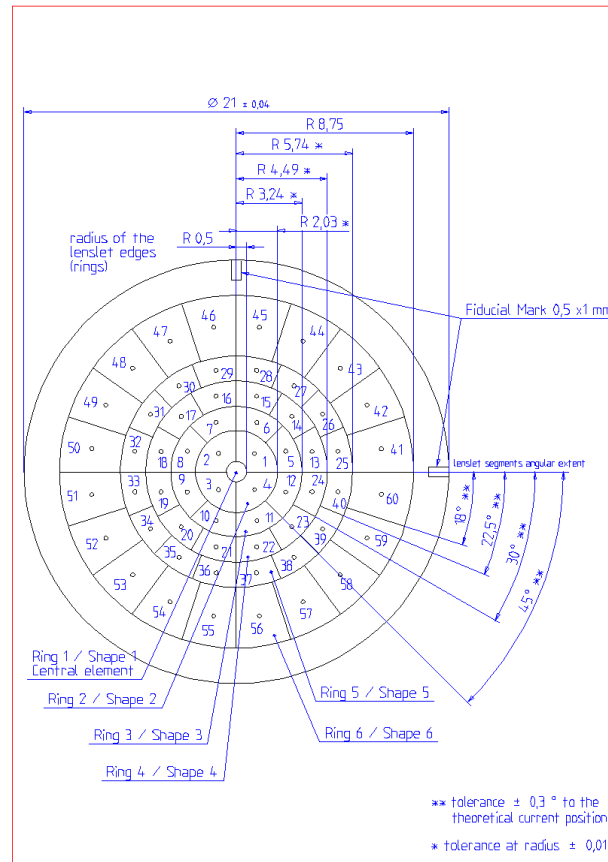
Figure 4-5 Subaperture geometry for ESO's 60 element curvature AO system.
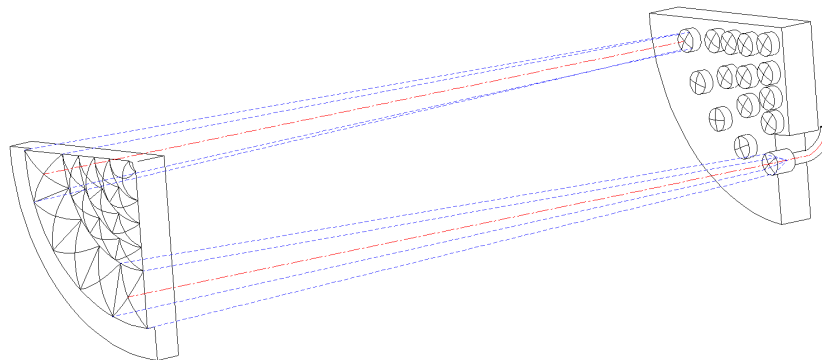
Figure 4-6 Division of converging power between two lenslets arrays.

The subaperture geometry is defined to be annular in order to best match the circular telescope pupil. In specifying the exact layout of subapertures, the first choice is the number of annuli. Then, using computer simulations, various subaperture geometries are tested and the optimal arrangement is chosen. Generally, the chosen geometry is the one that equalizes subaperture areas. The outermost annulus has subapertures that extend beyond the pupil boundary, to capture light that is projected beyond the unaberrated pupil

(see Figure 4-5). In ESO's design, there are 5 annuli and the lenslet array diameter is 25% larger than the pupil diameter. Refer to Figure 3-11(f) in chapter 3 to see an example of the curvature signal intensity integrated into the 60 subapertures.

This lenslet is then incorporated in the "wavefront sensor (WFS) box" [Farinato and Delabre, 2000]. For the ESO MACAO VLTI system the WFS box consists of 4 mirrors, which provides a 14 mm (diameter) parallel beam starting from a F/46.7 beam. The incoming light is reflected by the membrane mirror. This beam is then collimated by the mirror SBM1. This mirror is spherical and tilted by 3°. The second mirror SBM2 folds the beam and send it to the beam expander, which includes the mirrors SBM3 and SBM4. Both mirrors are off-axis parabolas, they produces a 14 mm parallel beam starting from a 4.67 mm beam. This mirror combination re-images the pupil at an accessible location in the parallel beam. An optical derotator in the parallel beam is used to compensate for the pupil rotation and to avoid the rotation of the APD's. The layout of the wavefront sensor box is shown in Figure 4-7.
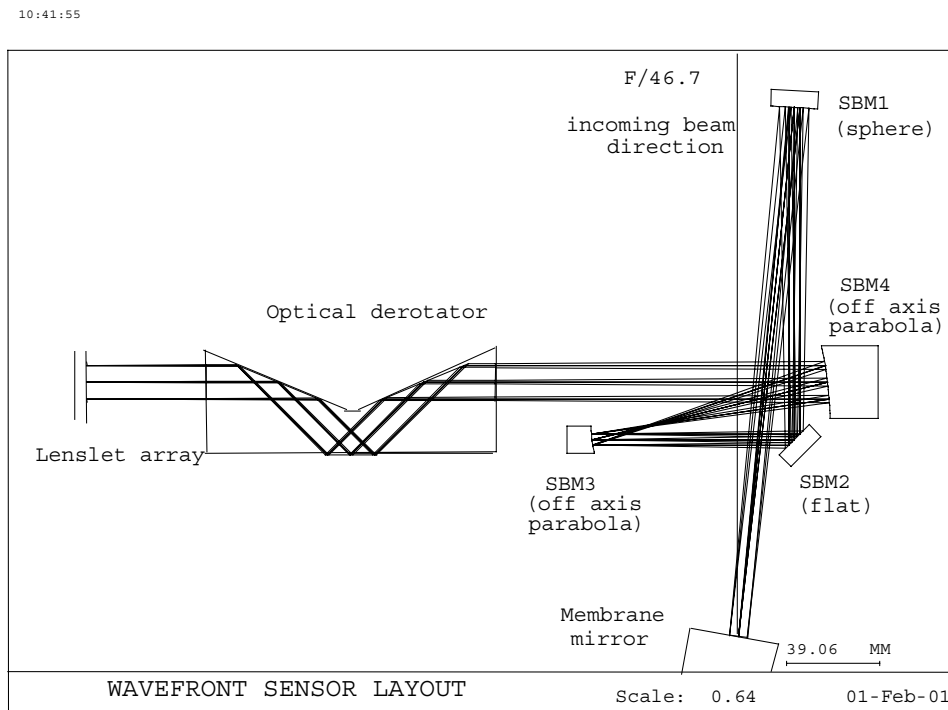
Figure 4-7 Optical layout of the wavefront sensor box for the MACAO VLTI system.

Due to the 120 nsec dead time of the APD modules, 10% non-linearity is reached at 830,000 counts/sec, but this non-linearity can easily be compensated in the real-time computer. More important are the heating effects that occur at high count rates, which can damage the APD module. Thus, the count rate should not exceed a few million counts/sec, which corresponds to an 8th - 9th magnitude object in the ~1 m^2 subapertures of the 60 element AO system on ESO's 8 m telescope. For brighter objects, neutral density filters must be used with the APD modules.

There is only one commercial source for the highest quality APD modules - Perkin Elmer, formerly known as EG&G Canada. This firm has a history of long delivery time for APD modules. In the past, individual APD modules cost $3000 each, but recently several institutes have been quoted a price of $1800 for orders of large quantities (≥100) of the 250 dark count/sec modules.   Thus, for a 60 element curvature AO system, the cost of APD modules is about $108,000.
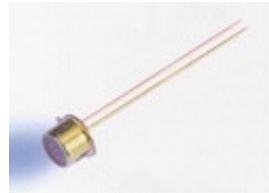
Figure 4-8 Picture of an APD from Perkin Elmer.

Figure 4-9 shows a typical QE curve of the quantum efficiency of an APD module, measured in the ESO laboratories [Farinato et al., 2001].

Measured quantum efficiency of an EG&G APD module
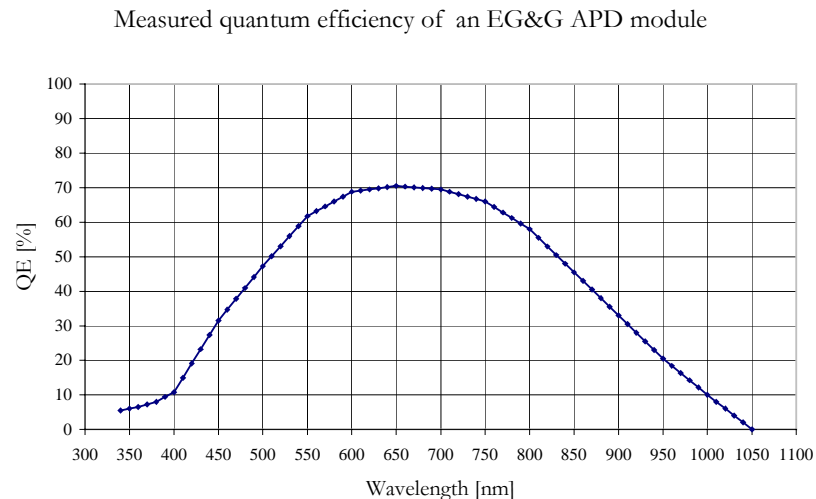
Figure 4-9 APD quantum efficiency.

Due to the large number of 60 element AO systems that ESO is implementing at the VLT telescopes (at least 7, when spare parts are counted), and concerns about APD cost and delivery schedule, ESO began investigating a specially designed CCD as the detector in its curvature WFS [Beletic et al., 2000] as a research and development project and started with a detailed computer simulation to compare the performance and the requirements of the new CCD.

4.3 Computer simulation of curvature WFS detector performance

A detailed computer simulation to compare the performance of the curvature WFS CCD with APD modules has been developed [Craven-Bartle et al., 2000]. The simulation includes detailed models for atmospheric distortions (3 layers with different speeds, directions), telescope optics, bimorph deformable mirror and wavefront sensor optics.
The interaction matrix and control loop utilize the same algorithms as working curvature AO systems. The detector model includes random Poisson processes for modeling dark current and photon detection; readout noise is modeled as a zero mean Gaussian process. The simulation increments time in 15 µsec steps so that the effects of an evolving atmosphere and time delay of CCD readout are accurately modeled.

The quality of this simulation was verified by closely comparing its results with those of a simulation that has been validated with telescope data from the Hokupa'a and Pueo curvature AO systems.

The performance of the AO system is quantified by the Strehl ratio of the image in the K-band (2.2 µm) of the infrared as a function of the visible guide star magnitude. The Strehl is the ratio of the maximum intensity of the point spread function (PSF) relative to the maximum intensity of an aberration-free PSF.

The first result from the simulation was the discovery that, for a 60 element curvature AO system, the instantaneous Strehl was significantly higher than the integrated Strehl, as shown in Figure 4-10.
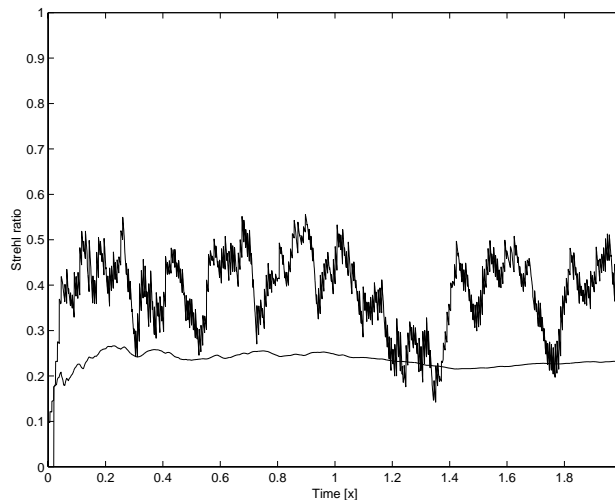
Figure 4-10 Instantaneous and integrated Strehl ratios at 2.2 microns when using APDs and 16th magnitude guide star with no separate tip/tilt sensor.

The reduction of integrated Strehl is due to image wander, a problem that had been speculated for curvature systems with many subapertures [Northcott, 1999]. The simulation was modified to include a separate tip/tilt sensor that used 20% of the light, which gave a significant improvement to integrated Strehl, as shown in Figure 4-11. This prompted us to include a tip/tilt sensor in the curvature AO CCD design presented in the next chapter.

Although there appears to be a clear advantage for using a separate tip/tilt sensor, there may be complications in co-aligning the curvature and tip/tilt sensors.
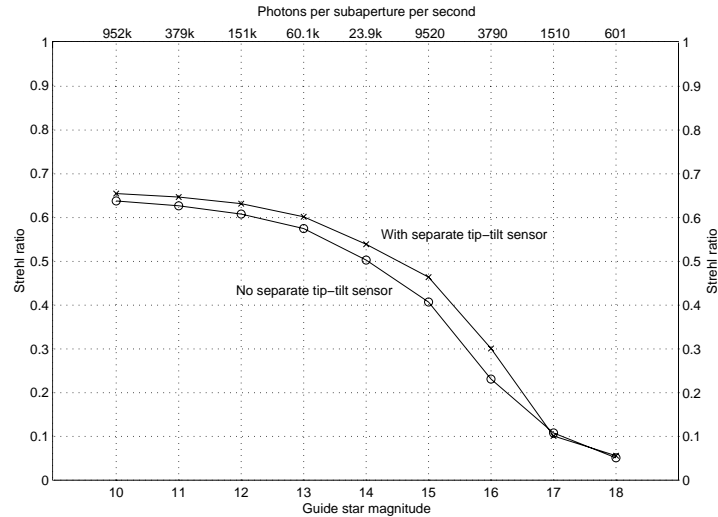
Figure 4-11 Integrated Strehl as a function of guide star magnitude for APD detectors with and without separate tip/tilt sensor (which uses 20% of the light). The sky background is 19th magnitude per square arcsec and the APD dark current is 250 counts/sec.
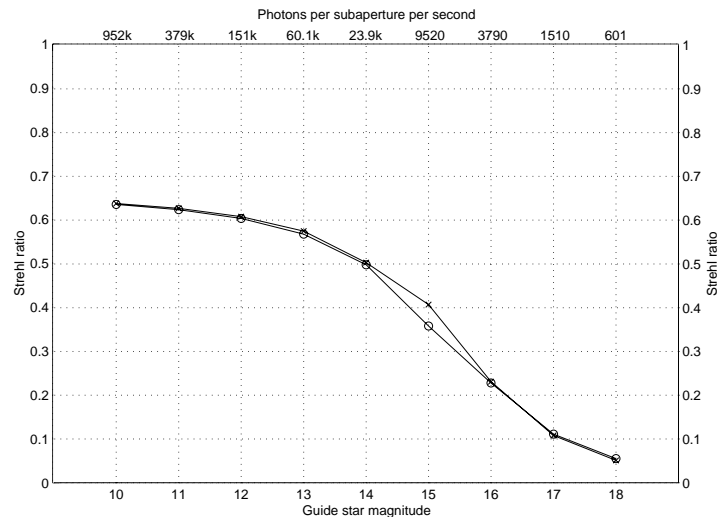
Figure 4-12 Performance of the APD and CCD without a tip/tilt sensor.

Thus, the performance of APDs and CCD for systems with and without a separate tip/tilt sensor were simulated. The results are presented in Figure 4-12 and Figure 4-13, with Table 4-1 listing the parameters used for these simulation runs.
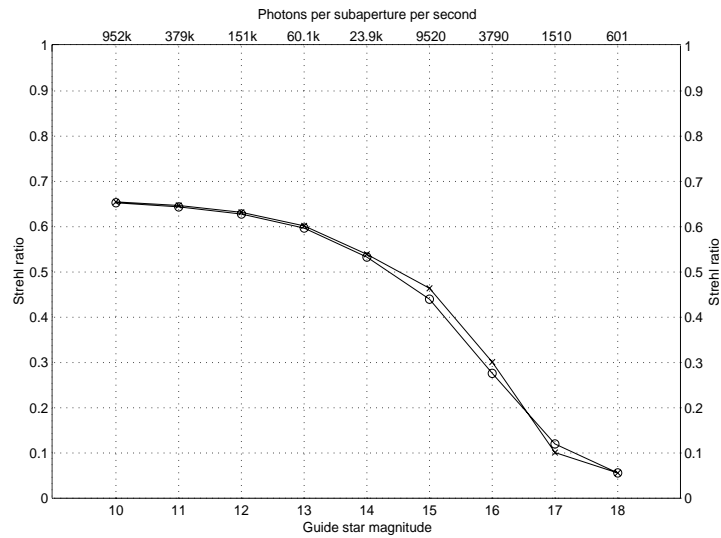
Figure 4-13 Performance of the APD and CCD with a tip/tilt sensor that utilizes 20% of the photons.

For these simulation runs, the APD parameters are: 250 dark counts/sec, 70% quantum efficiency (including fiber losses), zero read noise. The CCD parameters are: zero dark counts/sec, 80% quantum efficiency (including fiber losses), 2 electrons read noise, 250 μsec delay. The sky background is 19th magnitude per square arcsec. A darker sky (21st mag / square arcsec) gives the same results but with slightly better Strehl achieved at guide star magnitudes 16 and 17.

The results from the computer simulation show that the curvature CCD should achieve the same performance as an APD, except at magnitudes 15 and 16, when the integrated Strehl is 2-5% higher for the APD-based system.

Guide star magnitude	Photon flux* per subaperture [1/s]	Integration time [ms]	Loop gain	Photon flux* per integration [1/s]
10	$952 \cdot 10^3$	2.0	0.60	1904
11	$379 \cdot 10^3$	2.0	0.50	758
12	$151 \cdot 10^3$	2.0	0.40	302
13	$60.1 \cdot 10^3$	2.0	0.30	120
14	$23.9 \cdot 10^3$	5.0	0.60	120
15	9520	5.0	0.50	47.6
16	3790	6.5	0.30	24.6
17	1510	15.0	0.30	22.7
18	601	40.0	0.30	24.0

* on the detector – to get number of photoelectrons, multiply by the detector QE.

Table 4-1 Parameters used in the simulation.

With the results from the computer simulation, the requirements for the curvature WFS CCD were as follows:
- 60 integration areas.
- High quantum efficiency (peak greater 80%).
- Very short exposure times (250 μsec) with "long" integration times (1 to 20 msec, 2 to 40 cycles of a 2 kHz membrane).
- Ability to switch between half-cycle integrations within 10 μsec.
- Ability to store half-cycle frames on-chip while integrating other half-cycle frames.
- Lowest possible noise: 2 electrons maximum, < 1 electron desired (including all sources – dark current, readout noise, etc.).
- Read out all pixels within 250 μsec.

The key to making a CCD work in this application is on-chip integration. In order to fulfill the requirements, the following design options were utilized:

- Use of superpixels, i.e. bin on-chip to loosen alignment tolerances.
- Layout pixels on a grid to lower risk (keep it simple!), using fibers to feed from the lenslet array to the CCD, as is done with APD modules.
- Use multiple readout ports to have slower readout rates and lower readout noise.

Note that a previous attempt was made to design a radial geometry CCD for curvature wavefront sensing [Geary and Luppino, 1994]. This CCD would have had the advantage of having the same geometry as a lenslet array used in curvature sensing. Frontside versions of the CCD were fabricated, but were never fully tested. Also another attempt by adapting a 64x64 pixel frame-transfer CCD to be used as a versatile CCD curvature wavefront sensor was made by Burley [Burley et al., 1998]. Burley achieved versatility be having the serial binning pattern and the number of subapertures under software control. However, to the authors knowledge, those versions of a curvature WFS CCDs will not be useful since they fail to fulfill several requirements: They can not integrate half-cycles on chip, they can not switch between half-cycles within 10 μsec and they do not have a < 2 electron noise amplifier and can not be read out in 250 μsec.

However the newly designed CCD, named **CCID-35,** will fulfill all of the requirements. This CCD has the ability to shift intrafocal and extrafocal photoelectrons integrated in a **superpixel** into charge storage areas on either side of the superpixel. The CCD can then be read out relatively slowly while the next integration starts on the chip. The readout noise for the CCD is one of the most critical parameters for use in a curvature WFS. At low light levels, 14th magnitude and fainter stars, 1 to 2 electrons noise at a readout speed of 50,000 pixels/port/sec is required. This very low noise (1.9 electrons) has been demonstrated at ESO with a MIT/LL CCID-20 2k x 4k CCD device at an even higher readout speed of 100,000 pixels/port/sec already in 1997. The same output amplifier design is used for the CCID-35.

In the following chapter, after a brief introduction on the basics physics of charge coupled devices (CCDs), the new CCD design is presented and its implementation for curvature wavefront sensing. The following chapters demonstrate that the CCD can fulfill the requirements.

Chapter 5

ARCHITECTURE AND OPERATION OF THE CURVATURE CCD

Up to now CCDs were not well suited for the use as curvature wavefront sensors. The reason is that conventional CCDs must be read out twice every membrane cycle in order to differentiate the photoelectrons collected during the intrafocal and extrafocal periods. With the membrane oscillating at two kHz, a CCD must operate at a frame-rate of four kHz. With the current detector technology the signal from the CCD would be dominated by read-out noise at that speed. However, if the charge collected during the intrafocal period could be stored away on the chip during the extrafocal period, and vice versa, the CCD would only need to be read out when a new curvature signal is to be calculated. This is the principle of the design of the new CCD, the **CCID-35.**

This CCD has the ability to shift extrafocal and intrafocal photoelectrons integrated in a "**super pixel**" into charge storage areas on either side of the super pixel. This will be explained later in more detail. The CCD can then be read out relatively slowly while the next integration starts on the chip i.e. it has the ability to store charge while reading and integrating with multiple readout ports. The new CCD consists of 80 **unit cells** where the light from each subaperture is focused. The transfer of light to the CCD can be done by a lenslet array directly, or via a fiber feed as done for APDs.

For the scope of this thesis the prototype will use the fiber feed approach since it is difficult and very costly to manufacture a lenslet array, which relays the radial geometry of the pupil image directly onto the grid structure of the CCD. The concept of the CCD and the operation can be fully demonstrated with a fiber feed system. The fiberfeed concept and relay optics design is presented in chapter 6 together with the laboratory system design.

In this chapter the schematic layout of a **unit cell**, a **unit column** (consisting of ten unit cells with the associated readout amplifier) and a schematic overview of the complete **device** (consisting of eight unit columns) plus the functional wiring of the device is presented. The CCID-35 also features a separate tip/tilt sensor integrated on the device. The results of our computer simulation (chapter 4) showed, that a separate tip/tilt sensor would improve system performance for 60-element curvature AO. The best way to measure tip/tilt is with a quad cell detector and therefore we required 4 superpixels on the tip/tilt sensor. The light to the quad cell can be relayed via fiber as for the curvature array.

Following the design, a performance estimation based on calculations and previous measurements with other CCDs is given and a detailed overview on the special developed operation and readout modes is given.

However before explaining in detail the architecture of the new CCD, a brief section on the basic principles of charge coupled devices is included. This will be essential to understand the design of the CCD.

5.1 Basic physics and principle operation a of Charge Coupled Device

Charge coupled devices (CCDs), were invented by Willard S. Boyle and George E. Smith at Bell Laboratories in 1969 in the United States. Boyle and Smith published the first paper in April 1970 in an issue of the Bell System Technical Journal [Boyle and Smith 1970]. A in depth discussion on the basic physics and the design of CCDs can be found in [Janesick, 2001]. However, to understand the principle of the CCID-35 curvature design, the basic principles are briefly discussed.

Absorption of light in silicon

The sensitivity to light of the CCD is based on the photoelectric effect. The electrons of the atoms in a silicon crystal are arranged in discrete energy bands. The lower energy band is called the valence band (VB), the upper band is called the conduction band (CB). Most of the electrons occupy the valence band but can be excited into the conduction band by the absorption of a photon and also thermally, by heating. When the electron reaches the conduction band it can move through the crystal. This can be controlled by an electric field by means of metal plates, the electrodes or gates, biased with an external voltage. The absorption of photons in silicon is a function of energy and therefore also wavelength. The energy required for a transition of an electron from the valence band into the conduction band is 1.26 eV. The amount of photons, which can be absorbed by the silicon at a given depth z, is given by

$$I(z)_{photons} = I(0)e^{-\alpha z}$$

(5-1)

where α is the absorption coefficient (~5/μm for silicon at 400nm and ~0.1/μm at 800 nm at room temperature). At colder temperatures the absorption coefficient gets smaller and photons can penetrate deeper into the material before being absorbed. This can be explained due to the fact that the photon absorption length increases because the silicon bandgap increases [Rajkanan et al., 1979]. This is especially important in the near infrared because phonons help energize free electrons into the conduction band. There is a cut-off wavelength λ_c, which means that photons with lower energies (redder wavelength) cannot interact with the material anymore. It can also be said that beyond a certain wavelength silicon becomes transparent and CCDs constructed from silicon become insensitive. This cut-off wavelength λ_c is given by

$$\lambda_c = \frac{hc}{E_G}$$

(5-2)

where c is the speed of light, h Planck's constant and E_G the bandgap in the crystal.

The MOS-Capacitor

The basic building block of a CCD and hence the CCID-35 is the MOS (Metal Oxide Semiconductor) capacitor illustrated in Figure 5-1. A semiconductor is said to be doped if the atoms get deliberately replaced by other atoms with a different number of electrons in the valence band. If the impurity atom has more valence electrons it is called an n-type semiconductor and if the impurity atom has less valence electrons, the semiconductor is called a p-type.

MOS - capacitor structure of a burried channel CCD
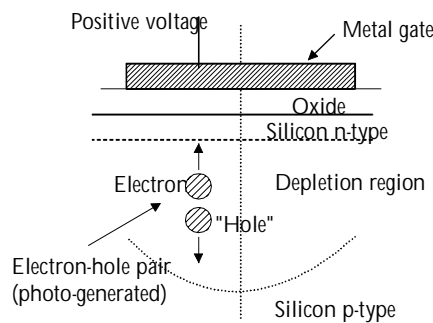
Figure 5-1 Schematic cross section of a buried channel capacitor.

On a wafer of p-type doped silicon also called the substrate, an n-type region usually around 1 μm thick is formed on the surface and then a thin insulating layer of silicon dioxide is grown thermally on the wafer surface. After this process a thin metal film or a heavily doped polycrystalline silicon layer is then evaporated on the insulator in a pattern to form a small MOS capacitor. The metal thickness is very small and therefore the photons can pass through the film with minimum attenuation. Hence a positive potential is applied to the gate, which is the metal film and the semiconductor bulk material acts like ground reference. The resulting structure behaves like a parallel plate capacitor and can therefore store electrons. If the MOS structure gets biased, the voltage will force holes away from the gate to create a depletion region. If the region is depleted, no charge movement is possible.

Now if photons pass trough the transparent metal electrode into the bulk material and generate photoelectrons, these photoelectrons get attracted towards the positive charged gates and move throughout the structure until they reach the silicon-silicon dioxide interface and stay at the interior surface of the MOS capacitor.

There are two types of MOS structures: surface channel and buried channel designs. All modern CCDs and therefore also the curvature CCD are buried channel devices with the advantage of keeping the photo-electrons confined away from the surface of the CCD where they could become trapped [Kim et al, 1972 and Walden et al, 1972]. The difference between the buried and surface channel capacitors is the presence or absence of the n-type layer; in the surface channel structure the potential maximum is located directly at the Si-SiO$_2$ interface whereas in the buried channel devices the charge is removed from the surface and hence can not interact with the interface states. This has the

advantage that the storage location (channel minimum) is positioned away from the silicon–silicon dioxide interface, deeper in the channel. Therefore the charge will not move near that interface during the transfer process and the transfer efficiency is improved. In the surface channel version the interfaces often suffer traps and surface states due to defects in the interface integrity.

<u>The energy band diagrams</u>

Figure 5-2 shows the electron energy and the electrostatic potential beneath the electrode for a typical buried channel capacitor at 3 different bias conditions.

An electron seeks usually a condition of lowest potential energy. The potential energy of the electron is given by

$$E_p = -|q|\Psi \ ,$$

(5-3)

where E_p is the electron energy and Ψ is the electrostatic potential and q is the magnitude of the charge on an electron. Thus an electron will seek a position where the local electrostatic potential is highest. For the unbiased or "flatband" condition as shown in Figure 5-2a, the number of electrons in the n-type region is characterized by the equilibrium Fermi level. The bands are flat and the electrostatic potential is uniform within the n-type region.

However, when the n-type region is fully depleted of electrons by a reverse bias voltage, a minimum occurs in the electron potential energy (Figure 5-2b) and a potential well is formed. The minimum is located within the n-type region and at some distance removed from the silicon-silicon dioxide interface. This minimum in the energy (or maximum in the potential) is, where excess electrons are collected.

Figure 5-2c now illustrates the situation where a bias voltage is applied to the gate with the substrate held at ground potential and some charge due to photoelectrons is collected in the potential minimum. The region where the charges collect is referred to as the channel since this structure is below the silicon surface. That's why the term buried channel is used. This potential in the channel is flat (i.e. the field is zero) in the region where the charge is collected. If it were not, the electrons would move in order to make the field zero in the channel.

<u>Single pixel structure</u>

Figure 5-3 shows three parallel polysilicon gates oriented orthogonal to two channel stop regions forming a single 3-phase CCD pixel. The buried channel is between the channel stop regions. Now having a potential more positive on the middle electrode than on the other two gates, a local potential energy minimum is formed under the middle gate. Hence the photoelectrons created within the potential minimum will be collected there. Electrons that are created in the channel stop region or in the substrate beneath the pixel may diffuse to the minimum and be collected. A CCD is then formed as an array of those structures. However there are also other formats for the CCD pixel.

There are structures that utilize two or four polysilicon gates to define a pixel and some even only use a single gate in combination with multiple implants to define the pixel. However, the technology most often used in the fabrication of scientific-grade CCDs is the three-phase structure.

Energy band diagrams for a buried channel CCD
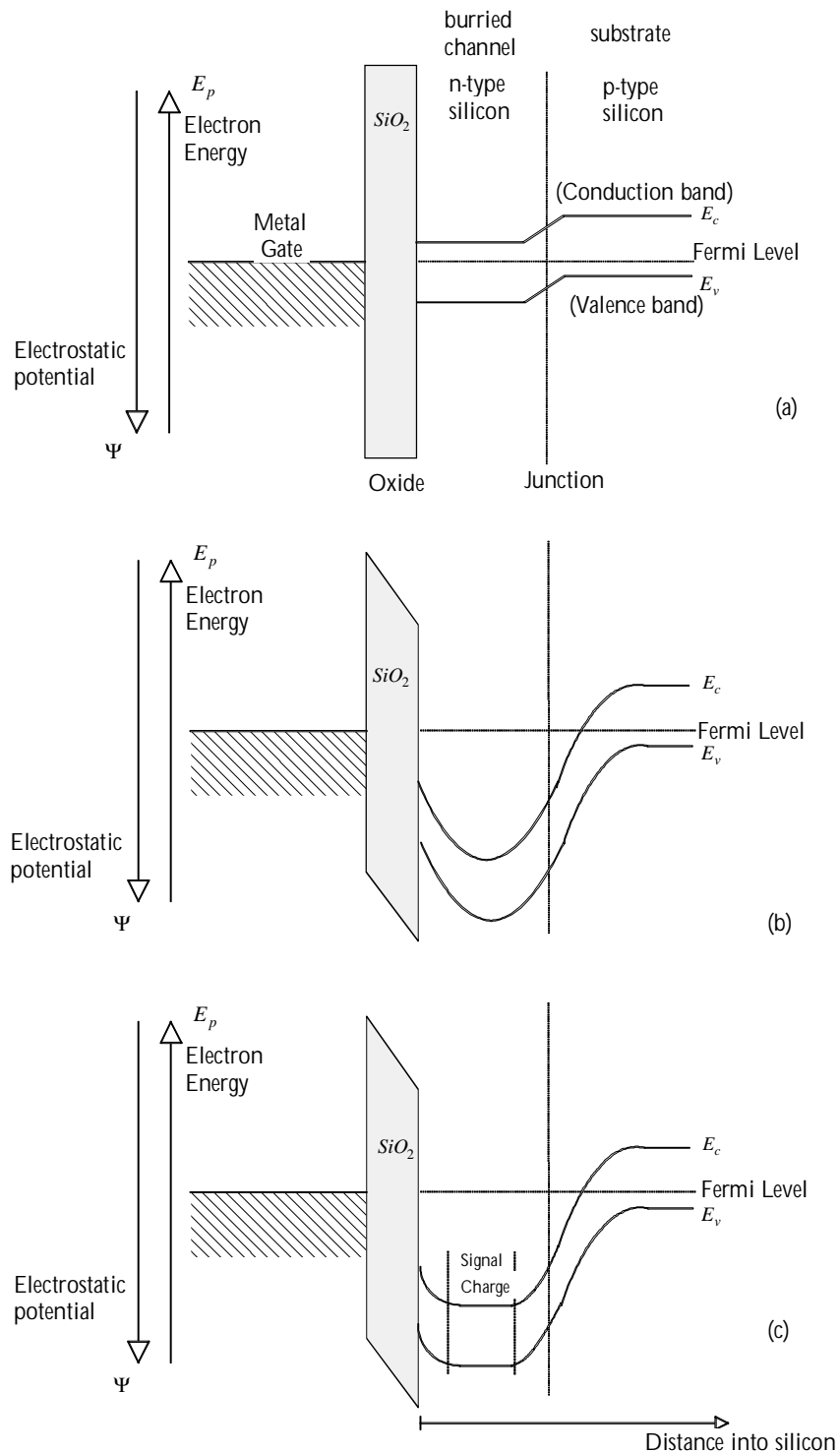
Figure 5-2 Energy band diagrams for a buried channel CCD - (a) unbiased condition, (b) n-type region is fully depleted, (c) bias voltage applied.

A single pixel of a buried channel CCD
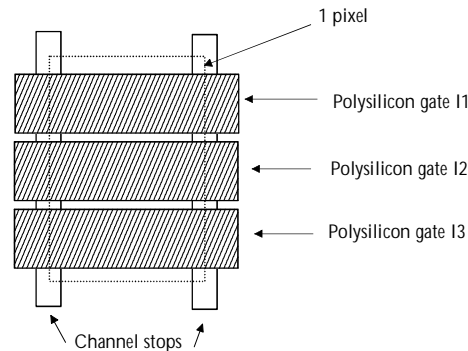
Figure 5-3 Schematic of a single pixel structure.

Charge Transfer Process

Figure 5-4 shows a schematic cross section of two cells of a three-phase buried channel CCD and the electron energy at the semiconductor-oxide interface for different applied clock voltages. There are three separate gates, named I1, I2, and I3 or clock 1, clock 2, clock 3. As shown in the Figure all I1 gates are connected to the same clock, also all I2 and all I3 share a common clock. During the integration time charge is collected under one of the gates. After an exposure the charge needs to be moved towards the output structure of the CCD. This charge transfer process is illustrated under the gate structure. Assuming that charge is collected beneath the I1 electrodes a simple scheme of clock pulses is applied to the gates to move the charge from one pixel to the next. Such clock cycles are repeated to readout an entire N-pixel linear registers for parallel or serial movement.
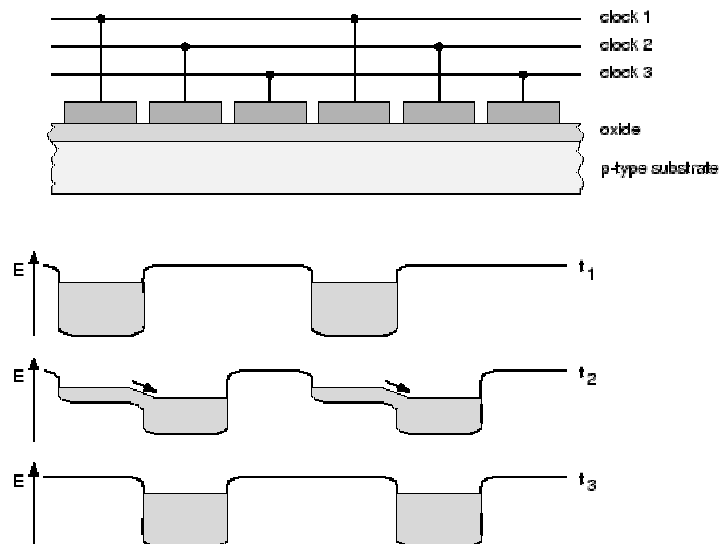
Figure 5-4 Schematic cross section of two cells of a three-phase, n-channel CCD and electron energy at the semiconductor-oxide interface for different applied clock voltages.

At all times within a single pixel, a barrier to the next pixel exists. These are required in order to store the charge and to maintain the uniqueness and identity of each charge packet. Note that by interchanging the roles of any two of the gates the charge will move in the different direction. This flexibility is clearly an advantage of the three-phase process and is needed also for the curvature CCD.

As a summary it can be said that the CCD has four fundamental functions, which are charge detection via the photoelectric effect, charge collection, charge transfer with the CCD potential well and charge detection with a sense node capacitance which converts the charge into a voltage. These MOS capacitors form the basic structure of the CCD and are then arranged into a device. Clock pulses applied to the gates modulate the channels and produce moving potential wells, which can store or transfer charge packets. The clocking of the curvature CCD will be explained in detail at the end of this chapter.

All these basic principle apply to the design of the curvature CCD. Following the architecture with the amplifiers and functional wiring of the complete CCID-35 **device** is presented. The architecture starts with the definition of a unit cell of the curvature CCD.

5.2 Layout of one unit cell
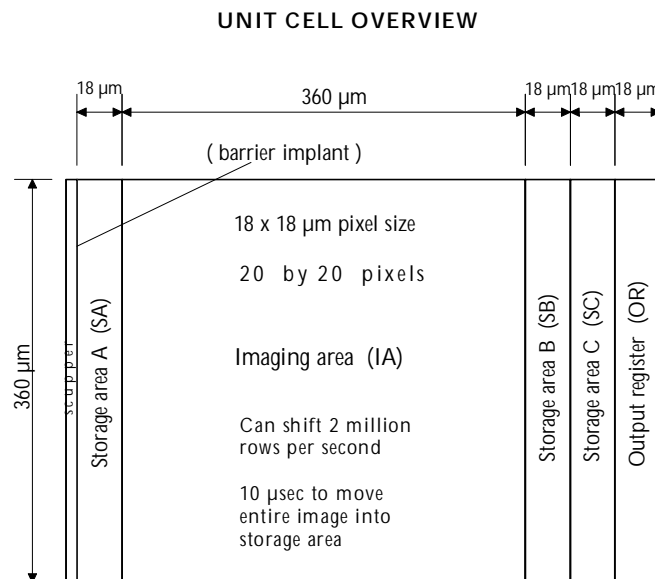
UNIT CELL OVERVIEW

Figure 5-5 Unit cell overview.

Figure 5-5 shows a functional drawing of a **unit cell**, with an integration area made of 20 x 20 pixels, each 18 µm square. These form an **imaging area** (IA) of 360 by 360 µm for each subaperture, large enough to focus the light without optical crosstalk to other pixels. These pixels will be binned by rows into the storage areas SA and SB. The storage areas are small compared to the imaging area, being only one pixel wide.

The SA and SB storage areas are used as a memory to store charge from the imaging area for multiple cycles of the membrane. After integration is completed the charge is moved into SC and then into the serial register for readout.

The complete imaging area can be shifted into a storage area within 10 μsec, during the relatively flat portion of the membrane oscillation, i.e. when $|f_m| > 3$ m, as discussed in chapter 3.

A minimum number of clock phases is used to move and store the charges in the storage areas. Storage SA and SB have only 2 phases to store and move the charge. Three phases are needed for the storage area SC (SC1, SC2, XG), since a transfer gate is required as a barrier between SC and the serial register (see Figure 5-6).
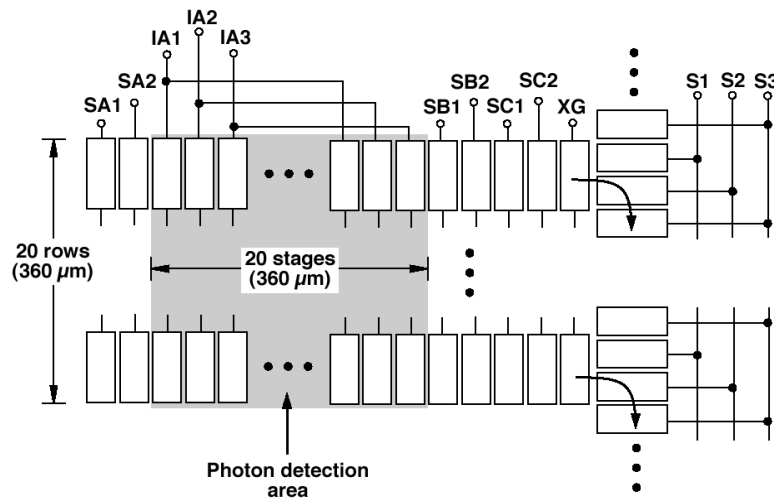
Figure 5-6 Superpixel architecture.

5.3 Layout of one unit column with associated readout amplifier

Figure 5-7 shows the layout of one **unit column**. Ten unit cells in the vertical direction are combined to form one unit column. There are only 3 prescan pixels in the serial register (see Figure 5-8). Since each unit column is a collection of 10 unit cells and only 8 of the unit cells are needed, we have the possibility to leave the first 2 cells empty to "warm up" the electronics for the 8 cells with light. If there is no need to warm up the electronics, the spots are put close to the output amplifier and hence the warmup time is saved. In addition the two extra cells will gave flexibility to avoid cells with traps.
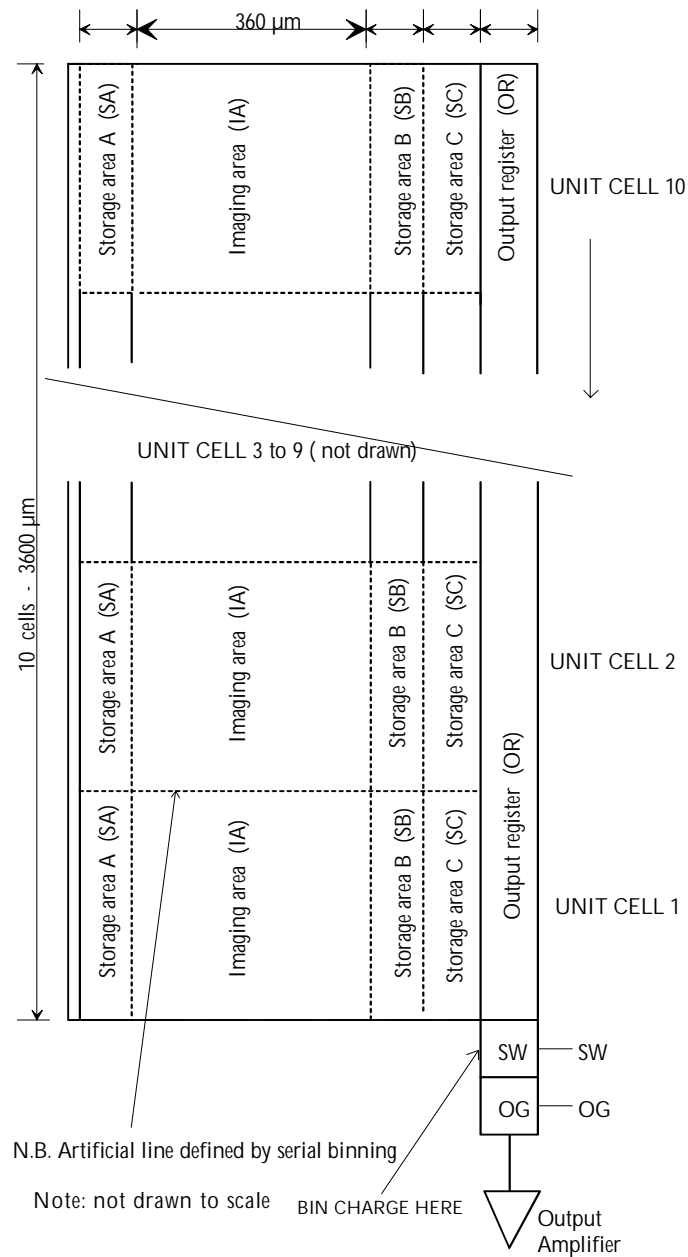
Figure 5-7 Unit column design - 10 combined unit cells with the output amplifier.

Note that the borders of the unit cells are only artificial and are defined by binning in serial direction. If the spots are small, even more subapertures can be defined within a singe unit column. The next Figure shows a schematic drawing of the unit column with the clock phased needed before the output amplifier circuit and also the phases needed for the output structure. The output structure will be explained in more detail further on.
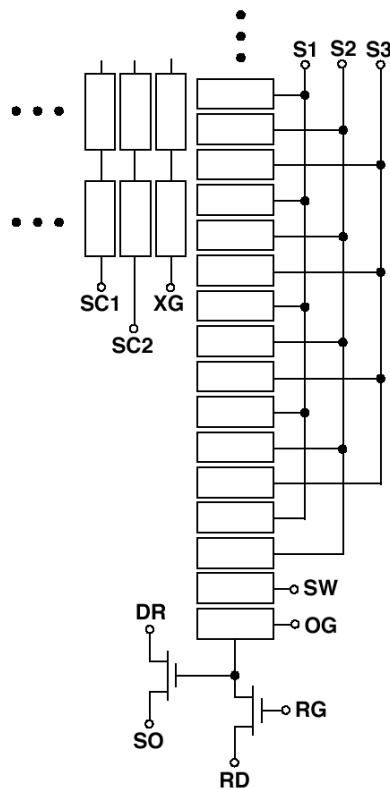
Figure 5-8 Unit column design - schematic diagram with the clock phases and output amplifier circuit.

5.4 Tip/tilt sensor

Simulations showed that for a 60-element curvature system Strehl is improved with separate tip/tilt sensing. The CCID-35 also includes a tracker chip to be used as a tip/tilt sensor. The tracker chip simply integrates charge and reads out; there was no need for storage area SA, SB and SC.

The tip/tilt sensor only has clocks IA1, IA2 and IA3 and XG. The tracker is a bit wider (24 pixels) since we expect to get at least 50 photoelectrons into each "cell" of the tracker chip; the extra rows provide tolerance for alignment and the use of larger fibers. Since we only need 4 subapertures in the tracker, it has a reduced length of 160 pixels.

The tip/tilt sensor is clocked completely independent of the curvature WFS CCD portion of the device. One can integrate and read out this tip/tilt array at a different rate, although for noise reasons it might be useful to synchronize the clocks of both arrays.

Detail layout design of one column of the CCID-35
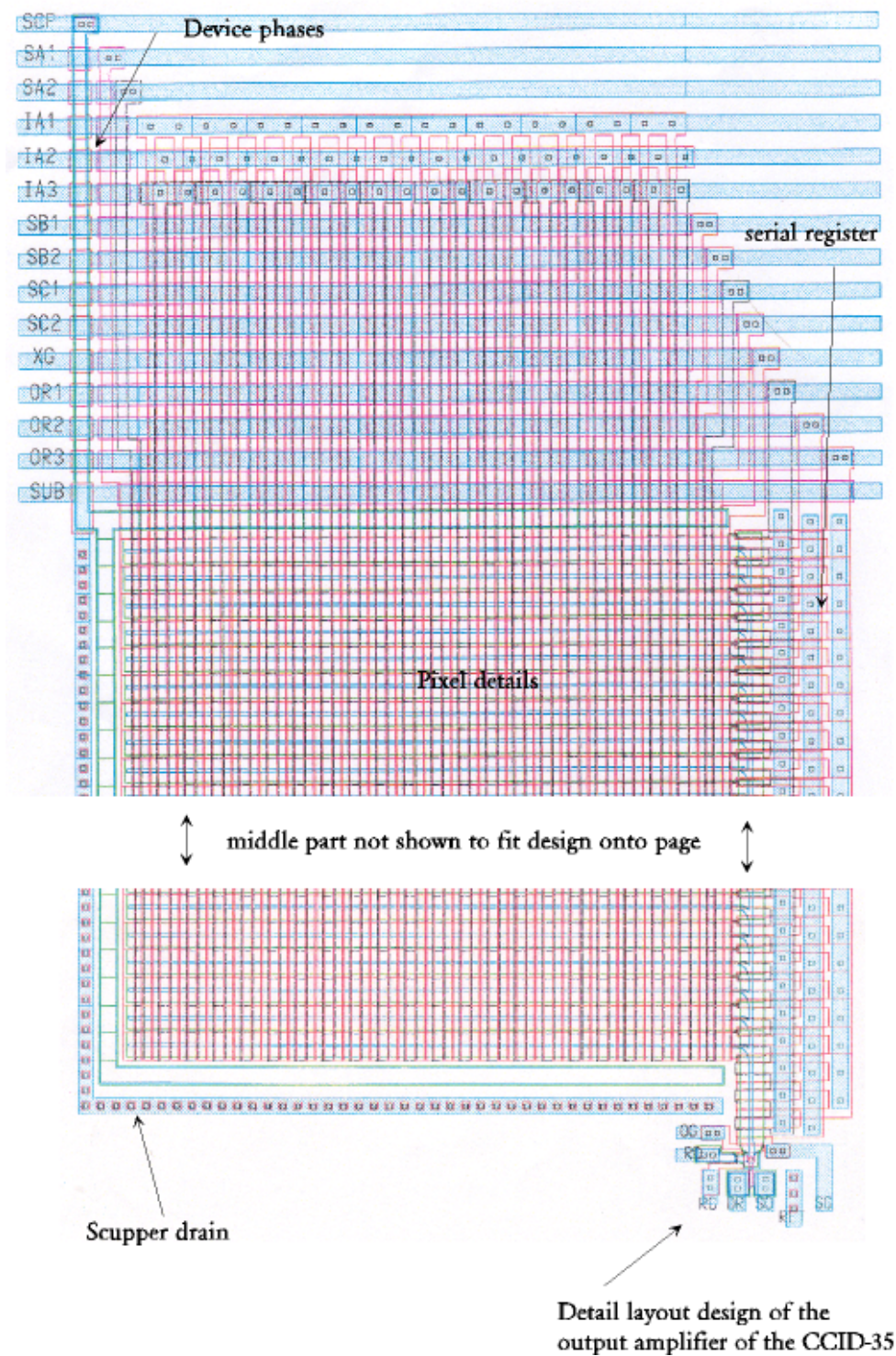
Figure 5-9 Layout of the CCD design for a unit column and the output amplifier design.

5.5 Layout of the complete curvature CCD

To summarize the design, each superpixel consists of 20 x 20 pixels, where a pixel is 18 x 18 microns in size. The total height of each column is 10 superpixels or 200 pixels. There are 8 columns for a total of 80 superpixels and an independent tip/tilt sensor array. Figure 5-10 shows the CCD design of the curvature wavefront sensor array and Figure 5-11 a picture of the CCD. The total width of each unit column, including the gap, is 550 μm.

There are substrate ground connections between the output circuit and the bottom of the imaging pixels to ensure good isolation of the clock waveforms from the output circuit. There is a **scupper** on the chip between each column to keep stray photocurrent and dark current from leaking into the pixels.

Experience with the CCID-20 [Dorn et al, 2000] was that its 3 micron wide scupper does not fully capture all stray electrons. Therefore the scupper on the CCID-35 was made 10 microns wide. The output gates from the 8 outputs of the curvature array are connected together on the chip to minimize the pin count and simplify packaging.

All of the corresponding clocks and bias lines for all unit columns are wired together on chip. Also the corresponding drive voltages for the amplifiers circuits are wired together. Only the drain voltages for the output amplifier are brought out separately to be able to optimize noise and linearity for each amplifier individually (see Appendix B for a picture of the CCID-35 die).
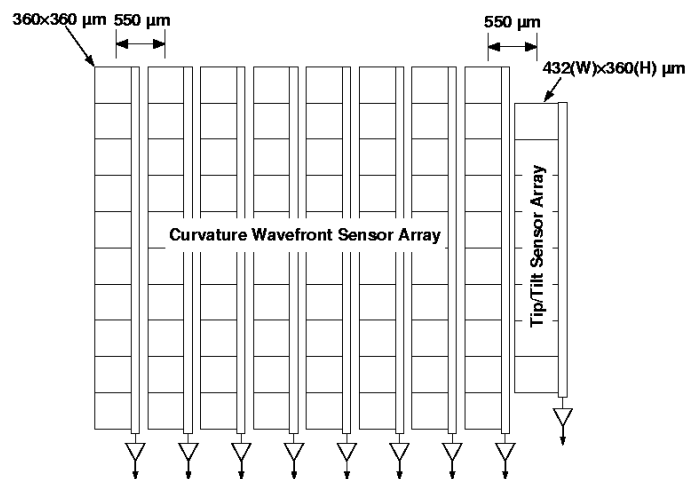
Figure 5-10 CCD design - curvature wavefront sensor array. The design consists of 80 unit cells. Ten unit cells are combined into a unit column. Each of these unit columns has an amplifier at the "bottom" end of the serial register. On the right side of the device is the tip/tilt sensor.
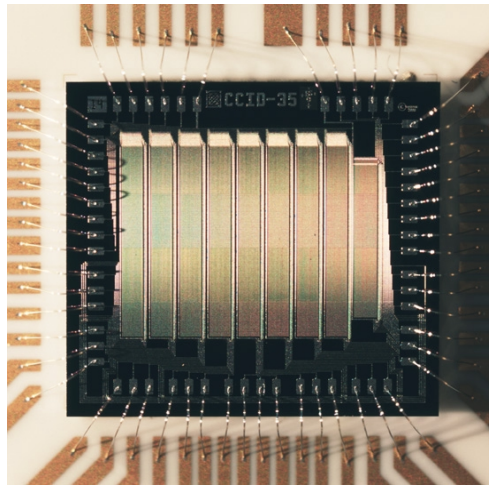
Figure 5-11 Picture of the real device with bonding wires.

5.5.1 Output amplifier design

The **read noise** for the CCD should be as low as possible, preferably under 2 electrons at 50 kpixel per second. To achieve this, the CCD electronics are operated at high gain (0.2 to 0.3 electrons / digital number). We decided to put the same amplifier on the CCD as for the MIT/LL CCID-20 [Dorn et al, 2000]. This is a conventional floating diffusion amplifier or gated charge integrator.

Figure 5-12 CCID-35 amplifier design.
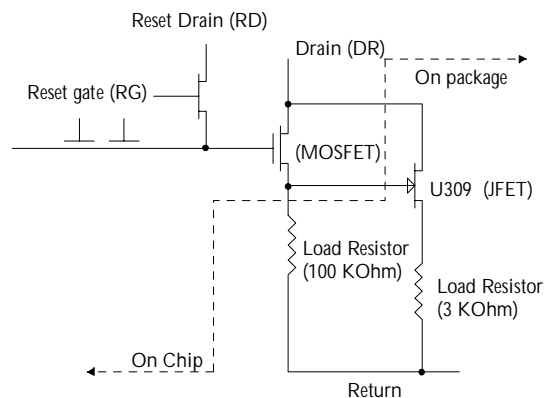
A JFET transistor, a U309, follows the output of the MOSFET. The U309 is located off chip and boosts the signal to the preamplifier. A sensitivity of around 15 to 20 µV per electron was expected. Figure 5-12 shows the schematics of the amplifier design and Figure 5-9 the layout of the amplifier on the CCD.

Parallel shift speed up to 3 MHz and serial shift speed up to 4 MHz is possible with this device, more than fast enough for a 2 kHz membrane frequency. With the high responsivity of the MIT/LL amplifier design, the amplifier full well was calculated to be around 100,000 electrons. We expected good **linearity,** better than 1%, up to the full well.

5.5.2 Charge transfer efficiency (CTE)

CTE is a measure of how effective the charge stored in the individual pixels is moved within the device. Problems usually occur when the potential wells are (a) almost empty or just have a small charge package stored, (b) the potential wells are filled up with lots of electrons and (c) when the CCD has defect pixels or other cosmetic problems. Since the CCID-35 will work most of the time with very low charge packages at low flux levels, achieving good CTE at low light levels was a very important issue in the design of the CCD.

To be able to move single electrons with good charge transfer efficiency, there is a notch in the channel. This is a standard feature of the CCID-20 and it reduces the ability of traps to capture electrons. This notch or trough is 2 microns wide in the image pixels and 3 microns wide in the serial pixels.

The charge transfer inefficiency (CTI), for Fe-55 (1620 e-), was measured for a CCD of similar design to be $< 10^{-6}$ [Burke, 1999]. Measuring CTI for 2 electron charge packets is more problematic. However MIT/LL has measured CTI on proton-irradiated parts as a function of packet size down to 30 e- and found that the CTI varied approximately as the packet size to the -1/2 power. Assuming this variation is true for packets as small as 2 electrons, one would expect CTI $< 3 \times 10^{-5}$. For 200 transfers this implies 99.4% cumulative transfer efficiency.

5.5.3 Cosmetic quality

The CCID-35 was manufactured on 150 mm (in diameter) silicon wafers together with other CCD devices at MIT/LL in Boston/USA. The mask set layout for this wafer run is shown in Figure 5-13 and Appendix A shows a picture of the wafer. In the first wafer run 6 wafers were process with each wafer having twenty CCID-35s, ten in the left upper and ten in the right upper corner of the wafer.

After the initial process two wafers were used to dice up frontside versions of the CCDs for packaging and testing. The remaining four wafer went then through the thinning process at MIT/LL. The **cosmetic quality** of the CCD is an important issue for this application. Since the CCD is small and 120 devices were produced in the first wafer run, we expected to be able to test and find devices that are cosmetically perfect.

5.5.4 Quantum efficiency (QE)

Charge coupled devices are thinned to enhance quantum efficiency. On the frontside version of the CCD the photons have to pass through the overlying electrode structure in order to reach the depletion region in the silicon. This results in poor response due to the absorption in the polysilicon gate electrodes. Furthermore the near infrared response is poor due to the thinness of the epitaxial layer in the devices.

To enhance the response, the CCDs are turned over and illuminated from the backside without the disturbance of the gate structure. This requires thinning the silicon substrate not to absorb the photons before interacting with the epitaxial layer.

WAFER LAYOUT MASK SET
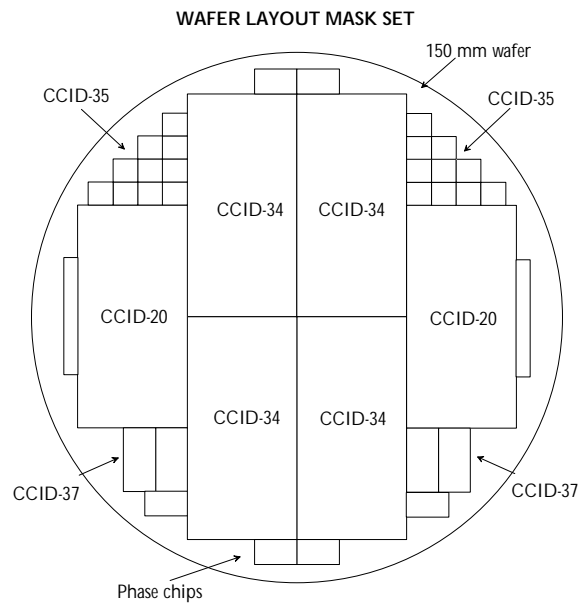
Figure 5-13 MIT/LL wafer layout mask set with the curvature CCDs.

The CCID-35 gets thinned to approximately 20 μm. The frontside versions have a thickness of 675 μm. Figure 5-14 illustrates the difference between frontside and backside illuminated CCDs. By thinning the CCDs more, the red response will be reduced since the red photons need a certain absorption length in the device. If too thin, the red photons would pass through without interacting with the photosensitive layer. After the thinning process the CCDs get coated with an anti-refection coating. This is done on the complete wafer before the individual devices get diced up for packaging.

Frontside (front-illuminated) CCD   **Thinned (back-illuminated) CCD**
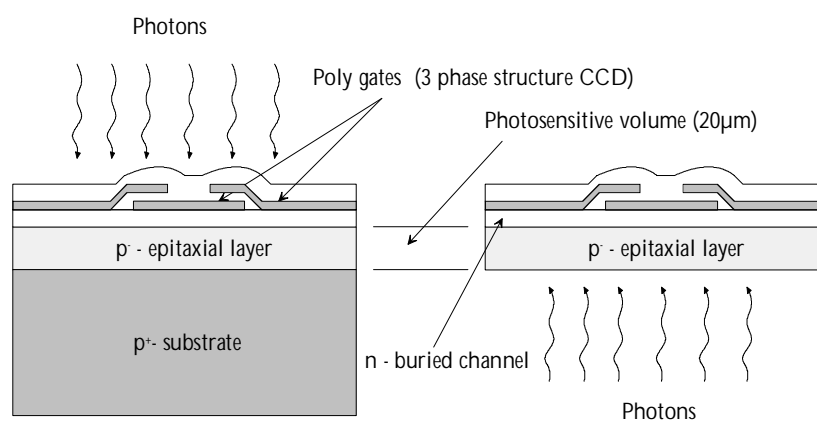
Figure 5-14 Frontside and backside illuminated CCDs.

For the thinned, back illuminated CCID-35 devices, there will be the same anti-reflecting coating as for the MIT/LL CCID-20 (QE peak up to 90%). Figure 5-15 shows the quantum efficiency measurement of a CCID-20 [Dorn et al, 2000]. For the thinned back illuminated versions of the CCID-35 an equal or better QE is expected.

Expected quantum efficiency of the CCID-35 for curvature
wavefront sensing
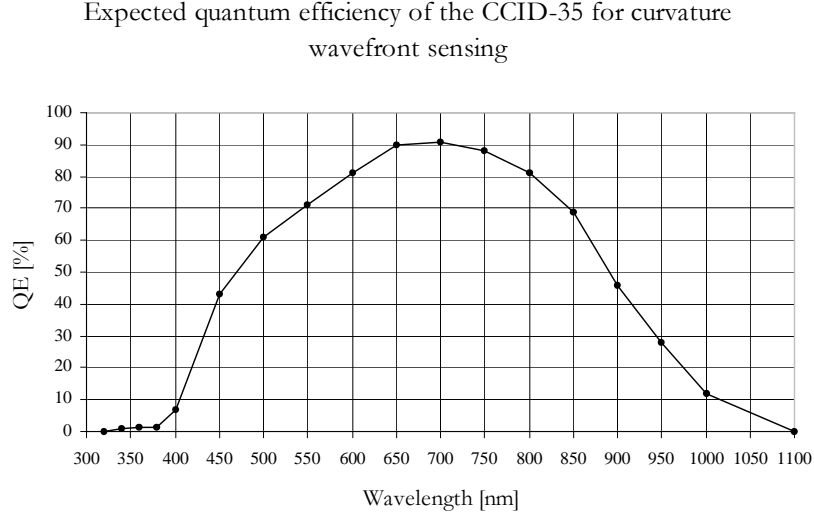
Figure 5-15 CCD design - expected quantum efficiency.

5.5.5 Dark current

A very important requirement for the curvature AO CCD is the reduction of **dark current** to a negligible level. For the 360 x 360 micron superpixel we want to have less than 0.25 electron dark current per frame, so that readout noise dominates. The slowest frame rate we will operate the device is 50 Hz, a frame time of 20 ms. Figure 5-16 shows the calculated dark current versus temperature using the following equation [Janesick, 2001]:

$$N_d = 2.5 \cdot 10^{15} N_o d_{pix}^2 \ T^{1.5} e^{\frac{-E_g}{2 k T}},$$ (5-4)

where N_d is in electrons/pixel/s, N_0 is the dark current in nanoamps per square centimeters at room temperature (T_o), d_{pix} is the pixel size in centimeters, T is the operating temperature in Kelvin, E_G is the band gap energy in eV and k is the Boltzmann constant.

For the CCID-35 we assumed N_0 to be 1 nA at a room temperature of 300 degree Kelvin. The band gap energy varies with temperature and is given by

$$E_g = \frac{7.021 \cdot 10^{-4} T^2}{1108 + T}$$ (5-5)

In Figure 5-16, the dashed line is dark current per superpixel per 20 ms, the solid line is dark current per pixel per second. The CCD must be cooled to a temperature of 192

degree Kelvin or - 81°C to achieve a dark current of less than 0.25 electrons per superpixel at 50 Hz frame rate. Thus we used liquid nitrogen to cool the CCD.

Calculated dark current for the MIT/LL CCID-35

solid line:
dark current [e-/pixel/s]

dashed line:
dark current [e-/superpixel/20 ms]

Dark current

Temperature [k]
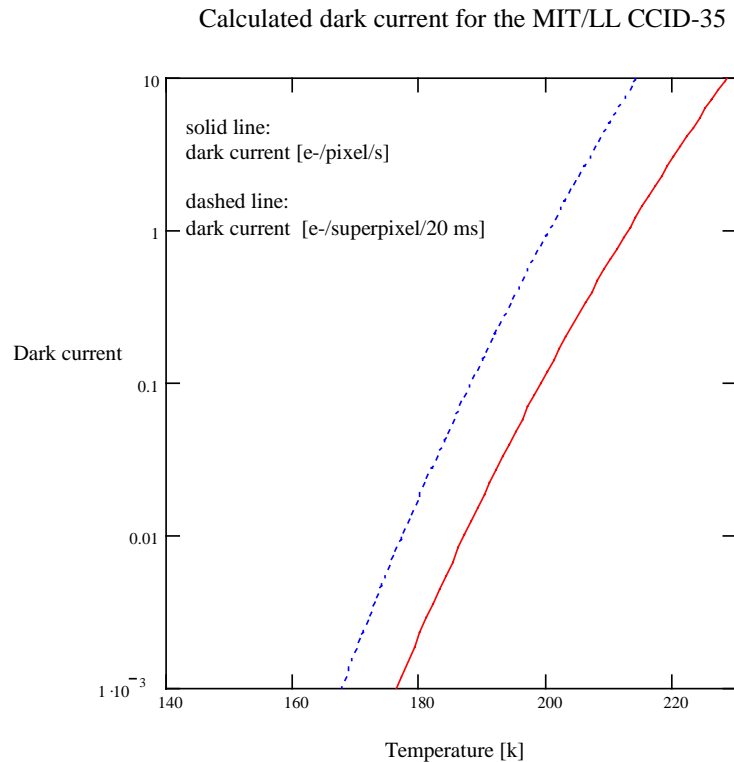
Figure 5-16 Calculated dark current for the CCID-35.

5.6 Package and dimensions

The CCD was glued onto a ceramic board and then integrated into a 72 pin kovar package. The 100 kOhm load resisters for the output amplifiers and the U309 JFET transistors are also mounted in the package (c.f. Figure 5-17). A picture in Appendix C shows the final layout of the package for the fronside device.

5.7 Summary of expected CCD performance

Readout noise

The serial register of the CCD can be clocked at 3 MHz rate with no degradation of CTE. Thus, it will take about 70 µsec to move all 200 pixels of one unit column through the serial register. For a 250 µsec half-cycle of the 2 kHz membrane there will be 180 µsec available for reading the 10 superpixels of a unit column, i.e. a pixel readout rate of 18 µsec

per pixel. At this rate, with high electronic gain (0.1 to 0.25 electrons per digital number), we expected to achieve ≤ 2 electrons noise.

Dynamic range

A good feature of the curvature CCD is its high dynamic range. For low light level situations, all photoelectrons of a subaperture will be binned into a single pixel. However, for bright objects, 20 pixels can be read out for each subaperture in each 250 μsec half-cycle. Assuming that 10 pixels of each subaperture are filled to an average level of 75,000 electrons every half cycle, this is comparable to 3000 million photoelectrons per subaperture per second. The curvature WFS CCD has a dynamic range that is more than 1000 that of APD modules – while being linear to 1% over the entire range.

Field of view

Another good feature of the curvature CCD is its ability to sense a large field of view. A 100 μm core fiber being used in the initial testing is very conservative and is primarily being used to match the fiber used for APD modules. However it is important to note that a 200 μm core fiber would be feasible, which would result in a 6 arcsec field of view, double that accessible to an APD WFS system. After the non-redundant engineering phase of the CCD was completed, we believe that we had designed a CCD that can be used for curvature wavefront sensing in astronomical AO systems and that this CCD will achieve nearly the same AO system performance as an APD-based WFS. A picture of the frontside device implemented in the package is shown below.
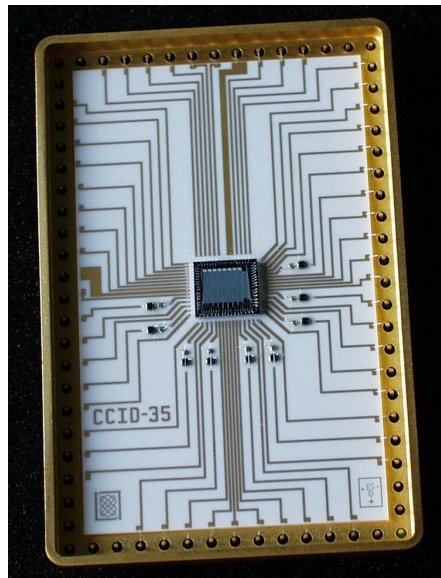
Figure 5-17 Picture of the frontside CCID-35, the curvature CCD.

5.8 Operation of the curvature CCD

Depending on the light level, the atmospheric seeing conditions and the desired update frequency for the correction of the wavefront distortions in an adaptive optics system, the CCD needs to be operated in different readout modes. Assuming a membrane frequency of 2 kHz, the typical update frequency for the MACAO system deformable mirror for the VLTI is 350 Hz, i.e. 2.86 ms and the slowest update frequency required for the VLTI is 150 Hz [Arsenault, 2001].

However, depending on the magnitude of the guide star, the curvature sensor will need to be able to operate between 50 to 2 kHz to be able cover all possible readout requirements also for other instruments. Hence the CCD needs to sum up the extrafocal and intrafocal photons for more than one halfcycle and to store this charge while integrating other halfcycles.

5.8.1 Timing and readout modes

The three memory areas SA, SB and SC are used to store the charges for more than one cycle before the electrons are moved to the serial register to read them out. It was important to implement "on-chip" storing onto the device to avoid, that the device needs to be read out every half cycle. Reading the CCD every half cycle would add up the readout noise per readout.

Following we will discuss a typical operation scheme for the curvature CCD at a frame rate of 2000 Hz (i.e. every 2 cycles). This is a desired mode in practical operation. Figure 5-19 shows a typical timing. The Figure shows the membrane amplitude versus time and the drawings on the bottom the required shifting and storing of the charge. Arrows in the desired direction indicate the charge movement.

The diagrams show the status while integrating the light for the membrane from the flat to the convex or concave shape and back and the time for the parallel shifting when the membrane is near the flat status. In this example a half a cycle lasts 250 µs. The summed charge [I_1 and I_1^*] over the positive amplitude and the summed charge [I_2 and I_2^*] over the negative amplitude are read out each in 240 µs. Those signals are needed to calculate the normalized difference, which is proportional to the desired curvature information. However this implies a readout delay of the curvature CCD of 240 to 250 µs. On contrast, APDs deliver the signals instantaneously.

To program this readout mode, the sequence for operating the CCD was split into several subsequences:

o   One which cleared the serial register from unwanted charge when the CCD was not read out and for integration during the membrane movement.
o   Two subsequences for shifting the charge from the imaging area into storage pixels SA or SB.
o   Two subsequences to either shifting the charge from IA into storage SB and SR or to shift the charge from IA into storage SB and SR.
o   Finally one subsequence for reading out the serial register and integration.

Hence those subsequences were combined into the following readout sequence:

```
SEQUENCE cws_2_cycles                      sequence name

  pixel_x = 12                             number of pixels in x + 1 prescan and 1 pipeline)
  pixel_y = 16                             number of pixels in y
  pixel_order = "0 ,1 ,2 ,3 ,4 ,5 ,6 ,7"   order of readout ports

START OF SEQUENCE LOOP

{
  parallel_shift_oneline_SB 20 1;          shifts charge from imaging area into storage SB
  serial_shift_int_20x_non_convert 12 1;   clearing of serial register and integration
  parallel_shift_oneline_SA 20 1;          shifts charge from imaging area into storage SA
  serial_shift_int_20x_non_convert 12 1;   clearing of serial register and integration
  parallel_shift_oneline_SB_SR 20 1;       shifts charge from IA into storage SB and SR
  serial_shift_int_20x 12 1;               reading out serial register and integration
  parallel_shift_oneline_SA_SR 20 1;       shifts charge from SA and IA into SB and SR
  serial_shift_int_20x 12 1;               reading out serial register and integration
}

END OF SEQUENCE LOOP
```

The pixels in the integration area are binned into one superpixel and the charge is shifted within 20 µs either into the serial register or the storage pixels. This is done during the time when the membrane is almost flat. For a 2 kHz membrane oscillation and f_{min} = 25 cm, there are 13 µsec during each half cycle when $|f_m(t)| > 3$ m as outlined in chapter 4. Thus there are more than 10 µsec each half-cyle to allow the detector to switch between intrafocal and extrafocal integration states. This is done during the even times shown in Figure 5-18.

To readout the serial register within the remaining 240 µs, the pixels in the serial register are binned also 20 times and readout. Due to electronic there is one additional pixel to be read which is an artifact in the FIFO pipeline of the analog to digital converter. The 3 prescan pixels are also binned to one "prescan superpixel" and hence 12 pixels need to be read out within the 240 µs. This requires a readtime of 20 µs per superpixel or 50 kHz. This was an important design parameter for the curvature CCD to be able to read the serial register relatively slow to be able to achive a readout noise less than two electrons rms.

However the readout time is a delay of 240 µs to update the curvature signal to the deformable mirror and cannot be avoided with the curvature CCD.

Example of CCD operation for a 2 cycle integation mode with the curvature CCD

End of first
2 cycle
integration

End second
2 cycle
integration

Membrane
Amplitude

time 2   time 4   time 6   time 8   time 10   time 12   time 14   time 16

$[I_1]$ $[I_{1'}]$ $[I_3]$ $[I_{3'}]$ $[I_5]$

$[I_2]$ $[I_{2'}]$ $[I_4]$ $[I_{4'}]$ t [s]

time 1   time 3   time 5   time 7   time 9   time 11   time 13   time 15

Time 1,3,5,7,9,11,13,15 (240 us)
Time 2,4,6,8,10,12,14,16 (20 us)

READOUT   READOUT   READOUT
SERIAL   SERIAL   SERIAL
REGISTER   REGISTER   REGISTER

Time 1,3,5,7,9,11,13,15 etc. (240 us)

During the integration time in the curvature mode (i.e. integrating the extrafocal and intrafocal photons [I1] or [I2]), the charge is collected in the integration area of the CCD. The charge in the storage section is kept and not moved within the device. The serial register is clocked to clear the charge (wipe) the register from unwanted electrons if not reading out.

Time 2,10,18, etc. (20 us)

During the shift time 2, 10 , 18 etc, in the 2 cycle mode the charge in the imaging area is shifted within 20 µs in the storage area SB while the charge in storage area SA is kept is during this movement.

Time 2,10,18, etc. (20 us)

During the shift time 4, 12 , 20 etc, in the 2 cycle mode the charge in the imaging area is shifted within 20 µs in the storage area SA while the charge in storage area SB is kept during this movement.

Time 6, 14, 22, etc. (20 us)

During the shift time 6, 14 , 22, etc. in the 2 cycle mode the charge in the imaging area is shifted within 20 µs in the storage area SB, SC and the serial register SR while the charge in storage area SA is kept is during this movement.

Time 8, 16, 24, etc. (20 us)

During the shift time 8, 16 , 24, etc. in the 2 cycle mode the charge in storage area SA and the charge the imaging area is shifted within 20 µs via the the storage area SB, SC (during this time no charge is stored there) into the serial register SR to be read out.

STORAGE A   IMAGING AREA   STORAGE B   STORAGE C   SERIAL REGISTER

Figure 5-18 Example of principle operation.

5.8.2 Clocking of the CCD device

To move the charge stored in the pixels of the CCD, clocking pulses are needed for the different phases of the CCD. Table 5-1 and Table 5-2 list the different phases of the curvature CCD and the tracker for tip/tilt sensing.

Clock phases curvature array	naming
Imaging area phase 1	IA 1
Imaging area phase 2	IA 2
Imaging area phase 3	IA 3
Storage area A phase 1	SA 1
Storage area A phase 2	SA 2
Storage area B phase 1	SB 1
Storage area B phase 2	SB 2
Storage area C phase 1	SC 1
Storage area C phase 2	SC 2
Storage area C barrier phase	XG
Output register phase 1	OR 1
Output register phase 2	OR 2
Output register phase 3	OR 3
Summing well	SB
Reset gate	RG

Table 5-1 Clockphases for the curvature CCD.

Clock phases tip/tilt sensor	naming
Imaging area phase 1	T_IA 1
Imaging area phase 2	T_IA 2
Imaging area phase 3	T_IA 3
Output register phase 1	T_OR 1
Output register phase 2	T_OR 2
Output register phase 3	T_OR 3
Summing well	T_SG
Reset gate	T_RG

Table 5-2 Clockphases for the tracker CCD.

Figure 5-19 and 5-20 show the required timing waveforms for the CCD to operate in curvature mode. The arrows in the diagrams indicate the charge movement forced by the clockpulses.

For the movement of charge in the serial register it was important that the curvature CCD features a summing well to sum up the charges of the twenty pixels before it gets dumped onto the output node structure of the amplifier. Clocking causes a feedtrough to the videosignal of the CCD output amplifier, which usually increases readnoise. Due to the summing well it is possible to compensate the effect of this feedtrough by leaving the summing well a bit longer positive biased and hence the signal more time to settle before being dumped onto the output node.

Clocking example for the charge movement of the curvature CCD (parallel movement)

Moving charge of one pixel in the imaging
to the storage area SA

Moving charge of one pixel in the imaging
to the storage area SB
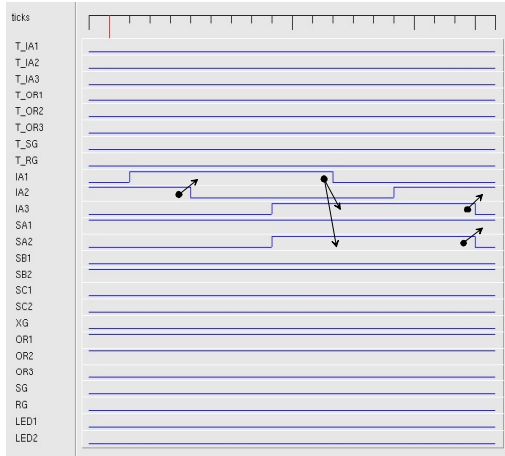
(a)
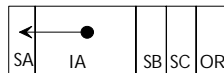
Note that stored charge under SB is
kept during this movement
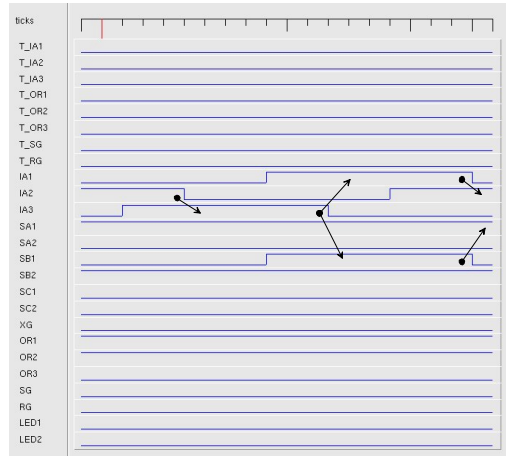
(b)

Note that stored charge under SA is
kept during this movement

Moving stored charge from storage area SA
and charge of one pixel in the imaging via SB
and SC into the serial register OR

Moving stored charge from storage area SB
and charge of one pixel in the imaging via
SC into the serial register OR
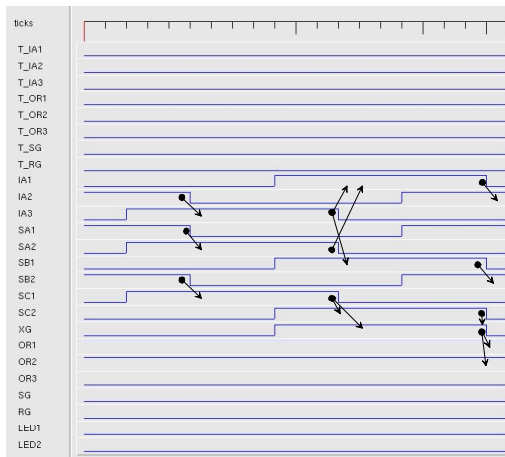
(c)
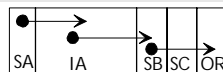
Note that stored charge under SB is
also moved into the serial register
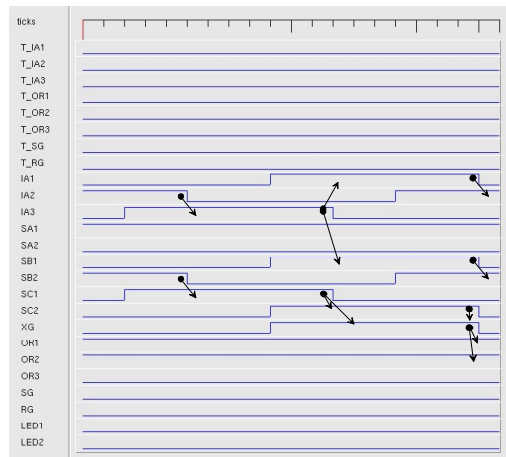
(d)

Note that stored charge under SA is
kept during this movement

Figure 5-19 Illustration of parallel timing waveforms required for the curvature CCD.

Clocking example for the charge movement of the curvature CCD (serial movement)
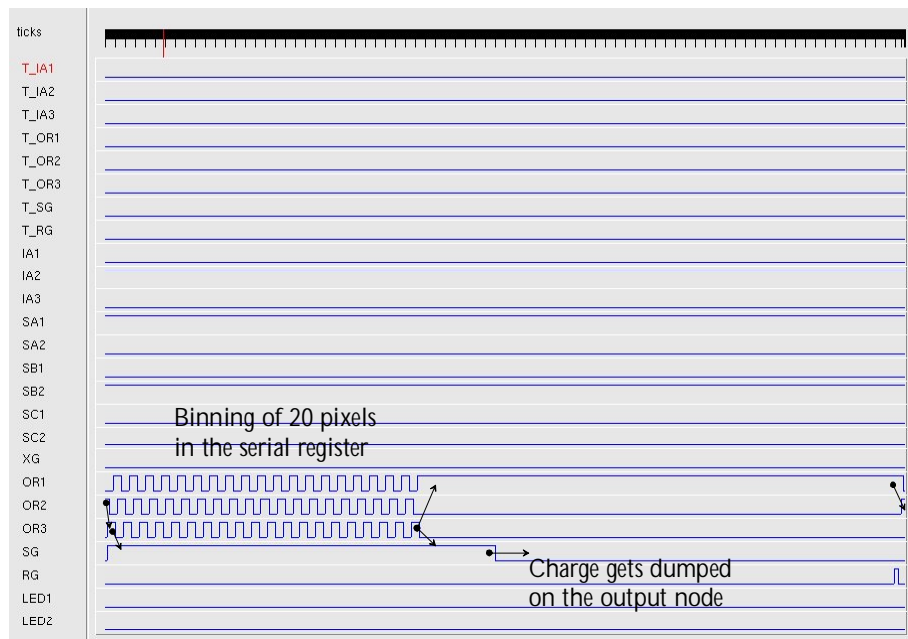
Charge of 20 pixels in the serial register is binned and summed up in the summing well SG. The charge is then dumped on the output node of the amplifier and sampled before reseting the amplifier serial register. Charge movement is from OR1 to OR2 OR3 and then onto the summingwell. Storage phases SA1, SB2 and the imaging phase IA2 are kept high during clocking the serial register.

Figure 5-20 Illustration of serial timing waveforms required for the curvature CCD.

5.8.3 Examples of readout modes

To illustrate the functionality of the curvature CCD, following four examples of readout modes are shown.

Figure 5-21 shows a dark frame of the curvature CCD in the non binned mode. Per readout port 200 image + 10 overscan pixels (including 3 prescan and 1 pipeline) are read out in the serial register and 20 image + 4 overscan pixels are read for the parallel lines.

Figure 5-22 shows the same image but with the 60 spots of the fiberfeed projected via the Oeffner relay optics onto the CCD.

Figure 5-23 shows an unbinned image with the charge for 10 extrafocal times stored in the storage pixels SA and the charge for 10 intrafocal times stored in the storage pixels SB. The light flux was kept constant during those exposures and hence the same amount of charge was stored in SA and SB.

Finally Figure 5-24 shows the CCD in curvature mode, i.e. the pixels were binned 20 x 20 with the charge for 10 extrafocal times stored in the storage pixels SA and the charge for 10 intrafocal times stored in the storage pixels SB and then read out. For better visualization the parallels lines are overscanned by two superpixels.

CCD image (0 second exposure) in unbinned mode
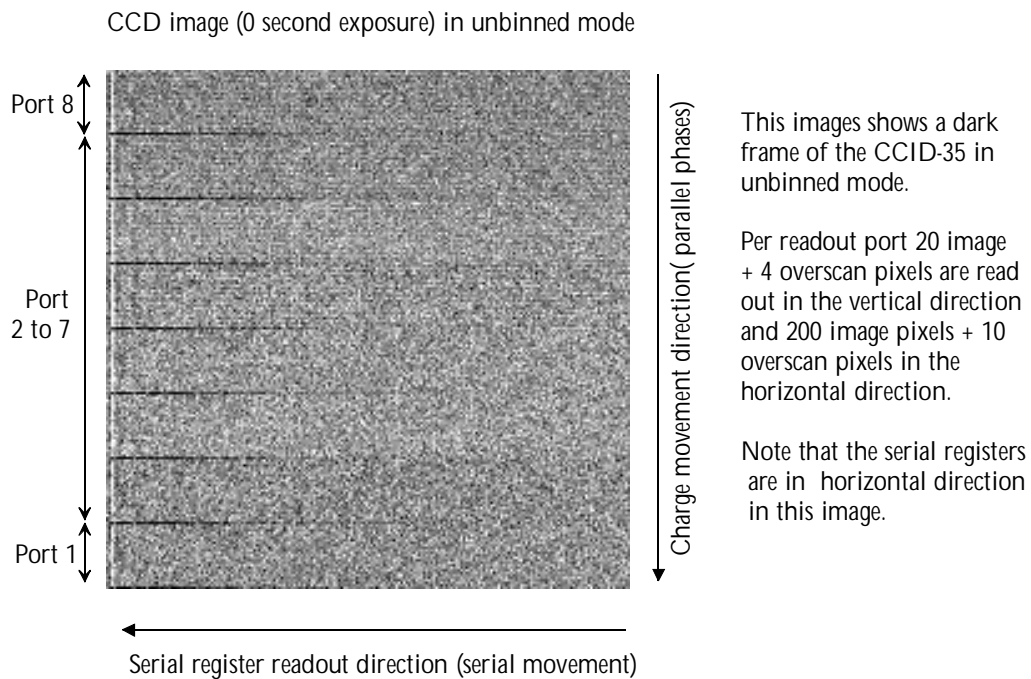
Figure 5-21 CCD mode –dark image.

CCD image in unbinned mode showing the 60 fiber spots
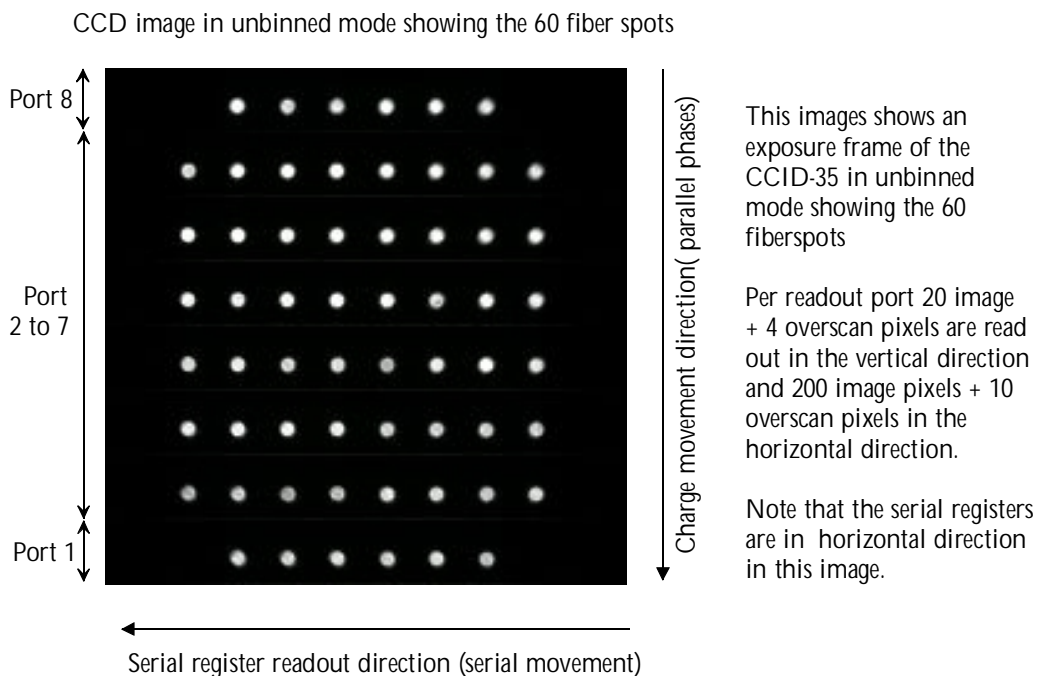
Figure 5-22 CCD mode –spot image.

CCD image in unbinned mode showing photons
stored in the storage pixels SA and SB

extrafocal photons

intrafocal photons

Location of the spot

Charge movement direction(parallel phases)

This images shows an CCID-35 image with charge collected during extrafocal and intrafocal periods of 10 cycles and stored in storage pixels SA and SB

Note that this requires charge movement up and down in vertical direction.

Note that the serial registers are in horizontal direction in this image.

Serial register readout direction (serial movement)

Figure 5-23 CCD mode – storage image.

CCD image in 20x20 binned mode showing photons
stored in the storage pixels SA and SB

extrafocal photons

intrafocal photons

Charge movement direction(parallel phases)

This images shows an CCID-35 image in curvature mode (20 x 20 binning). Charge is collected during extrafocal and intrafocal periods of 10 cycles and stored in storage pixels SA and SB and then read out.

Each superpixel reflects one subaperture in this mode. However, for better visualisation parallels are overscanned by two superpixels.

Note that this requires charge movement up and down in vertical direction.

Serial register readout direction (serial movement)

Figure 5-24 CCD mode –curvature mode image.

5.8.4 Tip/Tilt sensing

The curvature CCD device features a tracker chip to be used as a tip/tilt sensor. The tracker chip simply integrates charge and reads it out. Hence there was no need for storage areas SA, SB and SC. The tip/tilt sensor only has clocks IA1, IA2 and IA3 and XG. The tracker is a bit wider (24 pixels) since we expect to get at least 50 photoelectrons into each "cell" of the tracker chip; the extra rows provide tolerance for alignment and the use of larger fibers. Since we only need 4 subapertures in the tracker, it has a reduced length of 160 pixels.

The tip/tilt sensor is clocked completely independent of the curvature WFS CCD portion of the device. We can integrate and read out this tip/tilt array at a different rate, although for noise reasons one might synchronize the clocks of both arrays.

C h a p t e r   6

LABORATORY SYSTEM DESIGN AND PRACTICAL IMPLEMENTATION

To test the performance and the functionality of the curvature CCD, a laboratory system has been built to allow independent testing without the need to interface to a full adaptive optics system. This chapter gives an overview of the functionality of the laboratory detector system. The FIERA CCD controller [Beletic et al., 1998], developed by the Optical Detector Team at ESO is operating the device. FIERA is capable of reading CCDs fast (up to 2 MHz per port) with readout noise limited by the CCD. FIERA has successfully demonstrated in the past to be able to run 16 ports in parallel at low noise [Feutrier and Dorn, 2000]. Nevertheless, any other CCD controller that is able to run at the desired readout speed will be suitable for operating the curvature wavefront sensor CCD. Figure 6-1 shows a schematic diagram of the main components of the system including the FIERA CCD controller. The system can be split into several subsystems as there are:

6.1 Laboratory system design

o   An integrating sphere and a stable light source. The light source is used to simulate the membrane movement and providing the light signal for CCD characterization.
o   An Oeffner relay optics design (consisting of two spherical, reflecting surfaces to re-image the light of the fibers 1:1 onto the superpixels) and a fiberfeed with 60 individual fibers plus 4 additional fibers for the tip/tilt sensor to feed the subapertures of the CCD with light.
o   A cryostat head, which holds the CCD, the detector fanout circuit and the CCD temperature control and monitoring circuitry.
o   A continuous flow cryostat, which is a vacuum isolated reservoir of liquid nitrogen for cooling the CCD to 150 - 200 degree Kelvin.
o   A cryostat controller to control the flow of liquid nitrogen through the continuous flow cryostat, the temperature of the nitrogen exhaust gas and the temperature of the sorption pumps. The cryostat controller is monitored via a serial interface (RS485 or RS232).

67

Detector system - schematic overview
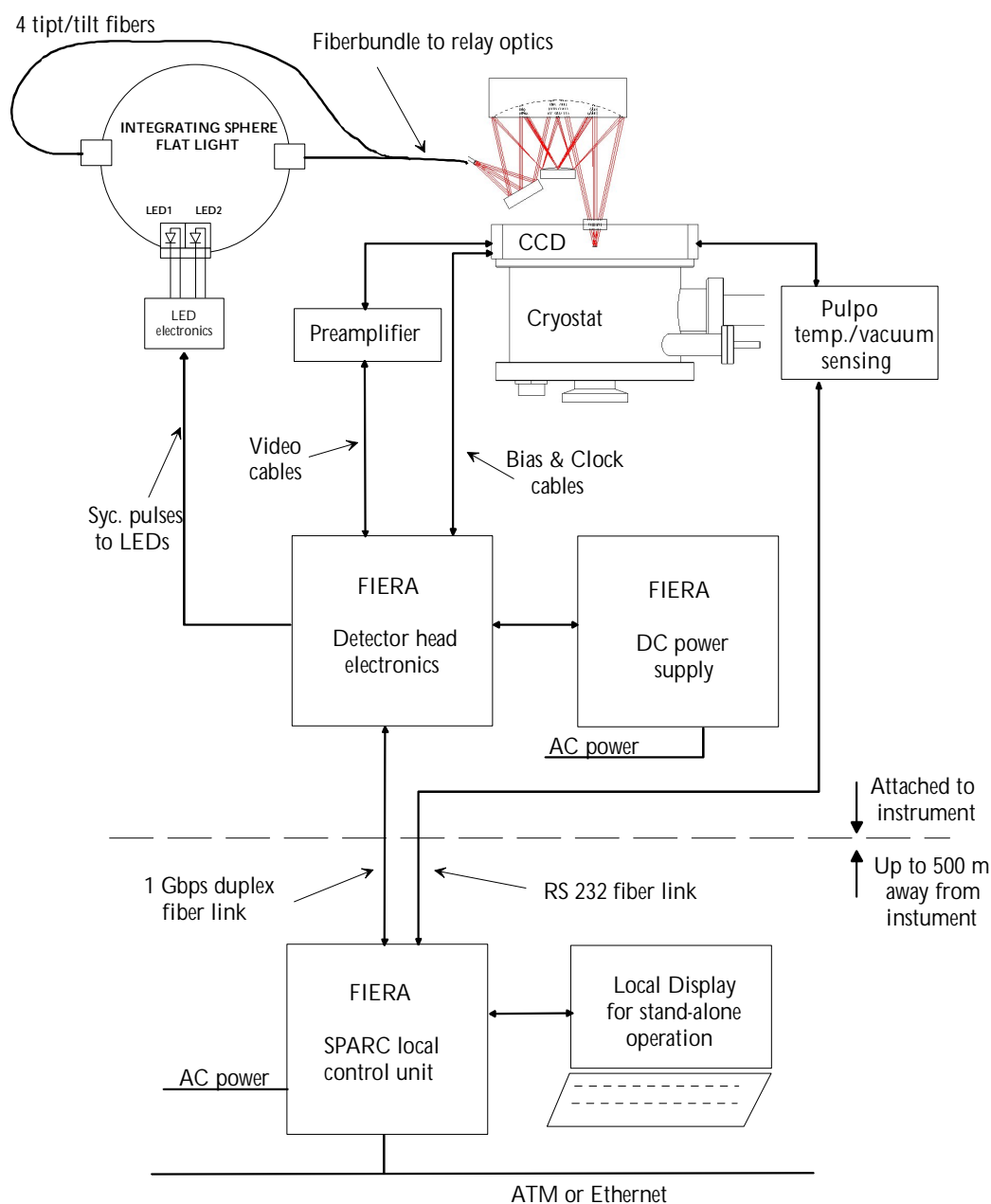
Figure 6-1 Schematic overview of the Detector system.

o   PULPO, a micro-controller based "house-keeping" unit that controls the CCD temperature and monitors the cryostat's vacuum. PULPO is connected to the SLCU via a RS232 fiber link.

o   Preamplifiers for the nine CCD output signals. Four amplifiers are located in one preamplifier box. The preamplifiers are located close to the cryostat head's video connectors (max. cable length of the video input cable is 5 cm).

o   Detector head electronics: The detector head electronics provides clock and bias voltages to the CCD and performs the video signal preprocessing, digitization and data transmission to the SLCU-rack.

o   DC power supply: Provides DC-power to the detector head electronics.   All power supplies are linear for low-noise operation.

o   Sparc Local Control Unit (SLCU):   The SLCU initiates and controls the CCD operation, i.e. wiping, integration and readout. A Sparc-CPU in the SLCU rack performs the higher-level coordination of these operations, whereas a DSP board functions as a real-time controller. The DSP board is directly connected to the detector head electronics via a fiber link. Apart from the CCD control function, the Sparc communicates directly to PULPO for temperature control of the cryostat head and monitoring of the cryostat's vacuum.   For stand-alone operation in the laboratory a display and keyboard is attached.

Figure 6-2 shows a picture of the laboratory prototype system for the CCD-based curvature wavefront sensor and explains the components.

Picture of the Laboratory detector system
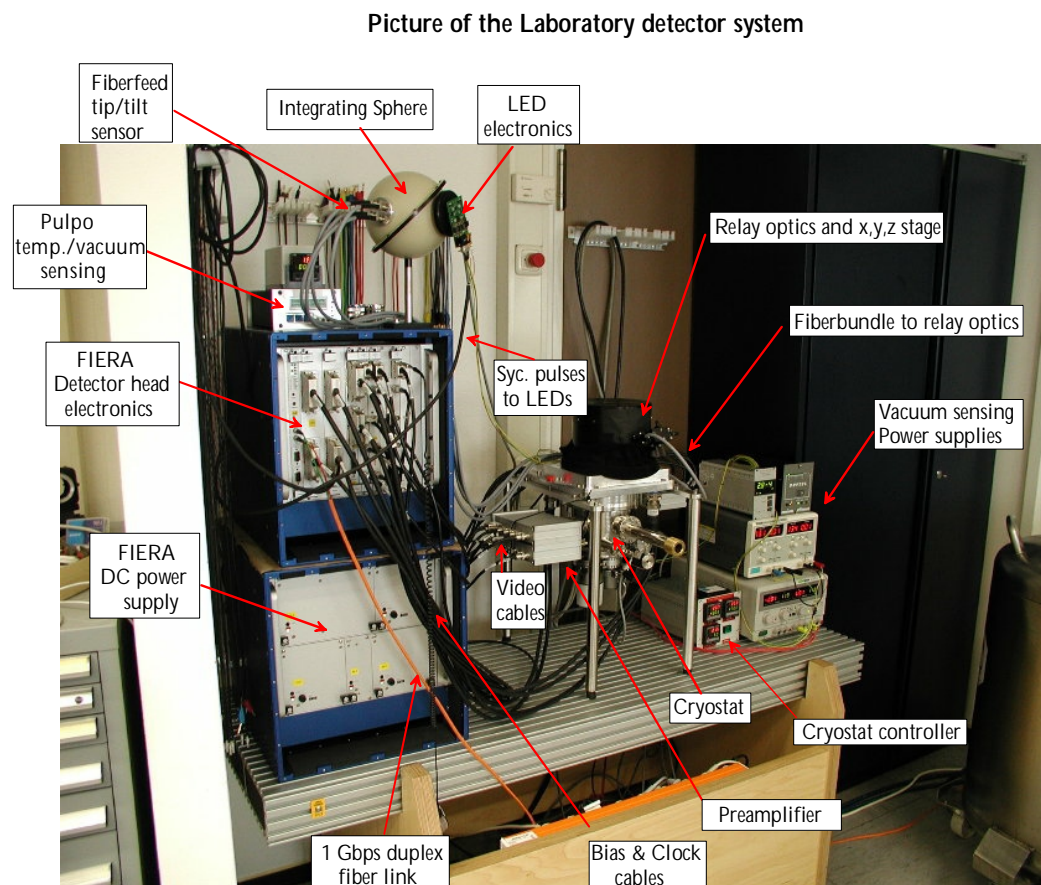
Figure 6-2   Picture of the prototype laboratory system of the CCD based curvature wavefront sensor.

6.2 FIERA CCD controller architecture

The architecture of the FIERA CCD controllers can be described to consist of four major parts in general. For more information on FIERA the reader is referred to the following articles [Beletic et al., 1996 and 1998]. The four parts are:

o A sequencer that generates all necessary signals for the switching of clock lines as well as control signals for the analog preprocessing of the video signal. It usually also includes a slow-speed command interface to a higher-level computer. This interface is used for controller initialization, telemetry (checking of voltages which are applied to the CCD), mode control, etc. Implementations of the sequencer with digital signal processors (DSP), transputers, or gate arrays are common. The sequencer is usually implemented in a single processor.

o A clock driver module, which employs the sequencer's output signals to switch the CCDs clock voltages between lower and upper rail voltages. In this part also the generation of analog bias voltages for the detector are grouped. These DC voltages are mainly used to supply the CCDs output amplifier.

o A video module that contains the analog preprocessing of the CCDs video signal and A/D-conversion. A fiber interface is used in many systems to transmit the data galvanically isolated over a high speed path to the higher level computer. The analog preprocessing of the CCDs video signal is of high importance for low noise operation and will be explain in more detail later on.

o The CCD preamplifiers. FIERA employs a separate preamplifier box, which boosts the CCDs single-ended video signals and converts them into a differential signal pair. The preamp is connected to the CCD head video connector with a cable of less than 5 cm length. The amplified and differential videosignal is output to the detector head electronic box using twinax cables with a maximum length of 2 m. One preamplifier printed circuit board provides four video channels with each one independently controllable gain switch. Each gain switch can be adjusted to any of four settings. The gains are remotely controlled by software via an I²C-bus from the video board in the detector head electronics. Figure 6-3 shows a picture of such a preamplifier box used for the curvature sensor.
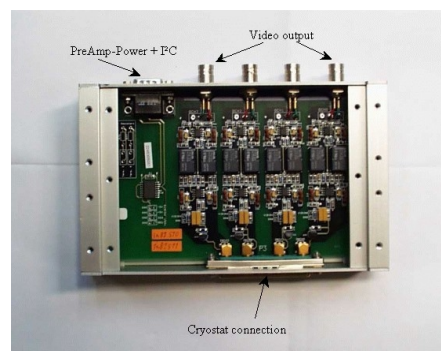
Figure 6-3 CCD preamplifier with 4 channels.

6.3 Fiberfeed concept and relay optics design

<u>Fiberfeed concept</u>

To transmit the light of each single subaperture of the lenslet array, or, for the laboratory system from the integrating sphere, a 100 micron core multi-mode fiber is used as done for APDs. This fiber has a numerical aperture (NA) of 0.22 +/- 0.02, allowing us to input light with f-numbers of 2.27 or slower. This fiber works in the range of 450 nm to 1000 nm with almost 100% efficiency at lengths up to 10 m. These fibers have been fully characterised [Avilia, 1999] and Figure 6-4 shows the total transmission efficiency of this fiber as a function of wavelength. Furthermore a 200 micron fiber was measured. This fiber would give a field of view twice the size of the 100 micron fiber in the curvature AO-system. However we decided to use a 100 micron fiber for the prototype system to loosen alignment tolerance to make sure all fiber spots are well contained in the light sensitive area of the CCD subapertures.
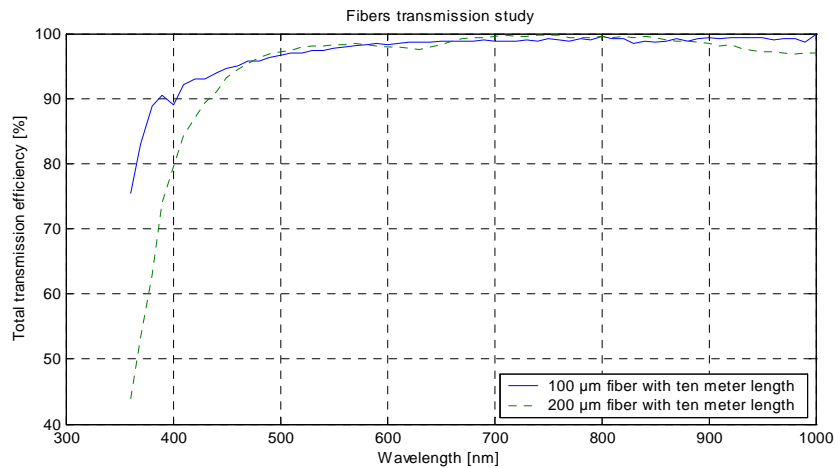
Figure 6-4   Total transmission efficiency of the fibers used for the curvature sensor as a function of wavelength.

The 100 micron fiber is comparable to a 3 arcsec field of view in the VLT curvature AO system design. A fiberfeed of 5 m length has been built to image the light of the individual subapertures of the lenslet array onto the CCD. This fiberfeed consists of 60 individual fibers glued into a support structure. The fiber ends are positioned in the focus spots of the individual lenses. This structure was used to attach the fibers to the integrating sphere or a possible lenslet array. On the other side of the fiberfeed a plate was designed and the fibers were glued into precision-drilled holes forming a grid structure that matches the geometry of the CCD superpixels. This plate has a thickness of 100 μm. Figure 6-5 shows this part. To avoid any crosstalk between the fibers and light intrusion from the outside, the fibers were put into a light tight sleeve. To adjust the fibers an x, y, z table with a fine adjustment precision ≤ 2 μm was attached to the input of the relay optics. This table is able to compensate any x and y tilts for the CCD inside the dewar and it is used to focus the spots onto the light sensitive CCD surface.

Figure 6-5 Support structure of the fibers at the input of the relay optics. The geometry of the precision-drilled hole matches the geometry of the subapertures on the curvature CCD.

Relay optics design

An Oeffner relay design consisting of two spherical, reflecting surfaces is used to re-image the light of the fibers 1:1 onto the superpixels as shown in Figure 6-6. We decided to use a relay optics for the prototype system to simplify the design testing. In parallel we were investigating mating the fiber directly to the CCD. The designed optics has a maximum blur of 60 microns (100% encircled energy) over the entire field size of 3.6 x 4.8 mm, the light sensitive area of the CCD.
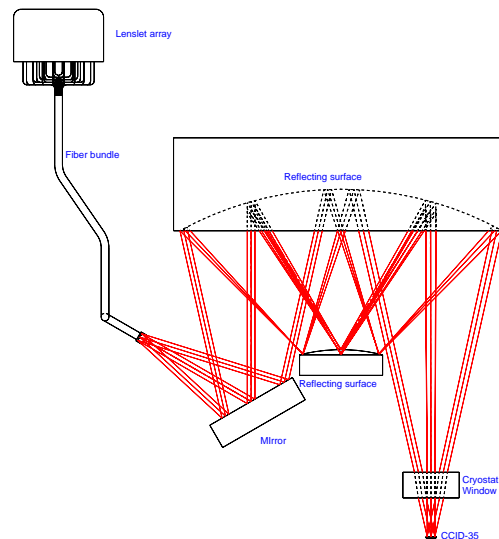
Figure 6-6 Relay optics to be used to reimage the light of the individual fibers onto the CCD.
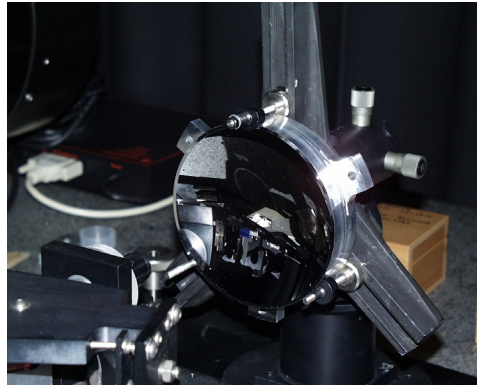
Figure 6-7 Convex sphere of the Oeffner relay optics during the alignment tests in the laboratory.

Figure 6-7 shows the convex mirror of the relay optics during alignment and performance tests in the laboratory. The dimension of the spot sizes on the curvature sensor was of great importance since the storage areas of the CCD did not contain a light shield. For the first wafer run we decided not to put a light shield for the CCD because the CCDs were manufactured on a wafer with many other different CCDs and we desided not to take a risk in the yield for this wafer run. Hence it was important that the optics produces spots not greater than the dimension of the subapertures (360 x 360 μm).
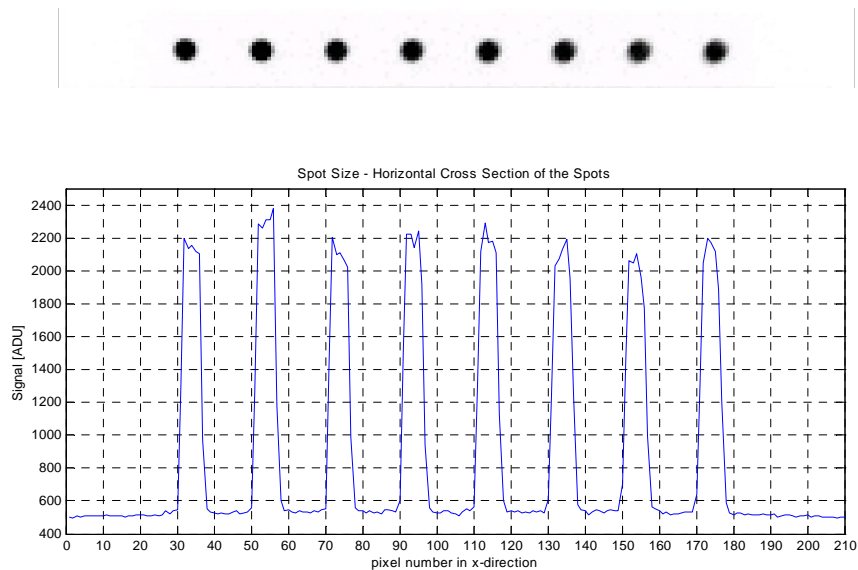
Figure 6-8 Spot image of the curvature CCD (20 x 210 pixels stripe; note that the image is inverted for better visualization) and a horizontal cross section.

Figure 6-8 shows a spot image of the curvature CCD (20 x 210 pixels stripe; note that the image is inverted for better visualization) and a horizontal cross section. The spots on the CCD are 8 to 9 pixels wide (around 144 to 160 μm in diameter) with the 100 μm fibers at the input of the relay optics.

This result matches very good with the calculated spot diameter and allows us also to use a 200 µm fiber to double the field of view.

The mirrors are made out of aluminum and diamond turned to the shape required. However, during the CCD testing it was found that the mirrors produce stray light almost entirely over the light sensitive area of the CCD. It was measured to be at the 1% level. The cause of the problem was found to be due to diamond turning of the mirrors, which produced an almost invisible structure. Mirrors made out of glass would avoid the stray light problem but are more expensive compared to diamond turned aluminum mirrors.

CCD surface

Another opto-mechanical interest for the curvature CCD was the peak to valley flatness of the sensitive surface of the chip. This was important information to align the Oeffner relay optics on top of the cryostat. This applies to optical field size only and was measured using a triangulation sensor [Stroebele, 2000].

We have measured under cooled down conditions the flatness of the CCDs and the flatness with respect to the window backside of the cryostat window. Figure 6-9 shows the topography of the CCD with respect to the window backside. The chip itself has a flatness of 8 µm peak to valley and 2 µm RMS. The distance of the CCD surface to the window backside was measured to be 15.06 +/- 0.02 mm at - 100° C.
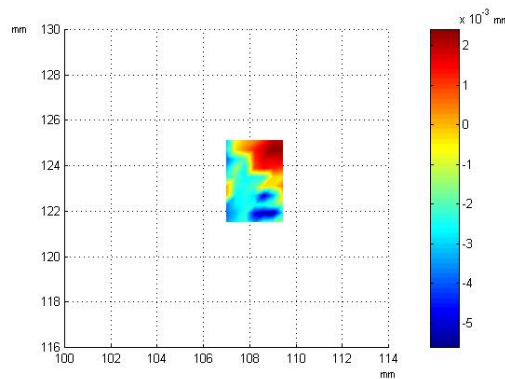
$$RMS = 2 \mu m$$
$$PV = 8 \mu m$$

Figure 6-9 CCD surface analysis.

6.4 CCD Cryostat and cooling of the curvature CCD

To cool the curvature CCD a special detector head was designed and attached to a standard continuous flow cryostat developed by ESO. This cryostat is based on a continuous circulation of coolant supplied from a delocalised reserve of liquid nitrogen [Dorn, 1996 and Lizon, 1997].

This system uses a large tank of liquid nitrogen so that cooling is provided automatically for a relative long period between replacements of the liquid nitrogen reservoir. Another advantage of the continuous-flow cryostat is that it only occupies a small volume at the instrument. Figure 6-10 shows the compactness of the continuous-flow cryostat relatively to the detector-head.
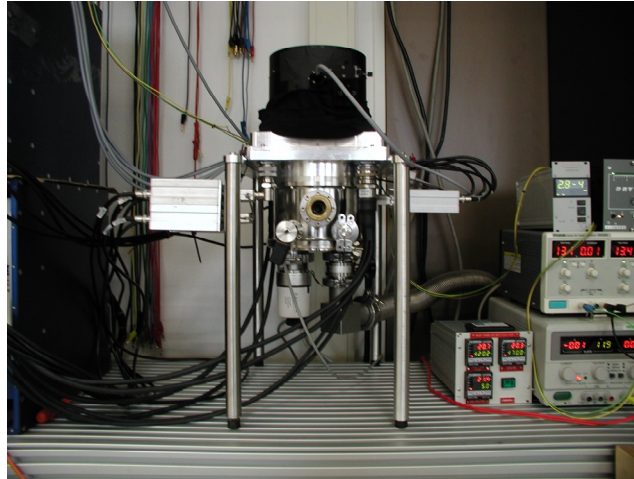
Figure 6-10 CCD cryostat with relay optics.

To monitor the CCD temperature and the vacuum inside the cryostat, PULPO is used. PULPO [Haddad and Sinclaire, 1997] is a versatile micro-controller based unit for housekeeping purposes. It provides CCD temperature monitoring and control. Up to seven PT100 temperature sensors can be monitored by PULPO. An output with a maximum current of 1 ampere can be used to control the temperature, e.g. that of the CCD. Vacuum monitoring is possible with a 0-10 V output voltage from a vacuum gauge. A user interface is based on a LCD-panel and a small keypad. A serial interface is provided for connection to the SLCU.

A simple protocol is used to read monitored sensor outputs and sets the desired values. Shutter control for a variety of different shutter types is also provided but was not used for the curvature system.

6.5 Cryostat electronics design

The CCD is mounted in a CCD head, which provides the mounting of the CCD and the attachment to the cold finger of the CFC cryostat. To operate the CCD a special multi-layer, flex-rigid printed circuit board (PCB) has been designed. On this PCB the passive filters for the CCD clock phases and the capacitors for filtering the bias voltages have been implemented. Furthermore a zero inforce socket is used which then connects to the interPCB. The video outputs run over shielded cables to the CCD head vacuum connectors. Figure 6-11 shows the PCB for the CCD.

This printed circuit board is of high importance for low noise operation of the CCDs. There are no active components on the PCB and no intermediate connectors. The bias, clock and videolines are brought out separately to the vacuum feedtrough connectors with minimal cable length. The PCB has a 6 layer design with ground and shielding layers to avoid crosstalk between the individual signal lines. Also for low noise operation it is

important to put the filters for the CCD bias and clock lines very close to the CCD package.

To filter the bias lines, 100 µF capacitors wired parallel to 100 nF capacitors were used and to filter the waveforms for the clocklines an RC low pass filter of 47 Ohms and 100 pF was implemented. The adjustment and optimization of the filters was of great importance to minimize spurious charge generation and is discussed in more detail in chapter 7.
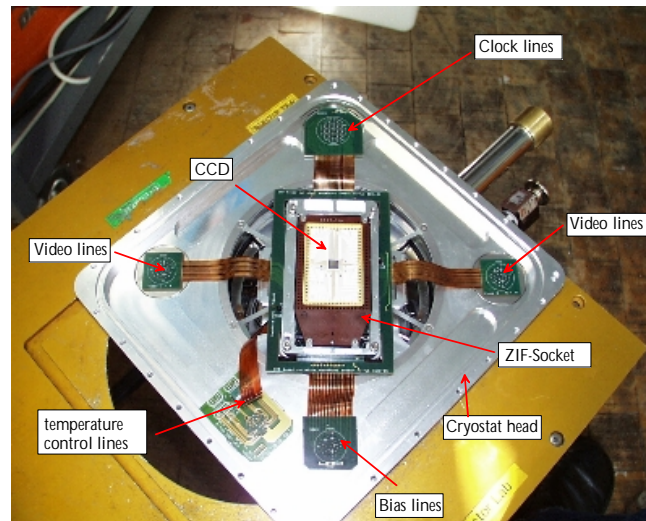
Figure 6-11 CCD cryostat electronics for the CCID-35.

6.6 Stable light sources

To characterize the CCD and to simulate the membrane movement of the curvature AO system a fast electronically switchable source whose brightness is constant down to very short exposure times was needed. Linearity measurements can be made by simply taking a series of exposures of varying duration. This light source is based on a design from Simon Tulloch described in the RGO technical note 111 [Tulloch, 1997].

This light source design was found to be suitable for low level measurements, such as those required for the curvature CCD. It switches on and off rapidly. For exposures of 1 ms or greater its linearity (total light output versus switch-on duration) is greater than 1%. For exposures of 5 ms or longer, the linearity exceeds 0.25%. The stable light source is based on a special LED device manufactured by IPL. This package contains a green LED, a monitor photodiode and a transconductance amplifier and is shown in Figure 6-12.

The output of the amplifier in the LED package is proportional to the LEDs optical output and its bandwidth is 100 kHz. An additional circuitry uses this monitor amplifier to close a feedback loop that ensures the LED has a constant brightness and thus reducing temperature sensitivity and self-heating effects.
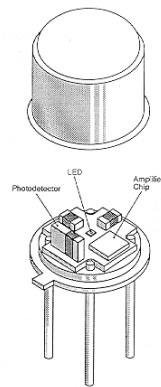
Figure 6-12 Diagram from the data sheet of the special LED IPL 10530 GAL, manufactured by Integrated Photomatrix Ltd (Output: 565 nm peak, 60 nm FWHM).

Additional to the LED an operational amplifier and a stable voltage reference were needed. The operational amplifier LM611 provided those. Two other ICs provided supply rail regulation. The circuit diagram is shown in Figure 6-13. The 3.3 MOhm resistor shown on the left of this diagram was needed to ensure that the lamp was switched off fully when the enable signal was absent. A small offset on the transconductance amplifier in the IPL 10530GAL device would otherwise prevent this happening.
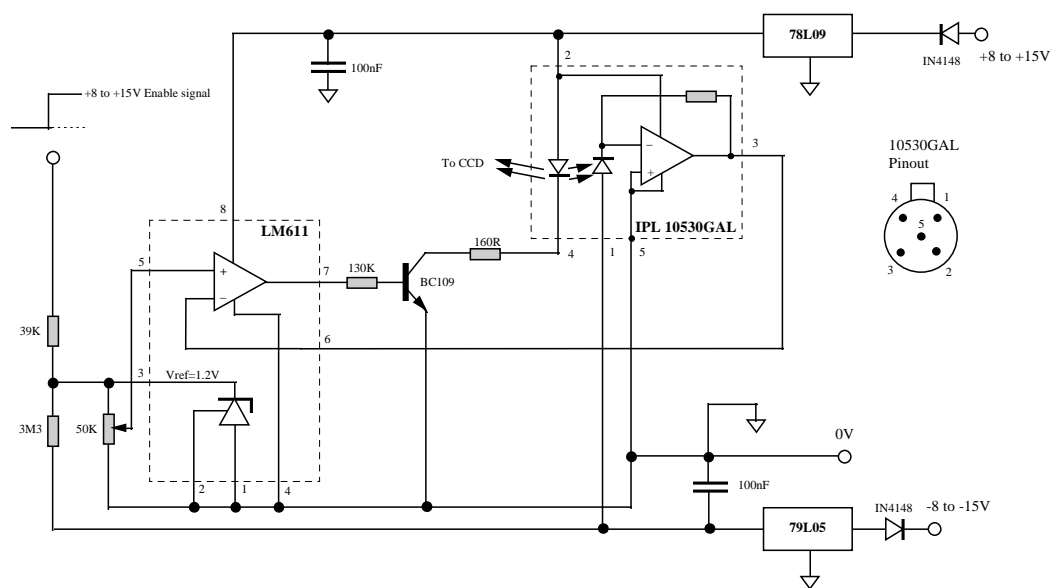
Figure 6-13 Lamp circuitry of the stable LED light source (courtesy Simon Tulloch, 1997).

A high bandwidth of the servo circuitry ensured that the LED output stabilized within about 25 μs after the enable signal went high. The LED switched off even quicker. Figure 6-14 shows the relevant waveforms, obtained at pin 3 of the 10530 GAL device [Tulloch, 1997].
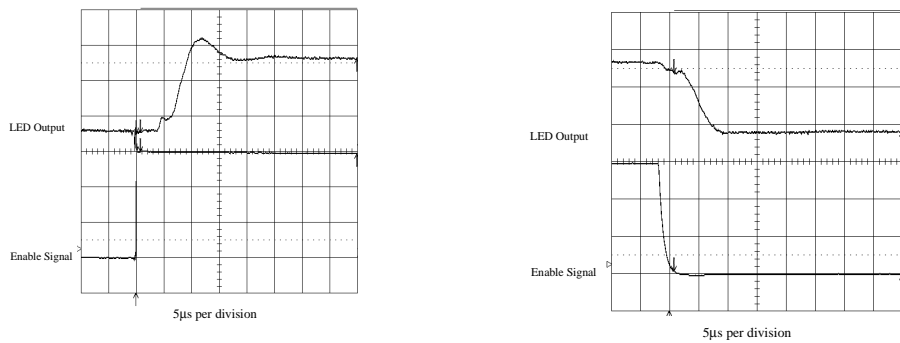
Figure 6-14 Switch-on delay and Switch-off delay of the LED.

6.7 Simulation setup for the curvature sensor

To be able to test the functionality of the curvature CCD without interfacing the CCD based curvature wavefront sensor to a complete adaptive optics system and to simplify the test procedures in the laboratory, a simulation setup has been built. The principle is shown in Figure 6-15 and Figure 6-16 shows a picture of this part in the laboratory system.

An integrating sphere was used to feed the fiber inputs with flat light given by two independent controllable stable LED sources. The LEDs were triggered with clockpulses from the CCD controller and hence it was possible to simulate the extrafocal and intrafocal times of a membrane as used in a full curvature system.

On one output of the sphere the 60 fibers for the curvature array were interfaced and on another output of the sphere the four individual fibers for the tip/tilt sensor were attached. On the last opening the two stable LEDs and the associated drive and stabilization electronics was attached.

With this setup it is possible to switch on and off the light of the LEDs, feeding the subapertures and to perform various tests. For example it was possible to turn on one LED during the complete time of a duty cycle integration of the CCD and to pulse the other LED during this time as in the example shown in Figure 6-15. This gives twice the amount of photons during either the exrafocal or intrafocal integration time. By putting the integrating sphere directly in front of the CCD window, it was possible to send flat light to the CCD for measurements such as charge transfer efficiency and the cosmetic quality of the curvature CCD.

TESTSETUP TO SIMULATE THE MEMBRANE MOVEMENT
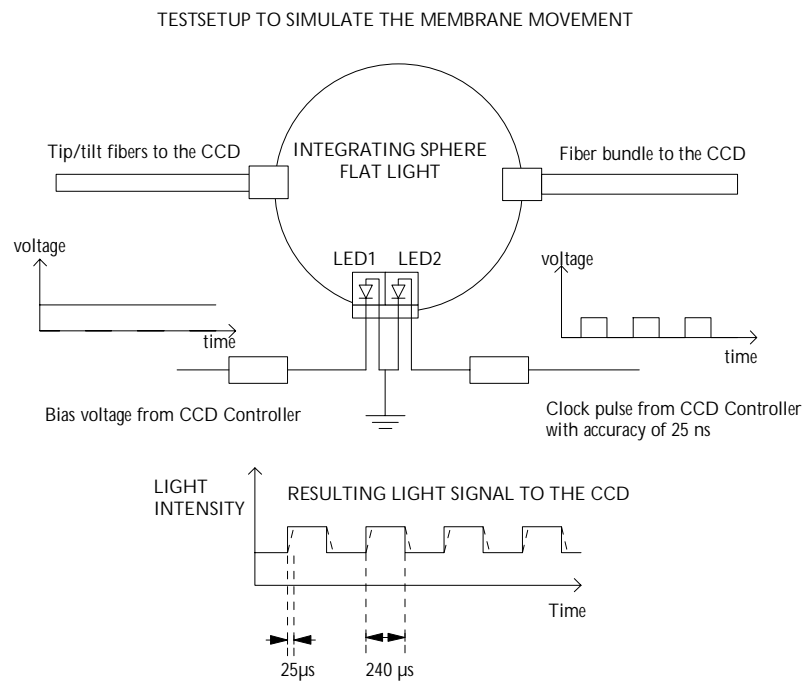
Figure 6-15 Schematic diagram of the simulation setup with the integrating sphere and the stable LEDs.
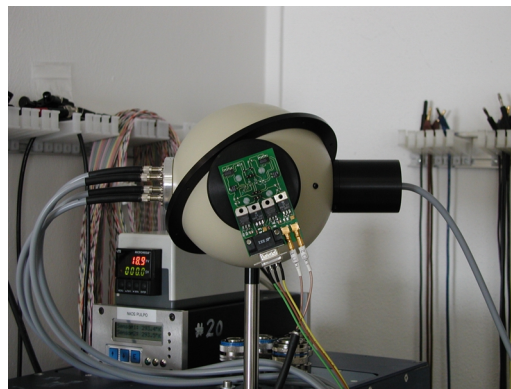
Figure 6-16 Picture of the simulation setup for the curvature sensor.

Chapter 7

CCD CHARACTERIZATION AND PERFORMANCE

The chapter is organized in several subsections, which explain the methods used to optimize and characterize the CCD performance and present the results obtained. Extensive test have been performed to evaluate the performance of the frontside CCD. The CCDs were optimized for low readout noise, essential for the application. A readout noise of less than 1.5 electrons at 4000 frames per second has been demonstrated. The last section presents the results of another simulation run with the obtain performance of the optimized CCDs with respect to avalanche photodiodes.

One of the most important CCD performance measures is the Photon Transfer Curve (PTC), which allows quantifying many CCD parameters. Furthermore it is used to calibrate and optimize the performance of the curvature CCD.

7.1 System performance - The Photon Transfer Curve

A fundamental technique to measure the performance of a CCD system is the Photon Transfer Curve [Janesick, 1987 and 2000]. This technique allows to measure and judge the performance of a detector system without knowing its inner setup. A proper transfer curve indicates, that the complete chain of the signals in the detector system like the drive voltages, the signal processing, the clocking and interfaces are in good order.

Measurement of CCD parameters such as noise, system gain, full well capacity, quantum efficiency, dark current, sensitivity and linearity are covered using the photon transfer curve. A photon transfer curve has three different noise regimes, as there are readnoise, shot noise and fixed pattern noise (shown in Figure 7-1).

Read noise is the noise associated with the CCD output amplifier and the readout electronics (i.e. its signal processing, digitization etc.). This is the intrinsic system noise of a dark frame or image (no light). It is independent of the photons or input signal. The slope is 0 on a logarithmic scale.

Shot noise occurs when the input signal increases and the noise of the CCD is dominated by shot noise. Shot noise is proportional to the square root of that signal. The slope is 0.5 on a logarithmic scale.

Fixed Pattern noise arises at high levels of illumination. This noise results from differences in sensitivity of pixels. This is also called the Pixel Response Nonuniformity (PRNU). Due to processing and mask alignment variations during manufacture each pixel has a slightly different charge collection capacity and responsivity. This noise is proportional to the number of photons. The slope is 1 on a logarithmic scale.
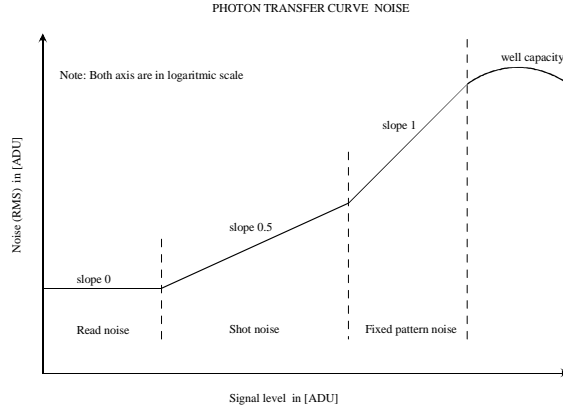
Figure 7-1 Photon transfer curve: The plot describes three noise regimes of the CCD detector system, 1) read noise 2) shot noise and 3) fixed pattern noise.

The photon transfer curve plots readnoise as a function of the signal for an area of n by n pixels in a CCD frame. To obtain the x-axis of the curve one computes the mean, dark subtracted signal S. That is

$$S = \frac{\sum_{i=0}^{i=N_p} S_i - S_{dark}}{Np} \, , \qquad (7\text{-}1)$$

where S_i is the signal value of the ith pixel and N_p is the number of pixels in the n by n pixel area. S_{dark} is the signal of a dark frame taken from the same data set. To obtain the y-axis of the curve, the variance σ^2 is computed. The variance is the square of the standard deviation of a single observation from the mean of the pixels.

$$\sigma^2 = \frac{\sum_{i=1}^{i=N_p} (S_i - S)^2}{Np} \, . \qquad (7\text{-}2)$$

For practical implementation two dark frames (*d1* and *d2*) and 2 equally exposed frames (*f1* and *f2*) where taken and the "true" signal frame on a frame basis and the variance on a pixel by pixel basis is calculated. That is

$$S(ADU) = \frac{(f1 - d1) + (f2 - d2)}{2} \, , \qquad (7\text{-}3)$$

and for the variance,

$$\sigma^2(ADU) = \frac{(f1 - S)^2 + (f2 - S)^2}{2} \, . \qquad (7\text{-}4)$$

The subtraction of the mean from the signal frame has the effect of removing the signal itself, as well as any DC offset or bias caused by amplifier drift occurring between the two exposures. Subtracting the differenced pixels from each other, again on a pixel-by-pixel basis, then removes any fixed pattern noise inherent in the CCD structure. What remains is the time varying random noise and the variance represents the random noise power of the detector system in analog to digital units (ADU).

Standard deviation σ is defined as the square root of the variance and is the rms noise of the system. Variance and standard deviation are expressed in ADU, not electrons, since they both inherently contain the system gain. Therefore the system gain is expressed in electrons/ADU. Finally the mean value of the pixels can be calculated, where n is the number of pixels in the subarea. This is the value for the x-axis of the photon transfer curve. The mean value of the variance can be calculated giving the value for the y-axis of the photon transfer curve.

$$S_{mean}(ADU) = \frac{1}{n}\sum_{i=1}^{i=n} S_i ,$$ (7-5)

and

$$\sigma^2{}_{mean}(ADU) = \frac{1}{n}\sum_{i=1}^{i=n} \sigma_i{}^2 .$$ (7-6)

Since the fixed pattern noise is removed with this method, the two noise sources left are photon noise and readout noise. Those noise sources add together quadrature since they are random and independent. The total noise is calculated as

$$\sigma^2_{total} = \sigma^2_{photon} + \sigma^2_{readnoise} .$$ (7-7)

Assuming poisson statistics, σ^2_{photon} is the signal in electrons and is equal to the illumination level i_e, the illumination level in electrons. This is the illumination level i_{ADC} multiplied by the conversion factor c in electrons/ADU. Hence σ_{ADU} is the standard deviation of the signal in ADU, multiplied by the conversion factor. In equation this can be written as:

$$c^2\sigma^2_{ADU} = ci_{ADU} + \sigma_{readnoise} .$$ (7-8)

Plotting the noise squared (in y) and the signal (in x) on a linear plot as the illumination is increased, gives a straight line of gradient $1/c$, where c is the conversion factor in electrons/ADU. The conversion factor is then used to convert the noise from ADUs to the noise in electrons.

Logarithmic graphs like the one shown in Figure 7-1, are commonly published in literature and are very similar to photon transfer curves on a linear plot. The dissimilarity is simply that fixed pattern noise is eliminated through frame subtraction and the full-well transition is excluded.

7.1.1 Implementation for the curvature CCD

Since the readnoise of each subaperture needed to be measured, a modified "time series" method has been developed to verify the readnoise in a single superpixel for the curvature mode (20 by 20 pixels binned superpixel). A readout mode was programmed to

transfer only one subaperture per frame. Hence those superpixel of 25,000 frames with equal exposure times were assembled into a 50 x 500 superpixel or "single" subaperture frame.

This method implies very accurate flux over time of the LED source used to illuminate the CCD. Using those frames and the photon transfer method outlined obove, the readout noise for each subaperture was measured.

```
SEQUENCE read_ccd_20x_1
pixel_x = 500
pixel_y = 400
pixel_order = "0 ,1 ,2 ,3 ,4 ,5 ,6 ,7"
{ repeat 50
{ repeat 500
{integrate 1 1;
parallel_shift 20 1;
serial_shift_20x_non_convert 5 1;              5 skipped subaperture
serial_shift_20x 1 1;                          only this subaperature get transferred per readout
serial_shift_20x_non_convert 6 1;              5 skipped subaperture
}}}.
```

Figure 7-2 shows a flat field image of the curvature array obtained with the "single subaperture" readmode.
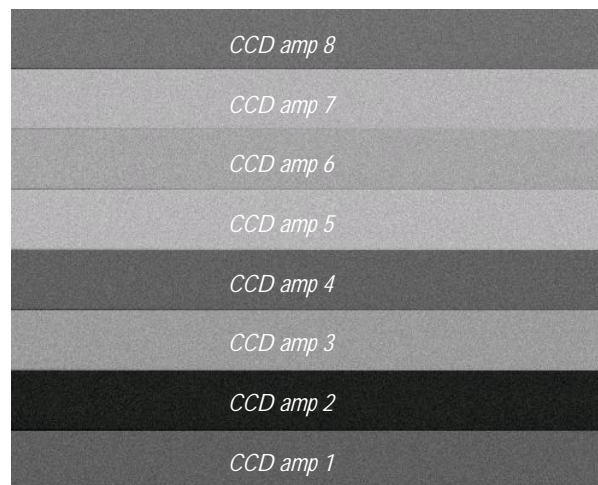
Figure 7-2 Example of a "time series" flat field image used for noise calculations with the curvature CCD.

7.1.2 Noise results

The readnoise for the curvature CCD was measured with the method explained above and Figure 7-3 shows a typical photon transfer curve for the first output amplifier of the CCD. Photon transfer curves for the other amplifiers are shown in Appendix E4. Table 7-1 list the results for all eight output amplifiers, the tip/tilt tracker and the corresponding conversion factors.

A readout noise of less than 1.5 electrons was achieved for all readout ports including the tip/tilt sensor at a readout speed of 4000 frames per second. With all pixels per per readout port binned into 12 superpixels, it was possible to read the serial register relatively slowly at 50 kilopixels per second. Hence it was possible to obtain very low noise results and to maintain the high frame rate with the CCD. Due to the summing well in the CCD design, binning of the pixels did not increase the readnoise.
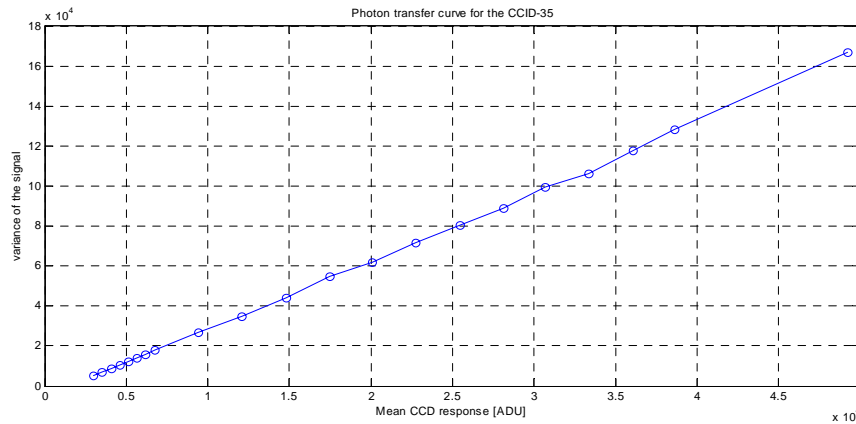
Figure 7-3 Photon transfer curve for the first output amplifier of the CCID-35. The conversion factor is 0.293 electrons/ADU (the inverse of the gradient of the best fit of that line).

CCD output amplifier	Readout noise (electrons)	Conversion factor (electrons/ADU)
1	1.42 ± 0.002	0.295 ± 0.007
2	1.38 ± 0.002	0.293 ± 0.005
3	1.42 ± 0.002	0.294 ± 0.005
4	1.42 ± 0.002	0.297 ± 0.004
5	1.31 ± 0.002	0.294 ± 0.005
6	1.43 ± 0.004	0.290 ± 0.005
7	1.28 ± 0.002	0.292 ± 0.004
8	1.23 ± 0.002	0.288 ± 0.005
Tip/tilt sensor	1.44 ± 0.003	0.299 ± 0.004

Table 7-1 Readout noise results for the CCID-35 with the 20 x 20 binned superpixels in curvature mode.

7.1.3 Optimal bias setting for the output amplifier

The optimal bias voltages for the nine output amplifiers of the CCID-35 were found by varying the drain voltage of the output MOSFET amplifiers. A curve of read noise (in electrons rms) as a function of drain voltages was measured for a certain drain current I_D.

The MOSFET amplifier are loaded with 100 kOhm resistor and the voltage at the source of the amplifiers is approximately one volt lower than the voltage applied to the drains. It was important to maintain a high voltage gain during the optimization process

for good linearity and being in the low noise regime. Therefore also the conversion factor was measured (see Figure 7-4). It was found that if the drain voltage is too low, the conversion factor gets too high and the noise increases. By raising the drain voltage too high, shot noise and 1/f noise are dominating the amplifier. All states in-between these regimes are also called the pitch-off state for the amplifier [Janesick, 2001].

The optimal setting for the CCD drain voltages were found to be around 21 Volts, obtaining the lowest noise levels. This implied a drain current of 20 Volts/100 kOhm to be 200 µA. By raising the drain voltages even higher (above 22 Volts), it is possible to destroy or damage the MOSFET transistors on the CCD. A plot of the measurement for one amplifier is shown in Figure 7-4.
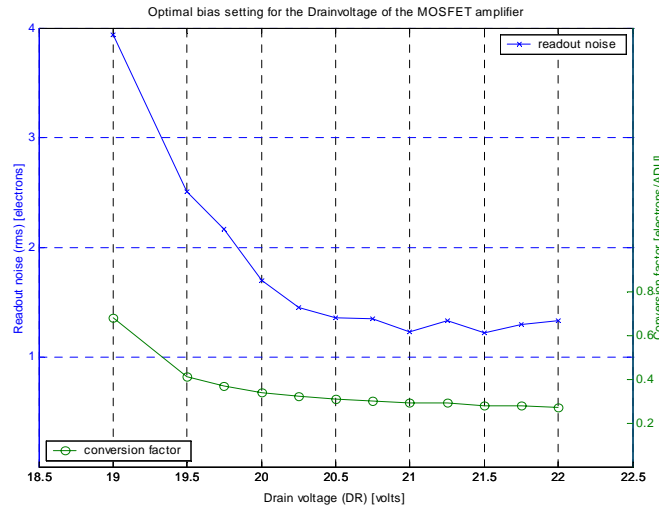
Figure 7-4 Determination of the optimal drain voltages for the MOSFET amplifier of the CCID-35 (I$_D$=200 µA).

7.1.4 Responsivity of the output amplifier

A high responsivity of the output amplifiers is important to obtain low noise with the CCID-35s. It is defined by

$$R = \frac{q}{C_s},$$ (7-9)

where R is the responsivity in µV/electron and C_s is the sense capacitance in Farad. C_s is the sum of the gate capacitance of the MOSFET structure and the capacitance related to the floating diffusion. The smaller the capacitance, the higher the responsivity of the amplifier. The responsivity of the amplifier can be measured using data from photons transfer curves and the characteristics of the analog amplification chain in the CCD controller. The responsivity is given by

$$R = \frac{S_{ADC}}{G} \frac{1}{C},$$ (7-10)

where S_{ADC} is the sensitivity of the analog to digital converter in µV/ADU used in the CCD controller, c is the conversion factor in electrons/ADU and G is the electrical gain in the analog signal chain, which is unitless. Using a 16 bit analog to digital converter with an input voltage range of +/- 5 Volts, the sensitivity of the ADC is calculated to be 10V/65536 ADU= 152.6 µV/ADU.

A schematic diagram of the analog signal chain for the curvature system is shown in the following Figure. With the gain settings in the amplification chain of the system the overall electrical gain can be calculated. For the curvature CCD the signal of the output amplifiers get amplified in the preamp with a gain of 2.25 and are then fed differential into the signal chain of the FIERA videoboard. The signals then get amplified in two steps with a low pass filter (gain 2/3) in between by a factor of two and a factor of twelve and are then fed to the input of the ADC. The overall electrical gain can be calculated by the sum of the different amplification steps and is for the curvature CCD 36.
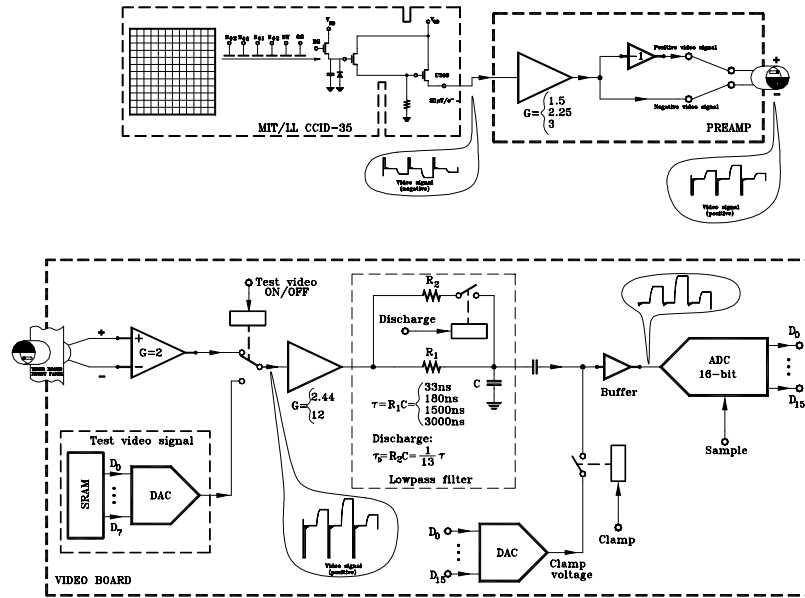
Figure 7-5 FIERA analog signal chain - schematic overview

The filter setting of the low pass filter in the signal chain was of importance for low noise operation and is optimized for the readout speed of the CCD. The RC time constant of the filter is $\tau = RC$. It was found that best noise values were obtained with the filter adjusted to τ =1500 ns, given the signal around 4 to 5 RC time constants time to settle before being sampled by the ADC.

Hence the responsivity of the CCID-35 can be calculated to be (152.6 µV/electron)/(36 x 0.3 electrons/ADU)= 14.2 µV/electron ± 5%. This result matches very closely the estimation given from the CCD design (see chapter 5). However there is an error of ~5% in this calculation due to the tolerance in the electronic parts and resistors in the signal chain.

7.2 Linearity

Charge that is generated by the photoelectric effect, collected in the pixel and transferred to the sense node of the output amplifier should be proportional to the photons that get absorbed be the CCD silicon. However, the conversion of charge to a voltage is not fully linear. Ideally the output amplifier of the CCD limits the linearity, which is usually as good as 0.1%.

Most linearity problems are encountered due to wrong bias voltages applied to the CCD and due to the electronics in the signal chain of the preamplifier and the CCD controller. This off-chip electronics usually limits the linearity to be better than 1% over the dynamic range of the CCD.

Linearity performance was measured using two curves, as there are: (1) The linearity transfer curve and (2) the residual non-linearity transfer curve. A linearity curve is obtained by plotting the input illumination or exposure time versus the CCD response on a linear graph. Since the plot is based on the true illumination levels and the CCD is expected to show a linear response, the result should be a straight line.

To calculate the residual non-linearity (RNL) curve, the best fit from those data points is calculated and its deviation is calculated as following:

$$RNL = \frac{error_{max} - error_{min}}{ADC_{fullscale}} 100 \, , \qquad\qquad (7\text{-}11)$$

where RNL is the integral non-linearity, $error_{max}$ is the maximum most positive error from the best fit straight line, $error_{min}$ is the minimum, most negative error from the best fit straight line and $ADC_{fullscale}$ is the ADC converter full-scale value. Note that the RNL curve presents the worst case peak to peak error of the linearity over the full dynamic range. The ADC converter full-scale value is the highest value of the ADC from the last measurement.

Figure 7-6 shows a linearity curve for CCD output amplifier one and Figure 7-7 the corresponding residual non-linearity plot. Table 7-2 list the results for all 8 ports of the CCD and the tip/tilt sensor in tabular form.

CCD output amplifier	Residual non linearity	Conversion factor (electrons/ADU)
1	+0.416% / -0.318%	0.295 ± 0.007
2	+0.603% / -0.285%	0.293 ± 0.004
3	+0.567% / -0.331%	0.294 ± 0.005
4	+0.491% / -0.393%	0.297 ± 0.004
5	+0.451% / -0.264%	0.294 ± 0.005
6	+0.415% / -0.455%	0.290 ± 0.005
7	+0.518% / -0.462%	0.292 ± 0.004
8	+0.407% / -0.321%	0.288 ± 0.005
Tip/tilt sensor	+0.442% / -0.323%	0.299 ± 0.004

Table 7-2 Residual non-linearity results for the CCID-35 and the corresponding conversion factors.

Plots of the linearity and residual non-linearity transfer curves for the other ports are shown in Appendix E1 and E2.
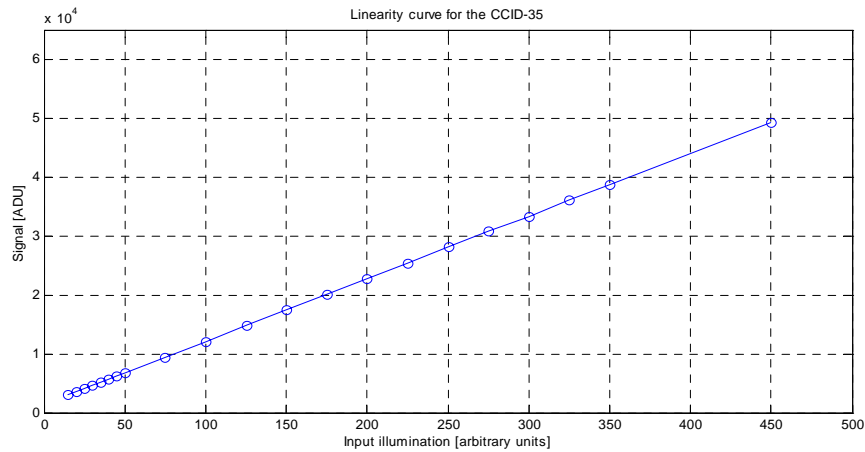
Figure 7-6 Linearity curve for the first output amplifier of the CCID-35 with a gain factor of ~0.3 electrons per ADU. Since the CCD will operate most of the time at low light levels more data points were measured at low illumination levels.
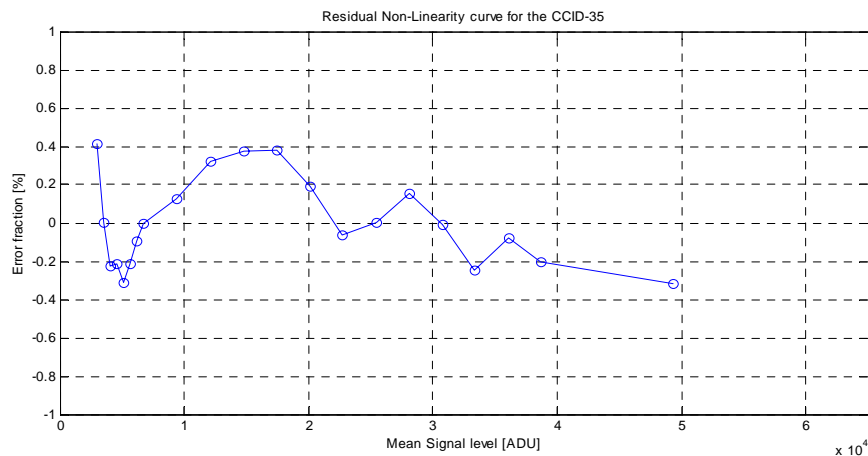
Figure 7-7 Residual non-linearity curve of the first output amplifier of the CCID-35. The non-linearity (peak to peak) is 0.41% / -0.32%.

The non-linearity was found to be better than 1% for all ports and required a significant amount of testing at various voltages for the amplifier to find the best trade of between low noise and good linearity. It is speculated that the CCD amplifier is much more linear than the results show. It is difficult to separate the non-linearity of the output amplifier from the non-linearity caused by the light source or the readout electronics. However a CCD system with a non-linearity of not greater than 1 % is considered to be very good.

7.3 Influence of charge shifting on readnoise and spurious charge generation

<u>The influence of charge shifting</u>

Figure 7-8 shows an image of the CCD adding up charge for 100 cycles in the storage pixels SA and SB and then the CCD was read out. To investigate the influence of charge shifting and the generation of spurious charge, the read noise in the imaging area was measured and showed no difference from a dark frame (4.5 ADU at a conversion factor of 0.3 electrons/ADU, i.e. 1.35 electrons readout noise.).
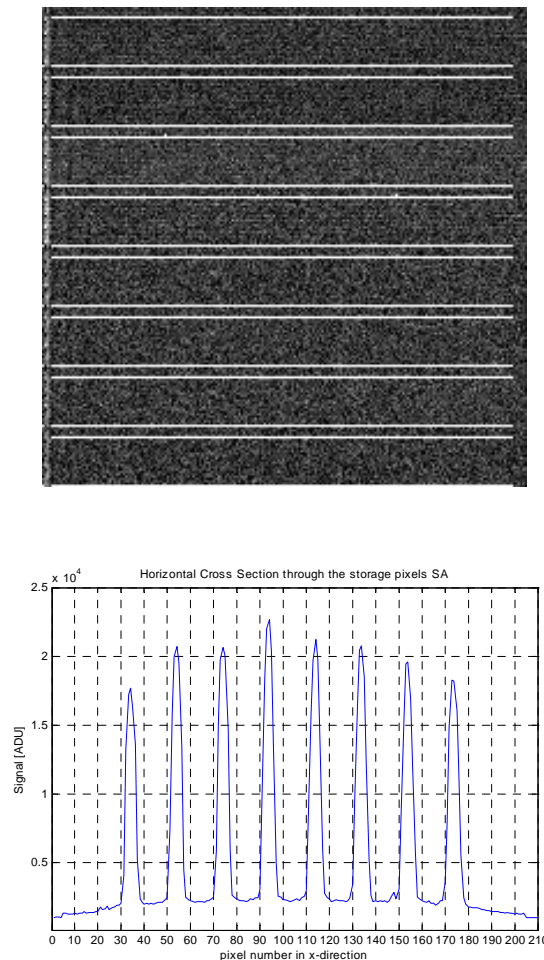
Figure 7-8 Image of the CCID-35 adding up charge for 100 cycles in the storage pixels SA and SB and a horizontal cross section though storage pixels SA, showing the signal level.

Also a cross section though the storage area is shown which indicates the charge summed in the pixels. Due to the cut level in the image the charge in the storage area is only visible as a bright line. This is due to stray light of ~1% caused by the mirrors in the Oeffner relay optics as mentioned in chapter 6.

<u>Spurious charge</u>

Spurious charge is an important source of unwanted charge when CCDs are clocked into inversion. Holes from the channel-stops migrate and collect beneath the gate, pinning the surface to the substrate potential. Some of these holes become trapped at the $Si\text{-}SiO_2$ interface and when the clock is switched to the noninverted state, the holes are accelerated away from the $Si\text{-}SiO_2$ interface. Some holes are released with sufficient energy to create additional electron-hole pairs by colliding with silicon atoms (a process known as impact ionization). These "spurious" electrons are then collected in the nearest potential well [Janesick, 2001].

Spurious charge was first observed when testing the CCD in curvature mode. Usually spurious charge is generated on the leading edge of the clock as a phase comes out of inversion. The falling edge has no influence on spurious charge generation in CCDs. On the other hand, spurious charge increases exponentially with clock rise time and clock swing. Sending holes back to the channel-stops with a fast moving, high amplitude clock increases impact ionisation and spurious charge. Furthermore spurious charge increases with clockwidth and if the clockpulse width is relatively short, holes will remain in the interface states reducing impact ionization. Spurious charge can be mistaken from normal dark current.

The sources can be measured separately because spurious charge is only generated when the device is clocked and its amplitude is not a function of integration time. If dark charge increases with clock amplitude or when driven into inversion then the source is likely to be spurious charge. It is more difficult to detect spurious charge in the horizontal register since it will appear as an offset in each pixel. Measuring the read noise as the clocks are adjusted isolated horizontal spurious charge and the noise level changes as the clock level changes.

The method to reduce spurious charge to negligible levels was waveshaping the clock pulses. Waveshaping reduced the electric fields and returned the holes to the channel-stop regions at a slower rate thereby suppressing spurious charge. Waveshaping was implemented by adding a R-C network in series with the output of each CCD clock driver on the cryostat pcb as shown in Figure 7-9. Allowing a phase to settle 3 RC time constants during the clock overlap period optimized the amount of waveshaping.
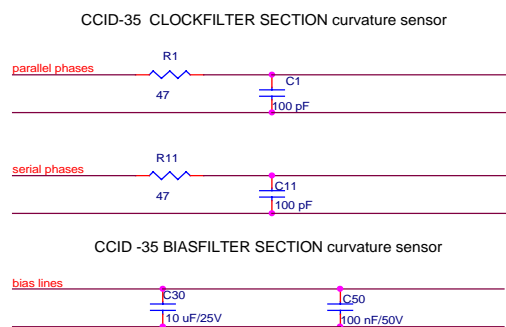
Figure 7-9 Clock and bias filter for the fanout printed circuit board inside the cryostat.

A clear indication that spurious charge generation is eliminated is the low dark current obtained with the CCD. This is explained in more detail in section 7.7.

7.4 Charge transfer efficiency (CTE)

Charge transfer efficiency is highly important for the use of the curvature CCD as a low light level wavefront sensor in adaptive optics. Therefore great emphasis was given to measure charge transfer efficiency (CTE) with the curvature CCD at low light levels. Two methods were used and the results were compared. The first method is the extended pixel edge response (EPER) method and a popular method for CTE measurements [Janesick et al, 1988]. By using a flat field exposure, CTE is estimated by measuring the amount of deferred charge found in the extended pixel of line region in the serial and horizontal direction (see Figure 7-10). Charge transfer efficiency is defined as

$$CTE = 1 - \frac{S_{total}}{S_{lc} n_{transfer}},$$
(7-12)

where S_{total} is the total deferred charge measured in the extended pixel region, S_{lc} is the charge level of the last column and $n_{transfer}$ is the number of pixel transfers in the CCD. It is important to use the last column in the sensitive area of the CCD since charge from flat field images can diffuse from outside the array, giving a higher response. To avoid this a scupper as mentioned in chapter 5 was implemented on the CCD design.

However, it can be seen that the scupper does not capture all the charges, resulting in a bit brighter last column.

Figure 7-10   Principle of charge transfer efficiency measurement with the extended pixel edge response method.

CTE was measured at various light levels and Table 7-3 lists the results. 200 images were averaged together to improve the signal to noise ratio in the overscan region and to reduce the noise. CTE was found to be very similar for all ports. However the charge transfer varied with the amount of charge transferred within the CCD.

Even at very low light levels down to 26 electrons per pixel signal charge, CTE was still measured to be 0.99999 or better. Its needs to be noted, that the extended pixel edge response method is a relative CTE measurement and not an absolute one. Since it

compares the target pixel amplitude to the deferred charge level other factors like the operating temperature or the readout rate will influence the results obtained. Measuring CTE at even lower light levels is more difficult as with good CTE the amount of deferred charge is very small and hence difficult to measure; especially with only 20 transfers in vertical direction and 200 transfers in horizontal direction as for the curvature CCD.

Mean signal in flat exposure in [electrons]	Horizontal CTE	Vertical CTE
2858	>0.9999999	>0.9999999
1397	>0.9999999	>0.9999999
228	0.99999607	0.99999948
90	0.99999848	0.99999879
84	0.99999607	0.99999734
53	0.99999308	0.99999867
26	0.99999878	0.99999568

Table 7-3 Results of charge transfer efficiency in horizontal and vertical direction at various light levels, measured with the EPER method.

Another method to estimate CTE can be made by using the data from pocket pumping images explained further in the next section. This technique locates very small traps as small as one electron [Janesick and Elliott, 1987]. Figure 7-11 shows a pocket pumping image of the CCD. This "trap-map" shows that CTE can be statistical when the trap count is very low. Some columns show more than one trap, leading to the result that CTE can vary from column to column when measured. The average global CTE can be estimated by counting the traps in the trap map and using the following equation [Janesick, 2001]:

$$CTE = 1 - \frac{N_{Trap}}{I_{flat}} \, , \qquad\qquad (7\text{-}13)$$

where N_{Trap} is the average number of traps per pixel and I_{flat} is the number of electrons per pixel in the flat field taken. Note that traps, which are usually less than 0.1 electrons are not counted for this estimation. However in the trap map for the CCID-35 at most one or none trap greater than 0.1 electrons was found per port (20 x 200 pixels). Hence the average number of traps counted per port is equal or smaller to 1/4000 single electrons traps/pixel. The average global CTE can hence be calculated to 1 - (0.00025/60) = 0.999996. This results matches with the results measured with the extended pixel edge response (EPER) method above.

The test results explained and outlined in section 7.8, were the ability and the efficiency of the CCD to move small charge packages is analyzed in more detail are very meaningful for the application of the CCD. Since in curvature mode only 12 superpixel in the serial register and one column in vertical direction are transferred, CTE can be considered perfect for this application.

7.5 Pocket Pumping experiment and cosmetic quality

Small traps may usually not be detected by X-ray characterization of the CCD device, but they can be clearly located by the technique of pocket pumping. This method amplifies the effects of a trap and can map the exact position, size and even the location of the defect within the pixels for traps of one electron or less in size.

Pocket pumping is performed by first exposing the CCD to a low level flat field of 50 to 100 electrons depending on the size of the trap to be located. After the exposure the CCD is clocked backwards then forwards a specified number of lines for a specified number of times and then the CCD is read out in normal fashion.

The backwards then forwards clocking sequence causes the signal charge to build up or be pumped at the trapping site. The size of the trap site can be calculated by dividing the excess charge at the trap site by the number of cycles.
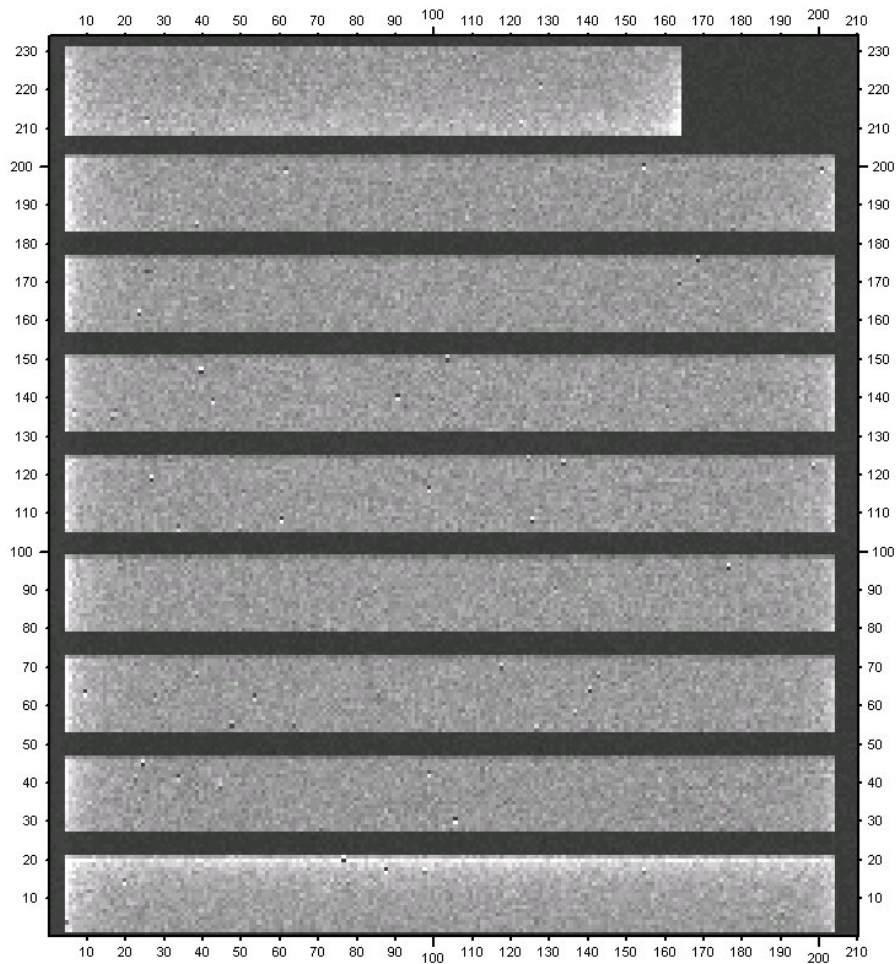
Figure 7-11   Pocket pumping response of the CCID-35 for a flat field of 60 electrons per pixels pumped for 1000 cycles.   The response shows forward and reverse traps smaller than one electron.

Small traps are the result of spurious potential pockets, which result from the loss of charge during transfer due to improper potential well shape and/or depth beneath the pixel. Those effects are often due to channel width variation, polysilicon edge lifting, and typical boron lateral diffusion [Janesick et al., 1993 and 2001].

To test the CCD flat field images with 120 electrons per pixel and flat field images with 60 electrons per pixel were pumped for 1000 cycles to locate very low-level traps in the device. Figure 7-11 shows a pocket pumping trap map that shows trapping sites for the curvature array and the tip/tilt sensor (top readout port in that image) at a light level of 60 electrons per pixel.

The traps are the brighter and dimmer pixels indicating the forward or reverse nature of the trap. The bright spot is always followed by a dimmer pixel since the charge in the bright pixel has to come from another pixel. The forward trap accumulates charge within the pixel containing the trap site. Its dark pixel always proceeds the trap side. On the other hand the reverse trap accumulates charge at the opposite end of the pumping sequence. The dark pixel lags behind the trap. All traps found in the device are statistically smaller than 1 electron of charge, meaning they do not trap charge with 100% probability. The conversion factor of readout sequence was 0.3 electrons/ADU.

This results shows that the CCD is almost perfect in term of cosmetic quality and does not contain any significant traps to influence the operation at low light level. The ability to operate at low flux is analyzed and discussed in section 7-8.
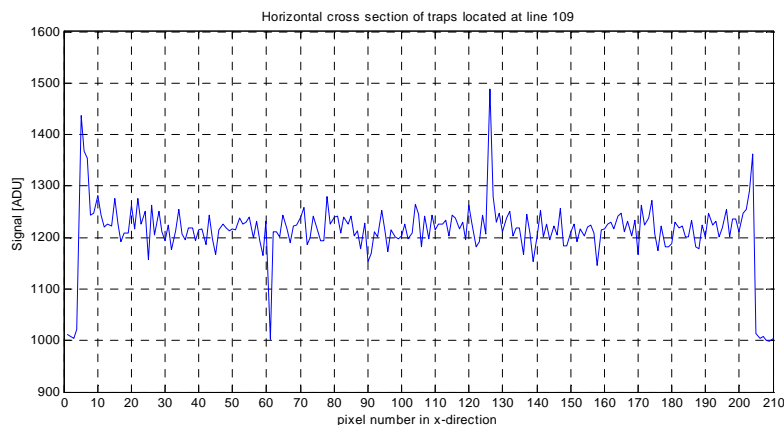
Figure 7-12 Horizontal cross section of the vertical line 109 of Figure 7-11 showing a trap located at x-126 and y-109. Also shown a dark pixel at x-61 and y-109 which is a proceeding a trap at line 110. The trap is very small and contains ~300 ADU equivalent to 90 electrons for charge (conversion factor 0.3 electrons/ADU). Note that the trap was pumped for 1000 cycles, translating the trap size statistically to a "fraction" of an electron.

7.6 Full well capacity and dynamic range

Pixel full well is the amount of charge that a single pixel can hold during integration (for a 18 micron pixel non-MPP device this should be at least 150,000 electrons). When the charge exceeds this value, the pixel will start blooming in vertical direction. If the pixel full well is especially low, it points to an incorrect positive voltage level applied to the parallel clocks.

The largest charge package for good CTE is more difficult to determine. Usually CTE for a given level of a flat field is stated or for a charge packet from an Iron 55 X-ray source (1620 electrons). With correct parallel clock voltage levels the pixel full well and largest charge packet for good CTE should be similar. However this this varies from CCD to CCD. Any deviation from good CTE is seen as a trail of charge in the direction away from the amplifier.

Serial pixel full well should usually be 2 to 3 times larger than the pixel full well, simply due to the geometric difference in the size of pixels in the serial register (they are 2-3 times wider, i.e. 36 to 50 microns wide).

Furthermore there is the amplifier full well, which is the amount of charge for which the amplifier output stays within 1% of linearity. As more charge is put on the gate of the amplifier, the amplifier output tends to saturate. Most CCD amplifiers work linearly over a range of 2 Volts. With the high responsivity of the MIT/LL amplifier, 15 microvolts per electron, the amplifier full well should be around 100,000 electrons.

For the curvature CCD the amplifier full well should be the lowest limit of full wells. That is (for a fully working CCD), the maximum charge packet size, defined by the amplifier full well and not pixel full well or CTE limitations.

During the test phase of the frontside versions of the CCDs from the first wafer run it was found, that the full well capacity was much lower than expected from the design calculations. Figure 7-13 shows an image of the curvature array and the tip/tilt sensor at an illumination level of ~25,000 electrons per pixel.

In the pixels of the spots the full well capacity of the serial register is exceeding. This is visible as deferred charge trails after the bright pixels. Various tests have been performed to localize the problem by varying the voltages for the clockphases to improve the full well capacity but none resulted in a higher full well. However the tip/tilt sensor on the device did not show those problems and a full well capacity of ~90,000 electrons/pixel was measured. With the first devices received from MIT/LL we encountered similar problems.

Fortunately a possible cause was found not to be a design problem but rather a process problem that we thought we could fix on the remaining wafers. The problem had to do with the metal traces as they go over polysilicon lines. It was found by probing that there were occasional discontinuities (open circuits) in the metal as it crossed polysilicon lines. The edges of the polysilicon lines are nearly vertical, and this can create conditions that lead to breaks in the metal.

This device is particularly prone to this problem because it needs a lot of crossovers to distribute the clock signals among the eight columns of the curvature sensor. The tip-tilt sensor does not have nearly as many crossovers, and that is probably why it works better. The CCDs were studied with a SEM (scanning electron microscope) to confirm this picture. To fix the problem the devices went through another process to cure the step-coverage problem.

The yield for working devices improved but still we measured low full well also with those devices.   The problem is not yet fully understood in detail and still under investigation at MIT/LL. However it is limiting the full well capacity of the frontside

curvature CCDs to about 10,000 to 20,000 electrons per pixel depending on the device. We are confident to find the cause of this problem in the near future and another wafer-run with the same mask set is planned after identifying the process problem.

However, with a full well capacity of 10,000 to 20,000 electrons the CCDs are still suited for the application. Even with a ful well capacity of 10,000 electrons the dynamic range of the curvature CCD is still higher by a factor of 100 compared to avalance photo diodes.
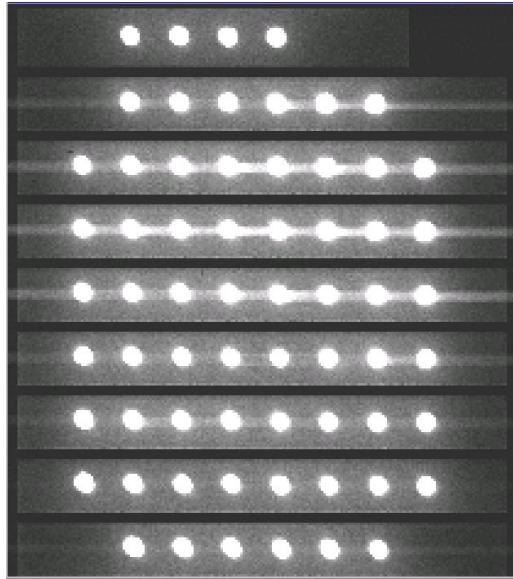
Figure 7-13 CCID-35 image with on average 25,000 electrons per pixel in the spots exceeding the full well capacity of the serial register seen as deferred charge trails after bright pixels. The cause of this problem is currently not fully understood but it limits the use of the frontside versions of the CCD to signal levels of 20,000 electrons per pixel or less depending on the device.

7.7 Dark current and cosmic radiation

Influence of cosmic radiation

High energy sub atomic particles (protons) entering the Earth's atmosphere from space generate a shower of secondary cosmic radiation called muons, which can be stopped by thick layer of silicon. The energy released can generate around 80 electrons per pixel per micron of thickness in the silicon [Mc Lean, 2000].

As mentioned in chapter 5, the frontside devices are 675 µm thick. Hence the electron lifetime in the silicon is very long and the ionization trail from any charged particle (from cosmic rays but also from trace radioisotopes in the environment, potassium-40 being a prime example) is collected from the whole bulk by the CCD.

Figure 7-14 shows an image of the CCD, which was exposed 1 hour in the dark. Huge clouds of charge caused by cosmic rays are visible. The portion of the trail from deep

inside the chips becomes very broad due to diffusion, while the portion near the surface is much narrower, hence one can see cone shaped trails for some of them.

Thinned, backside illuminated devices produce events that occupy only very few pixels. This was verified with the 20 μm thick backside MIT/LL CCID-20 [Dorn, 2000], now used in the UVES detector system at ESO. Since the CCD is operated at 4000 frames per second under normal operation, it was not detected on the first glance.

To measure dark current a careful examination of the individual long exposure frames of the CCD was neccesarry to avoid regions with charge generated by cosmic radiation, giving a false signal level.
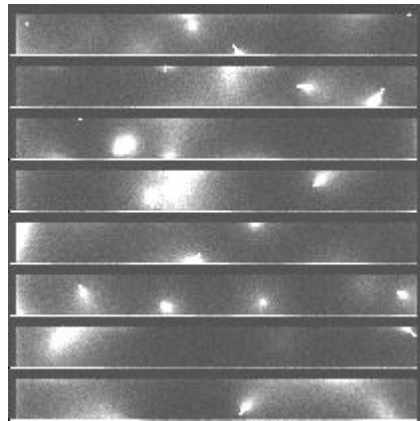
Figure 7-14 One hour dark frame of the thick frontside CCID-35. Huge clouds of charge caused by cosmic rays are visible. The portion of the trail from deep inside the chips becomes very broad due to diffusion, while the portion near the surface is much narrower, hence one can see cone-shaped trails for some of them.

Dark current

The reduction of dark current to a negligible level was a very important requirement for the curvature AO CCD to be limited by readout noise. For the 360 x 360 micron superpixel we wanted to have less than 0.25 electrons dark current per frame where the slowest frame rate of the device is 50 Hz, a frame time of 20 ms.

Dark current is the spontaneous generation of electrons in the silicon due to thermal excitation. These thermally generated electrons represent the limit of noise performance in a CCD. According to Janesick [Janesick, 2001] there are three main sources for dark current generation in CCDs.   They are 1) thermal generation and diffusion in the substrate silicon, 2) thermal generation in the depletion region and 3) thermal generation due to surface states at the Si-SiO$_2$ interface.   Among these three the most dominant dark current contributor is the generation due to surface states at the Si-SiO$_2$ interface.

A prior theoretical calculation (c.f. Figure 5-16) showed that the CCD needs to be cooled to 192 degree Kelvin and this was an estimation to decide whether the prototype systems will use liquid nitrogen or can be cooled thermoelectrically.

To verify the calculations dark current versus operating temperature was measured and the following plot shows the results. The temperature of the CCD was increased in steps of 5 degree Kelvin and 12 half hour frames and several 0 second exposure frames were acquired.

Due to the large effect of cosmic radiation on the thick devices each frame was reduced individually to find regions only dominated by dark current and not affected by charge generated by cosmic rays. The following figure plots dark current versus temperature for a single pixel per second and dark current per superpixels (i.e. 400 pixels) per 20 ms. For comparison the calculated values are plotted as dashed lines. However there is a discrepancy between the calculated dark current and the measured dark current as seen in Figure 7-15. This could be due to an error in the estimated value of 1 nA per square centimeter at 300 degree Kelvin. Dark current gets extrapolated from this value.

The results also clearly indicate that the CCD is not influenced by spurious charge generation, which would result in a higher dark current. However, it was found that the CCD needs to be cooled to ~197 degree Kelvin to meet the requirements to be limited by readout noise of 0.25 electrons per superpixel at a 50 Hz frame rate.
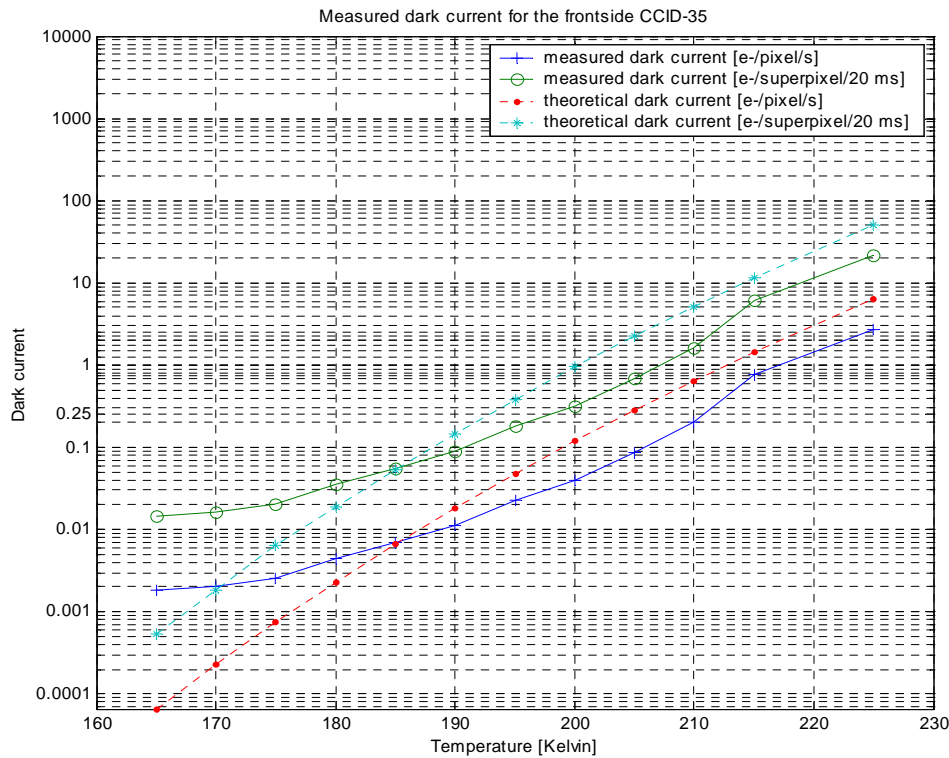
Figure 7-15   Measured dark current versus temperature for a single pixel per second and dark current per superpixels (400 pixels) per 20 ms. For comparison the calculated values are shown as dashed lines in the plot.

7.8 Low light level operation

Besides low noise capability of the curvature CCD, the CCD must also be able to transfer small charge packages down to one electron with high efficiency to be used as a low light level wavefront sensor in adaptive optics.

Traps, which absorb and release electrons on a very short timescale can cause a fluctuation in the charge of the pixel and hence add to noise of the CCD. A good feature of the buried channel CCDs is that the CCDs are less sensitive to trap charges as explained in chapter 5. CTE usually is dependent on the amount of charge being transferred because low-level cosmetic defects can trap small charge packages in a pixel. At low light levels problems usually occur when the potential wells are almost empty or just have a small charge package stored. To be able to move single electrons with good charge transfer efficiency, there is a notch in the channel design of the CCID-35s, which reduces the ability of traps to capture electrons. Doping a narrow region within the main signal channel with typically phosphorus forms a notch channel. For the CCID-35 this notch or trough is 2 microns wide in the image pixels and 3 microns wide in the serial pixels.

To verify the capability of the CCID-35s to move very small charge packets with high efficiency, the input illumination on the fiber entrance was turned down with neutral density filters to give a signal of ~1 electron per pixel per exposure. Figure 7-16 shows a strip of a CCD image for one amplifier with a readout noise of 1.4 electrons. The signal produced in the fiber spots is almost not visible and embedded in the noisy trace of the readout noise. Hence 256 exposures with the same illumination level were summed up and normalized. Figure 7-17 shows this image and the horizontal cross section of the spot signals.
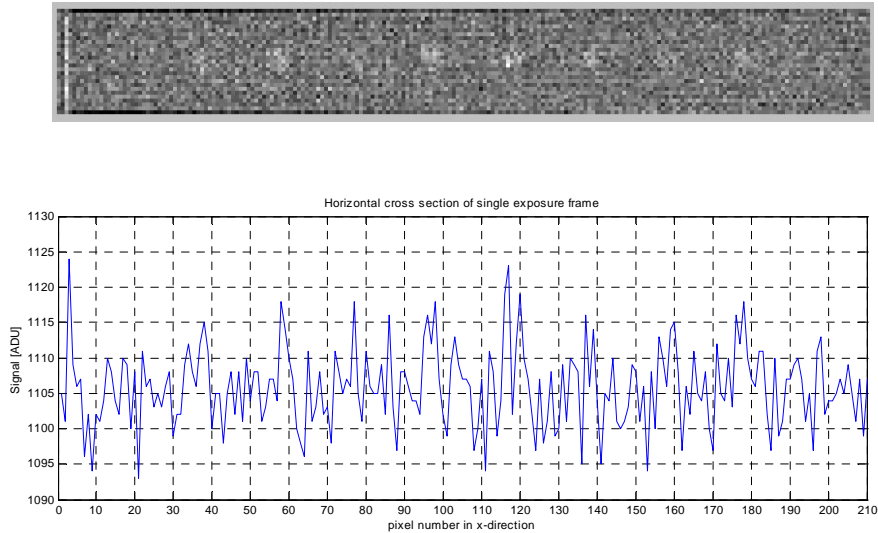
Figure 7-16 CCD image with ~ 1 electron charge per pixel and a readout noise of 1.4 electrons and its horizontal cross section.
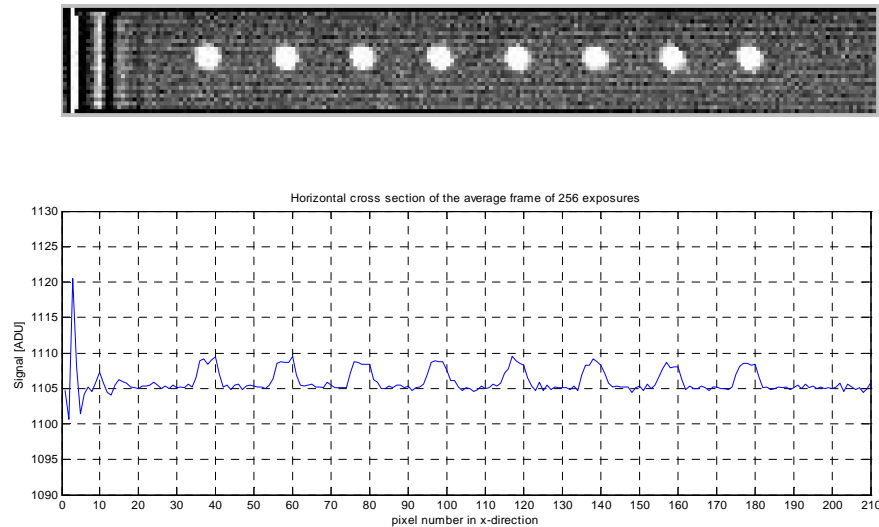
Figure 7-17 Average frame of 256 CCD image with ~1 electron charge per pixel and a readout noise of ~0.1 electrons and its horizontal cross section.

The charge is clearly visible and was measured to be 4 to 5 ADU (1 to 1.5 electrons) on average per pixel per frame. Due to averaging the single exposures, the signal to noise ratio was improved and the random noise was reduced and measured to be about 0.1 electrons.

Traps or blemishes however would also be seen in that image but the CCD has an extremely good cosmetic quality as outlined in section 7.5. The single electron events that made up the signal in the low light level frame are clearly separated in the average frame and indicate that single electrons have been transferred with a high efficiency throughout the device. The ramp-up effect seen at the beginning of the image (first 20 pixels) is not due to a trap in the CCD, it is due to a warm-up effect in the electronics at the beginning of the readout of the serial register. Since the CCD consists of 80 subapertures there was no need to use the first superpixel of each CCD column.

Going to even lower light levels was one of the most interesting tests with the curvature CCD to show that the CCD can transfer also very low signal charges per subaperture i.e. a 20x20 binned superpixel. To verify this capability a single image taken at a specific light level was compared with another image obtained by adding a large number of individual images each taken at a much lower light level. Hence the total number of photons per pixel in the two images should be the same. This was done at a number of light levels and the results are very consistent.

Figure 7-18 shows a series of images of the curvature CCD with the first 4 amplifiers of the CCD i.e. 30 subapertures. The first image is an exposure adding up charge for 4 cycles, resulting in an image with ~1 electron charge per subaperture. The signal is completely embedded in the noise of the frame. The second image shows the sum of 16 four-cycle images and the third image shows a sum of 256 four-cycle images added together. For both the 16 image sum and the 256 sum the signal in the individual subapertures is clearly visible. For comparison the last image shows a frame at much higher signal levels to identify the subapertures fed with photons by the fibers.
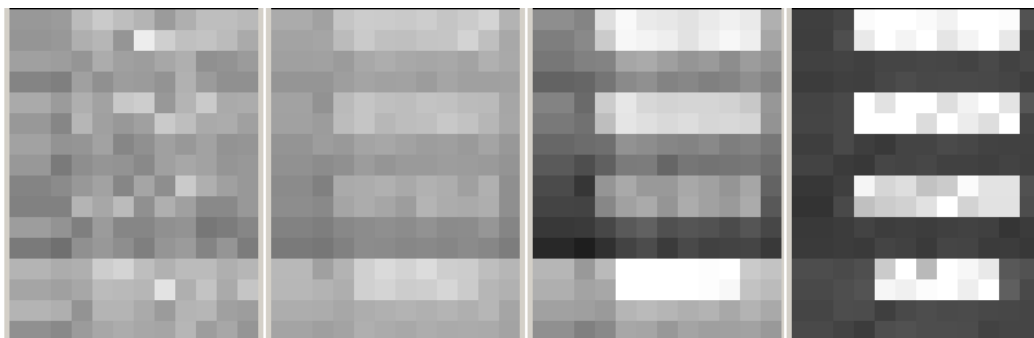
(1)   (2)   (3)   (4)

Figure 7-18 (1) Image adding up <u>extrafocal</u> and <u>intrafocal</u> charge for four cycles, resulting in an image with ~1 electron charge per subaperture. The signal is completely embedded in the noise of the frame. (2) Sum of 16 four-cycle images and (3) sum of 256 four-cycle images added together. For both the 16 image sum and the 256 sum the signal in the individual subapertures is clearly visible. For comparison, the last image (4) shows a frame at much higher signal levels to identify the subapertures fed with photons via the fibers.

Figure 7-19 shows similar images of the same kind, but the LED has been switched on only during the intrafocal integration times of the readout mode. Hence only the subaperatures for the intrafocal photons contain the charge. This result also demonstrates that the CCD is not only able to move very low charge packages within the CCD, it shows also that the charge movement goes in the desired direction.
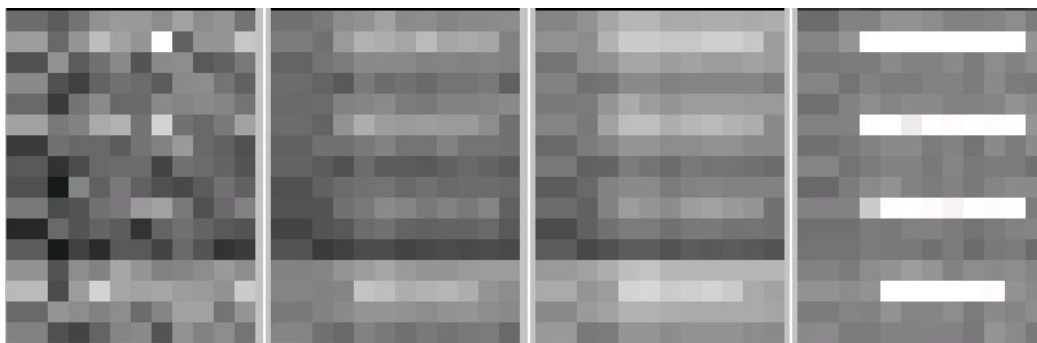
(1)   (2)   (3)   (4)

Figure 7-19 (1) Image adding up only <u>intrafocal</u> charge for four cycles, resulting in an image with ~1 electron charge per subaperture. The signal is completely embedded in the noise of the frame. (2) Sum of 16 four-cycle images and (3) sum of 256 four-cycle images added together. For both the 16 image sum and the 256 sum the signal in the individual subapertures is clearly visible. For comparison, the last image (4) shows a frame at much higher signal levels to identify the subapertures fed with photons via the fibers.

These images show qualitatively how well the curvature CCD is transferring charge at extremely low light levels and that the signal detected in the image depends only on the integrated signal levels and not on the numbers of images added together to achieve this signal level. This chapter shows that the CCD meets all the requirements needed to be able to be used as a wavefront sensor in a low light level curvature adaptive optics system. With the results of the CCD characterization another simulation run was started to compare the performance of the CCD in contrast to avalanche photo diodes traditionally used for curvature wavefront sensing in astronomy. The results of this simulation are presented in the last section of this chapter.

7.8 CCD performance compared to APDs

With the results from the CCD characterizations, another simulation was started to compare the performance of the CCD with respect to the performance of the avalanche photo diodes for the 60 – element MACAO system accounting the results obtained with the characterization of the CCDs. The properties and simulation parameters are listed in Table 7-4 and Table 7-6.

Property	APD	CCD
Sky background magnitude	19.0	19.0
Field of view diameter	2"	2"
Quantum efficiency	70%	80%
Dark current [electrons/s]	250	0
Read-out noise [electrons RMS]	0	1.5
Read-out delay [µs]	0	250
Seeing [arcsec]	0.65	0.65

Table 7-4 Specifications of the curvature wavefront sensor detector for APDs and CCD.

Guide star magnitude	APD	CCD
10	0.638	0.636
11	0.627	0.624
12	0.608	0.605
13	0.575	0.570
14	0.503	0.503
15	0.407	0.371
16	0.231	0.241
17	0.108	0.127
18	0.051	0.054

Table 7-5 Strehl ratios achived with APDs and the curvature CCD with 80% quantum efficiency.

Figure 7-20 shows the results for CCD. The CCD performs as well as APDs over the entire range of magnitudes down to very faint guide stars at magnitude 18. The plot shows a small difference of the performance of the CCD of 3% at magnitude 15 compared to APDs. At lower light levels the CCD outperforms the APDs due to its higher quantum efficiency.

Note that this comparison is only a relative comparison between the detectors and not in terms of absolute Stehl for an AO-system. Different models of the atmosphere and the inner setup of the rest of the AO system like the characteristics of the deformable mirrors would give a different result in overall Strehl. However this does not affect the relative comparison of the wavefront sensors. For convenience, the results of are also listed in tabular form in Table 7-5.
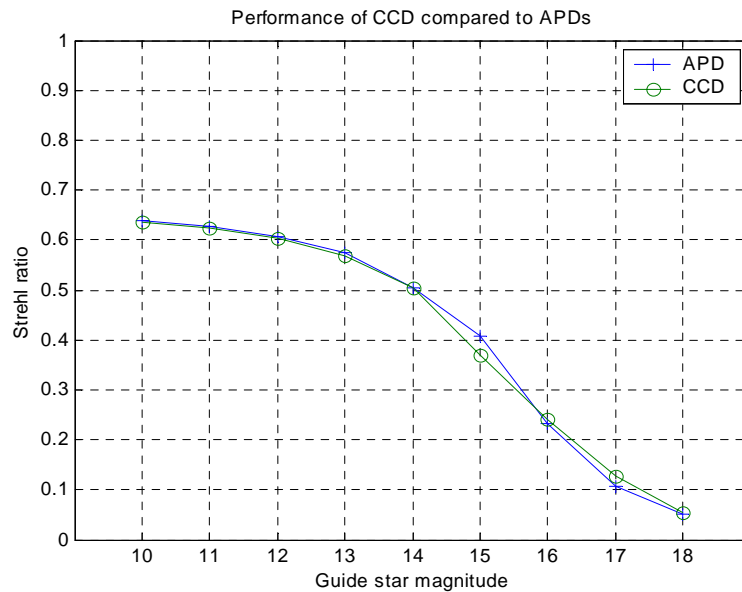
Figure 7-20 Performance of the curvature CCD with 80% quantum efficiency compared to avalanche photodiodes.

Guide star magnitude	Photon flux per subaperture [1/s]	Integration time [ms]	Loop gain	Photon flux* per integration [1/s]
10	$952 \cdot 10^3$	2.0	0.60	1904
11	$379 \cdot 10^3$	2.0	0.50	758
12	$151 \cdot 10^3$	2.0	0.40	302
13	$60.1 \cdot 10^3$	2.0	0.30	120
14	$23.9 \cdot 10^3$	5.0	0.60	120
15	9520	5.0	0.50	47.6
16	3790	6.5	0.30	24.6
17	1510	15.0	0.30	22.7
18	601	40.0	0.30	24.0

Table 7-6 Loop gains and integration times.

*on the detector – to get number of photoelectrons, multiply by the detector QE.

Chapter 8

SUMMARY AND CONCLUSIONS

The comparison in the last section of this thesis where photon counting detectors such as avalanche photodiodes were compared to the curvature CCD showed that the influence of 1.5 electrons readout noise is remarkably small. With this readout noise the CCD with 80% quantum efficiency performs as well as APDs down to the lowest light level. Since the wavefront sensor detects the light in the visible, many photons are required to obtain a good signal to noise ratio.

Glindemann and Rees, who used computer simulations to compare three different wavefront sensors in the presence of noise, also investigated the influence of readnoise with wavefront sensors in the past. Glindemann concluded that a CCD with 5 electrons readout noise performs similar to a photon counting detector [Glindemann and Rees, 1994 and Glindemann, 1997].

Furthermore the quantum efficiency of the CCD is really 20% higher than that of avalanche photo diodes, but the additional relay optics used in the prototype system brings this difference down to 10%. In future systems, the relay optics and the consequent loss of light can be avoided by placing the fibers coming from the 60 subapertures of the lenslet array directly in front of the CCD or the use of a lenslet array to directly image the subapertures on the CCD. The design of such a lenslet array seems to be feasible and first calculations and optical simulations have been carried out [Delabre, 2000]. This is still in the design phase and needs more investigation in the future.

Another result, which was found by the computer simulations, was the fact that, for a 60 element curvature AO system, the instantaneous Strehl was significantly higher than the integrated Strehl. The reduction of integrated Strehl is due to image wander and had been speculated for curvature systems with many subapertures [Northcott, 1999]. Francois Rigaut also concluded this in a computer simulation done for a comparison of Shack-Hartmann and curvature AO-systems for the 8 m Gemini Telescope [Rigaut, 1997]. To verify this in more detail the simulations were modified to include a separate tip/tilt sensor that used 20% of the light. This gave a significant improvement to integrated Strehl, as

shown in Figure 4-11. To be able to recover this difference, a separate tip/tilt sensor was included in the curvature CCD to combine high order curvature sensing with the possibility of separate tip/tilt sensing in one sensor.

It was demonstrated that the CCD can be operated at noise levels down to 1.3 to 1.5 electrons at a frame rate of 4000 frames per second. This was possible by binning all pixels per subaperture and hence read the serial register at slower speed i.e. 20 µs per superpixel. It was also possible to maintain this noise performance for longer integration times (i.e. integration for more cycles of the membrane) due to the novel design of adding up the charges on the CCD. Readout noise has been one of the most limiting factors in using standard format CCDs as the wavefront sensor in curvature systems. Furthermore a very demanding requirement for the curvature CCD, the ability to move very small charge packages with high efficiency to be well suited for such low light level application was demonstrated to be very efficient.

The CCD provides a much greater integration area per subaperture (360 µm by 360 µm) compared to avalanche photodiodes, which are limited to using 100 µm fibers in diameter. This allows the use of fibers twice the size (200 µm in diameter), which doubles the field of view from 3 arcsec to 6 arcssec. The bigger subapertures also relax the alignment tolerances for the lenslet array optics to couple the light into the fiber inputs.

APDs generate dark current, or false photon counts, of 100 to 250 counts per second depending on the cost of the APDs, while the to ~197 degree Kelvin cooled curvature CCD generates a negligible amount of dark current (0.25 electrons per subapearature at 50 Hz frame rate). The dark current of the APDs affects the performance of the system when faint guide stars are used. However there is a drawback of cooling the CCD since it needs to be cooled with liquid nitrogen. It is very difficult to cool the CCDs thermoelectrically to temperatures down to 197 degree Kelvin. This requires a constant supply of liquid nitrogen to the sensor, which is certainly a drawback in maintenance and size and needs to be considered for the use of the CCD at the telescope. However the CCD based curvature wavefront sensor provides a smaller and more compact design which is easily expandable to higher order systems by building a mosaic of many CCDs in one cryostat and then fed via fibers.

The use of APDs as the wavefront sensor furthermore requires neutral density filters in order to not to destroy the detector and also to reduce the light for bright objects due to its limited dynamic range. For the duration of the avalanche of electrons – typically around 40 ns – the APD is blind to any new photons arriving. This limits the dynamic range of the APD. Also a security system is needed at the telescope to avoid sudden light getting to the diodes. The neutral density filters and the accompanying filter-wheels required for the APDs increase the mechanical complexity of the system. In contrast, the CCD should provide a dynamic range 1000 times that of APDs and hence no neutral density filters are needed and no security measures have to be taken for excess light reaching the detector. The CCD provides a much more reliable and simpler setup. It needs to be noted that we encountered a process problem on the first wafer run of the curvature CCDs, limiting the dynamic range to 10,000 to 20,000 electrons per pixel. The cause of this problem is not yet fully understood and under investigation at MIT/LL, who produced the devices. There will be an additional wafer run with the same mask set to produce additional curvature CCDs once the cause of this problem is fully investigated. However this is not a critical problem

for this application and the dynamic range is still greater by a factor of 100 compared to the dynamic range of avalanche photo diodes.

It can be concluded that back illuminated curvature CCDs provide a real alternative to APDs for high order curvature AO systems with the many advantages outlined above. Still, there is a readnoise of 1.5 electrons which presently limits the performance of CCDs as photon counting detectors but advances in the design of CCDs in the last year (LLLCCD technology) showed that it will be possible in the future to design CCDs which are essentially noiseless and can be used as photon counting detectors [Mackay et al., 2000]. The readout structure of these devices can be combined with the functionality of the curvature CCD design and hence provide a virtually noise free detector for curvature wavefront sensing.

With the reduced cost, about half of that of APDs, it would even be possible to use two detectors in a curvature AO system, one in the extrafocal plane and one in the intrafocal, avoiding the need for a membrane. This would provide a much simpler and less complex system. It has the advantage that photons can be collected over the full extrafocal and intrafocal times. However the sensors would need to be carefully calibrated to avoid any differences in gain and other detector parameters.

The future research for the curvature CCD implies the evaluation of thinned, high quantum efficiency CCDs, which will be available by the end of 2001 and the investigation to put fibers directly in front of the CCD to avoid light loss due to the relay optics. Furthermore the wavefront sensor needs to be interfaced to the MACAO system and to first proof its ability with a lab system and later the performance of the wavefront sensor on the telescope. In the future, AO-systems with hundreds of subapertures will be built. For such systems, the difference in cost and reliability between APDs and the CCD will become very significant. With these systems in mind, the development and use of the curvature CCD seems all the more feasible.

Finally we can conclude from this thesis that CCD detectors, or detectors in general, can be successfully designed for special purposes. With the growing demand in astronomy to build bigger telescopes, to detect fainter objects, combining the light of many telescopes as done with interferometers, the need for specially designed detectors, adapted to the specific applications, will grow. Due to the need of excellent performance, those detectors will possibly never be available as off-the-shelf detectors. Hence research and development in special detectors should always be kept in mind to meet the needs of future instruments.

APPENDIX A

Picture of the wafer with the curvature CCDs
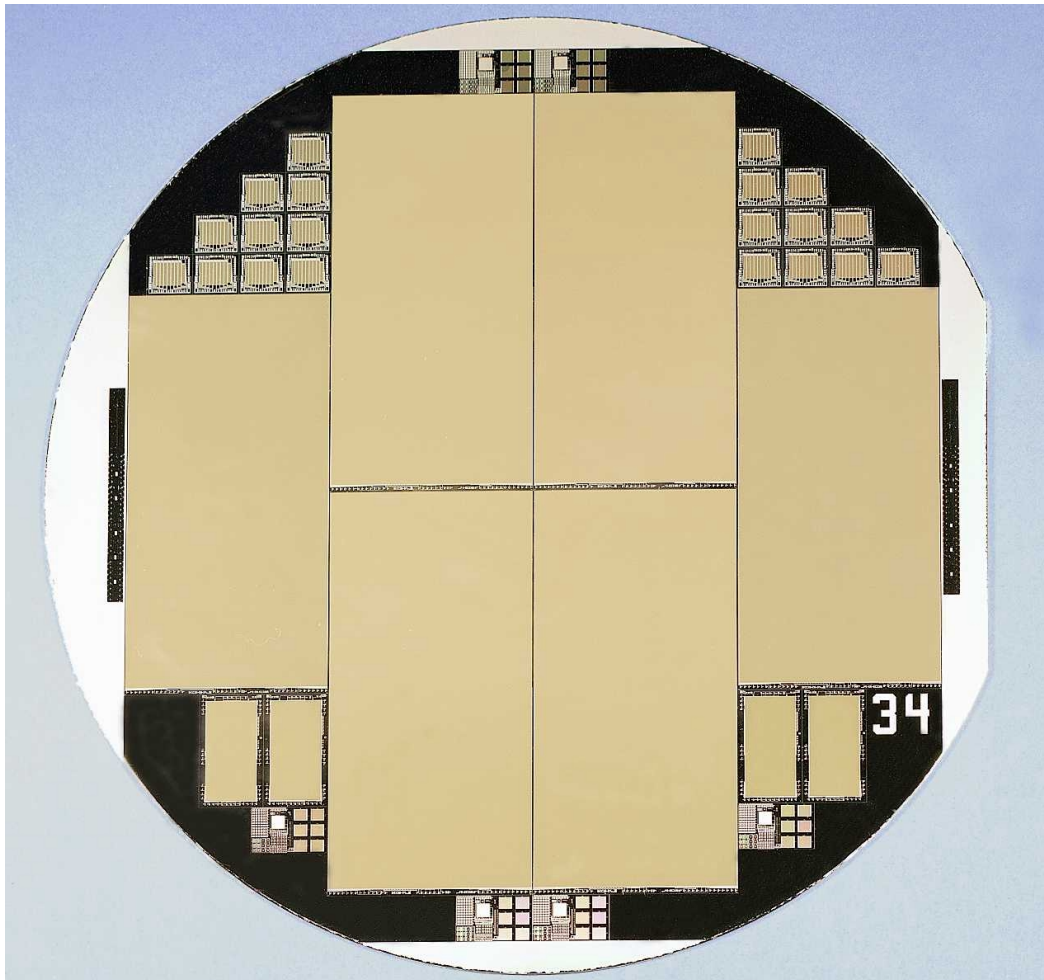
APPENDIX B

Picture of the CCID-35 die
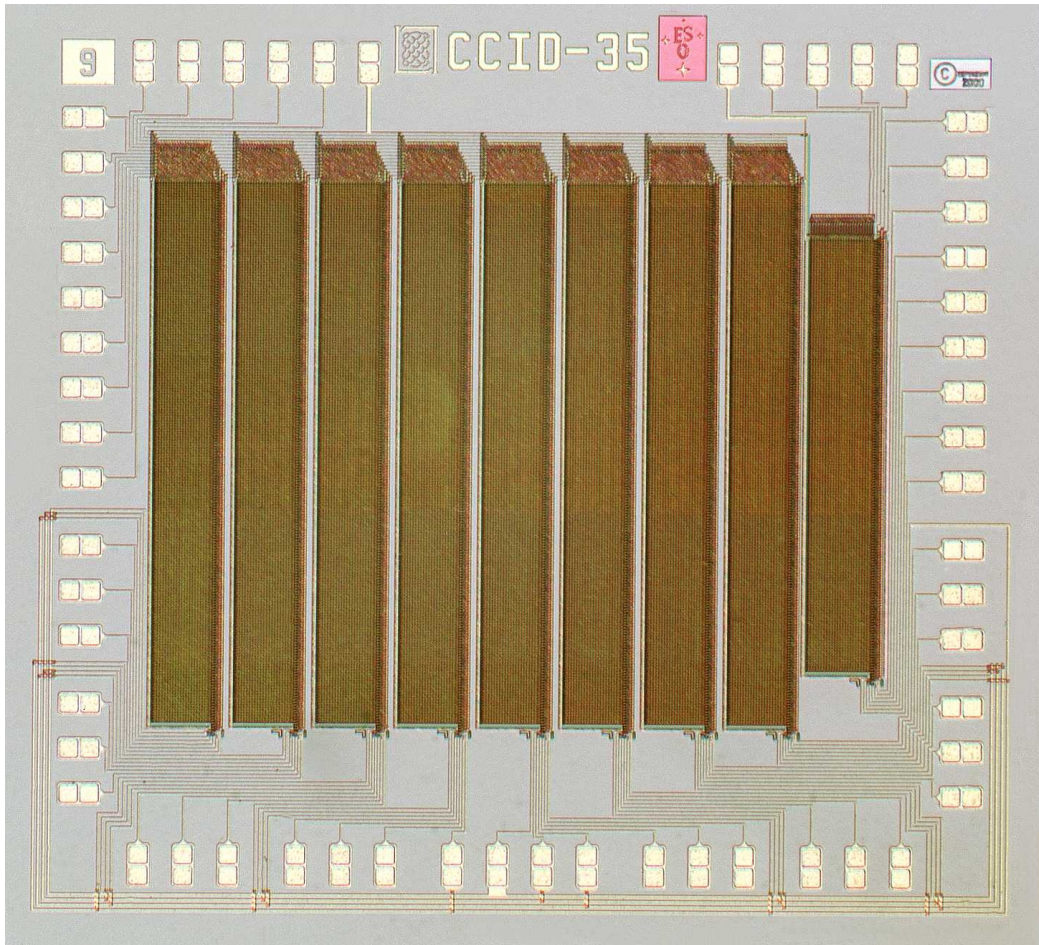
APPENDIX C

Package layout of the frontside curvature CCD array

APPENDIX D

Voltage setting for the clock and bias phases of the frontside CCID-35

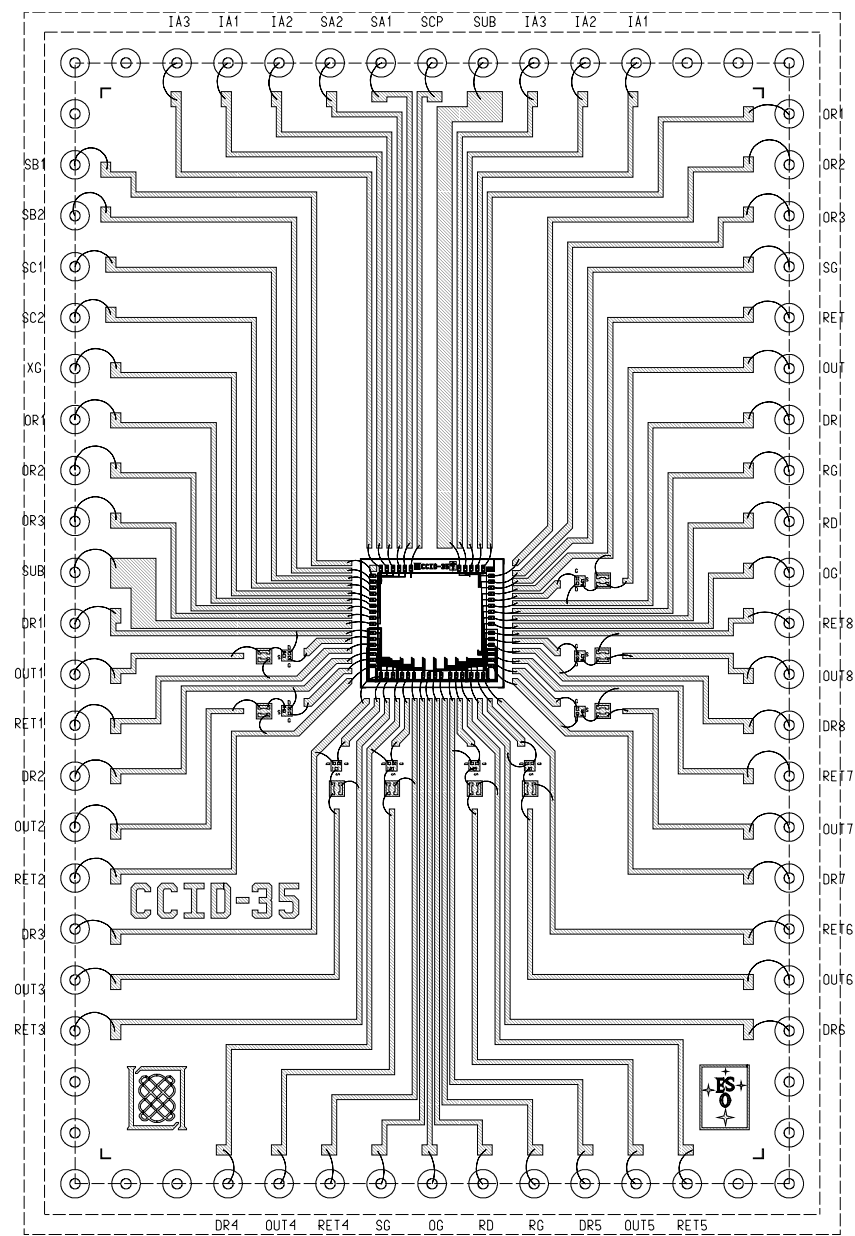| Clock phases curvature array	naming	Low rail voltage	High rail voltage
Imaging area phase 1	IA 1	-6 V	+4 V
Imaging area phase 2	IA 2	-6 V	+4 V
Imaging area phase 3	IA 3	-6 V	+4 V
Storage area A phase 1	SA 1	-6 V	+4 V
Storage area A phase 2	SA 2	-6 V	+4 V
Storage area B phase 1	SB 1	-6 V	+4 V
Storage area B phase 2	SB 2	-6 V	+4 V
Storage area C phase 1	SC 1	-6 V	+4 V
Storage area C phase 2	SC 2	-6 V	+4 V
Storage area C barrier phase	XG	-6 V	+4 V
Output register phase 1	OR 1	-2 V	+ 5V
Output register phase 2	OR 2	-2 V	+ 5V
Output register phase 3	OR 3	-2 V	+ 5V
Summing well	SB	-2 V	+ 5V
Reset gate	RG	+3 V	+ 10V

Clock phases tip/tilt sensor	naming	Low rail voltage	High rail voltage
Imaging area phase 1	T_IA 1	-6 V	+4 V
Imaging area phase 2	T_IA 2	-6 V	+4 V
Imaging area phase 3	T_IA 3	-6 V	+4 V
Output register phase 1	T_OR 1	-2 V	+ 5V
Output register phase 2	T_OR 2	-2 V	+ 5V
Output register phase 3	T_OR 3	-2 V	+ 5V
Summing well	T_SG	-2 V	+ 5V
Reset gate	T_RG	+3 V	+ 10V

Bias phase curvature array	naming	Voltage setting
Output drain 1	DR 1	21 V
Output drain 2	DR 2	21 V
Output drain 3	DR 3	21 V
Output drain 4	DR 4	21 V
Output drain 5	DR 5	21 V
Output drain 6	DR 6	21 V
Output drain 7	DR 7	21 V
Output drain 8	DR 8	21 V
Reset drain	RD	12.5 V
Output gate	OG	0 V
Scupper drain	SCP	12 V

Bias phase tip/tilt sensor	naming	Voltage setting
Output drain	T_DR 1	21 V
Reset drain	T_RD	12.5 V
Output gate	T_OG	0 V
Scupper drain	T_SCP	12 V

APPENDIX E1

Measured linearity curves for the output amplifiers of the curvature CCD
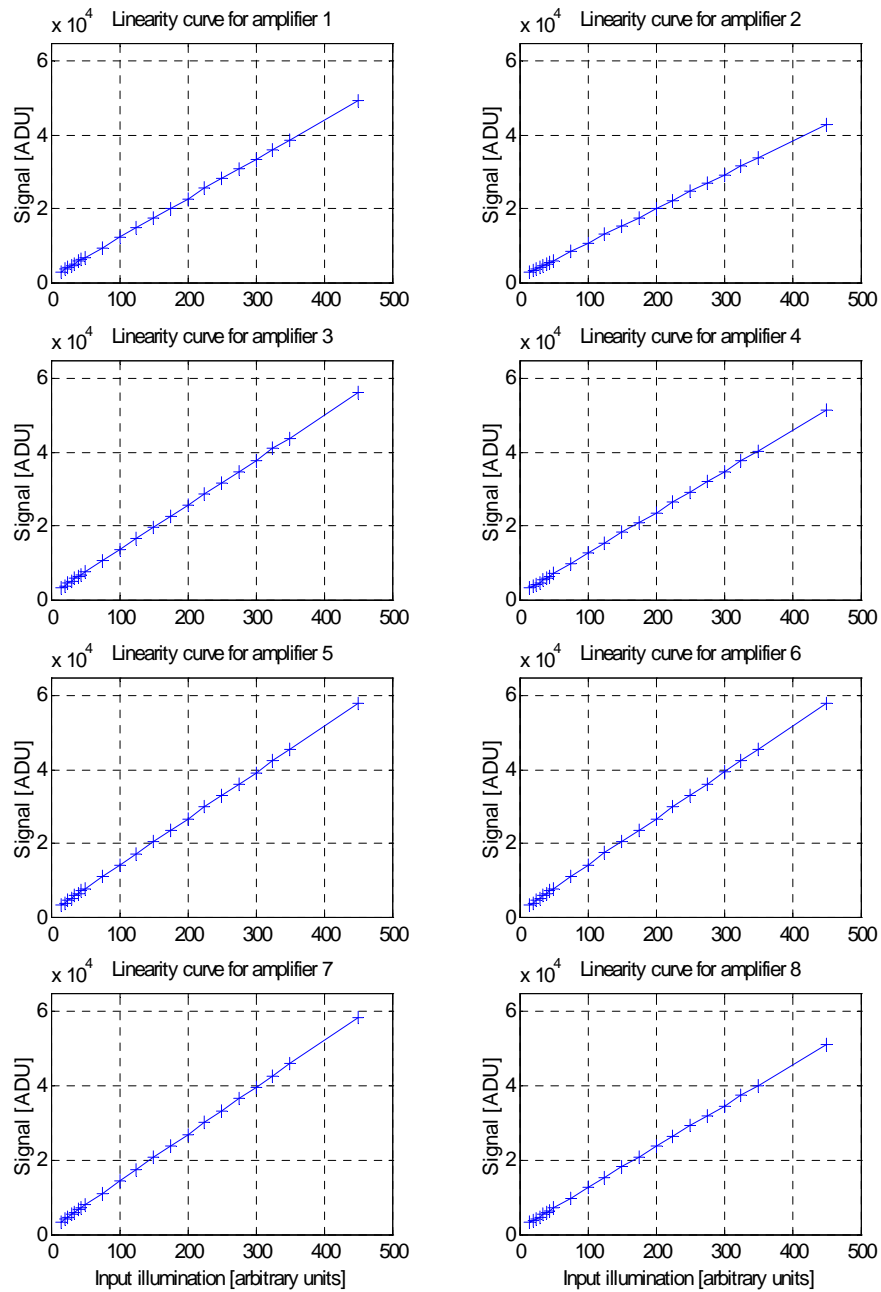
APPENDIX E2

Measured residual non-linearity curves for the output amplifiers of the curvature CCD.

APPENDIX E3

Measured photon transfer curves for the output amplifiers of the curvature CCD

APPENDIX F

Acronyms

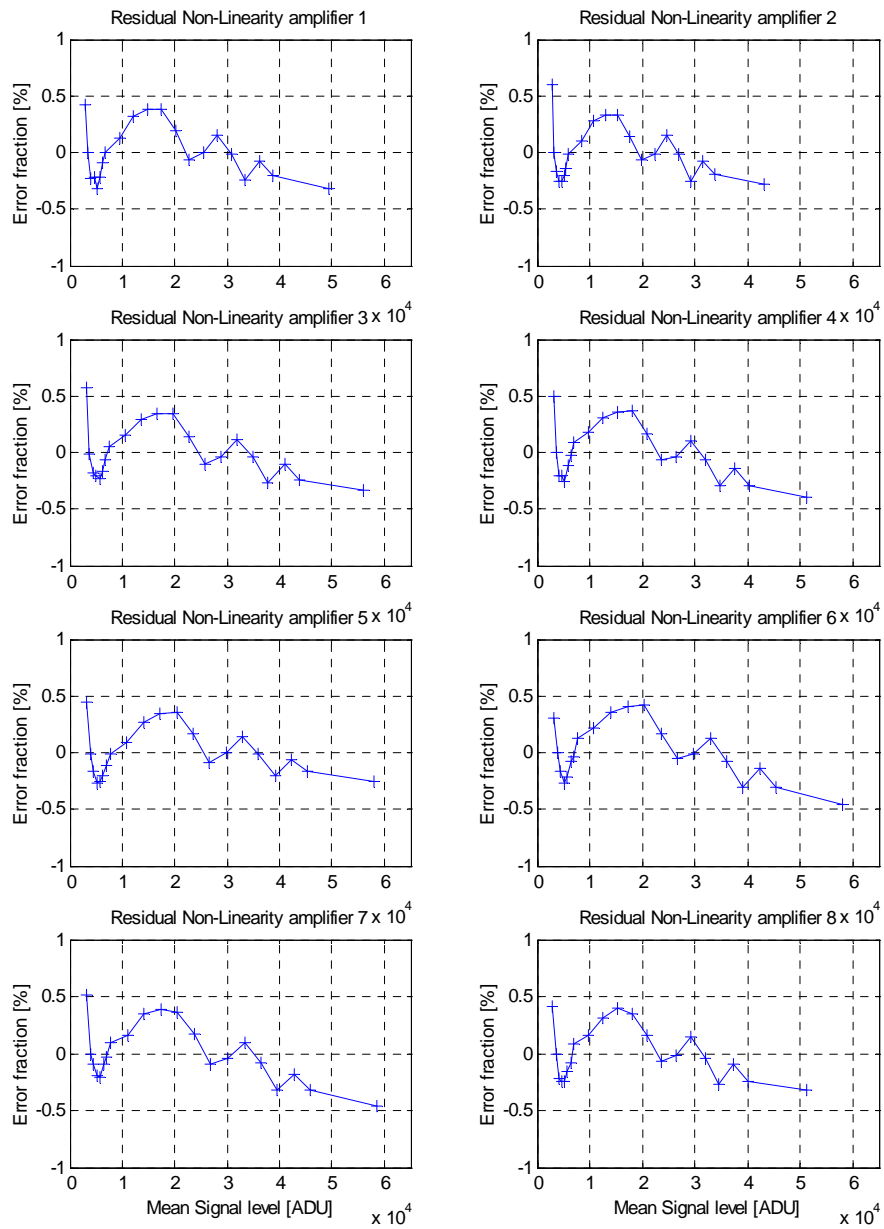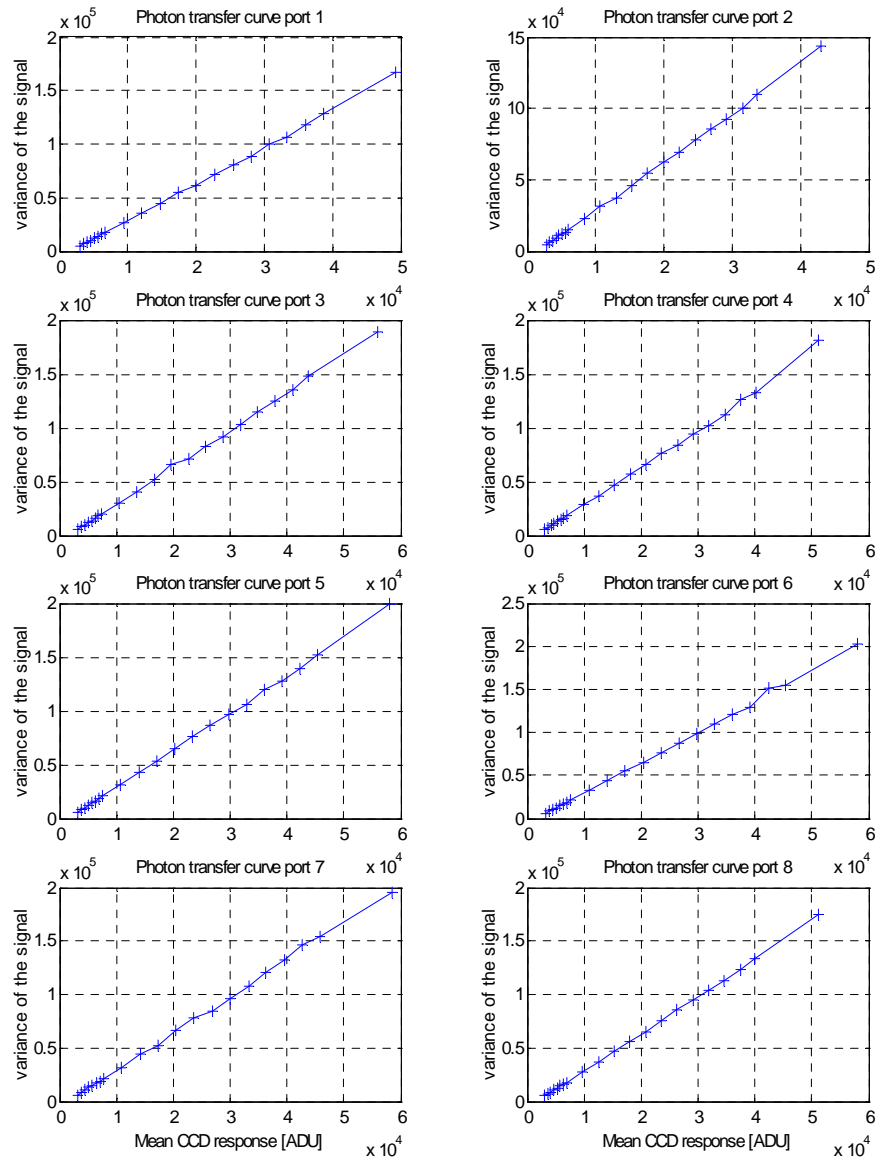| Acronym	Expression
ADC	Analog to Digital Converter
ADONIS	Adaptive Optics near Infrared System
ADOPT	The 100 inch adaptive optics system on Mount Wilson
AdOpt@TNG	Adaptive Optics Module at the National Telescope Galileo
ADU	Analog to Digital Unit
ALFA	Adaptive Optics with a Laser for Astronomy
AO	Adaptive Optics
AOB	Adaptive Optics Bonnette
APD	Avalanche Photo Diode
CB	Conduction Band
CCD	Charge Coupled Device
CFC	Continuous Flow Cryostat
CFH	Canadian French Hawaiian (Telescope)
CONICA	Coude Near Infrared Camera
CRIRES	Cryogenic High Resolution Infrared Echelle Spectrograph for the VLT
CTE	Charge Transfer Efficiency
CTI	Charge Transfer Inefficiency
CWS	Curvature Wavefront Sensor
DAC	Digital to Analog Converter
DM	Deformable Mirror
DR	Drain
DSP	Digital Signal Processing
EBCCD	Electron Bombarded Charge Coupled Device
EPER	Extended Pixel Edge Response
ESO	European Southern Observatory
FIERA	Fast Imaging Electronic Readout Assembly
FIFO	First Input First Output
FWHM	Full With Half Maximum
IA	Imaging Area
IC	Integrated Circuit
JFET	Junction Field Effect Transistor
LED	Light Emitting Diode
LGS	Laser Guide Star
LLLCCD	Low Light Level Charge Coupled Device
LLNL	Lawrence Livermore National Laboratory
MACAO	Multiple Applications Curvature Adaptive Optics
MIT	Massachusetts Institute of Technology
MIT/LL	Massachusetts Institute of Technology/Lincoln Laboratory
MOS	Metal Oxide Semiconductor
MOSFET	Metal Oxide Semiconductor Field Effect Transistor

MPP	Multi Pinned Phase
NA	Numerical Aperture
NAOS	Nasmyth Adaptive Optics System
NTT	New Technology Telescope
OG	Output Gate
OR	Output Register
PCB	Printed Circuit Board
PRNU	Pixel Response Nonuniformity
PSF	Point Spread Function
PTC	Photon Transfer Curve
PV	Peak to Valley
PWS	Pyramid Wavefront Sensor
PUEO	(see AOB)
QE	Quantum Efficiency
RC	Resistor Capacitor Network
RGO	Royal Greenwich Observatory
RMS	Root Mean Square
RNL	Residual Non Linearity
SA	Storage Area A
SB	Storage Area B
SC	Storage Area C
SEM	Scanning Electron Microscope
SI	Shearing Interferometry
SINFONI	Single Far Object Near-ir Investigation
SLCU	SPARC Local Control Unit
SPARC	Scalable Processor Architecture
SR	Strehl Ratio
SW	Summing Well
VB	Valence Band
VLT	Very Large Telescope
VLTI	Very Large Telescope Interferometer
WFS	Wave Front Sensor
XG	Transfer Gate

BIBLIOGRAPHY

Arsenault, R. (2001), ESO, private communication.

Avilia, G. (1999), ESO, private communication.

Babcock, H. W. (1953), "Possibility of compensating astronomical seeing", in *Publ. Astron. Soc. Par.*, **65**, 229.

Beletic, J. W., Dorn, R. J.,Craven-Bartle, T., Burke, B. (2000), "A new CCD for curvature wavefront sensing" in *ESO workshop on Optical Detectors for Astromony II*, eds. P. Amico, P. and Beletic, J.W., Kluwer Academic Publishers.

Beletic, J. W., Gerdes, R. and DuVarney, R. C. (1998), "FIERA: ESO's new generation CCD controller", in *Astrophysics and Space Science Library, Optical Detectors for Astronomy*, Kluwer Academic Publishers.

Beletic, J. W., Gerdes, R. and Zipperer, J. (1996), "A DSP-based solution to remote control of detector head electronics for scientific CCD systems", in *DSP-96*, Munich.

Born, M. and Wolf, E. (1970), "Principles of optics", Pergamon Press, Oxford.

Boyle, W. and Smith, G. (1970), "Charge coupled devices", in *Bell Syst. Tech. J.*, **49**, 587-593.

Burke, B. (1999), MIT Lincoln Laboratory, private communication.

Burley, G. S., Walker, G. A. H. and Johnson R. (1998), "A versatile CCD curvature sensor", in *PASP*, **110**, 330-338.

Cavadore C. and Dorn, R. J., Beletic, J. W. (2000), "Charge coupled devices at the European Southern Observatory - performance and results", in *ESO workshop on Optical Detectors for Astromony II*, eds. P. Amico, P. and Beletic, J.W., Kluwer Academic Publishers.

Craven-Bartle, T. V. (2000), "Modelling curvature wavefront sensors in adaptive optics", Master's thesis, Dept. of Applied Physics, Linköpings Universitet (Sweden).

Craven-Bartle, T. V., Dorn, R. J. and Beletic, J. W. (2000), "Computer simulation of CCDs and APDs for curvature wavefront sensing", in *SPIE's International Symposium on Astronomical Telescopes and Instrumentation 2000, Munich, March 27-31, 2000*, SPIE publications.

Delabre, B. (2000), ESO, private communication.

Dorn, R. J. (1996), "CRYMAC, CRYostat Maintenance Controller" in *ESO workshop on Optical Detectors for Astromony*, eds. Beletic, J.W. and Amico, P. , Kluwer Academic Publishers.

Dorn, R. J., Beletic, J. W., Cavadore, C., Lizon, J. L. (2000), "The optical detector systems for the blue and red arms of UVES, the echelle spectrograph for the UT2 Kueyen Telescope at the ESO Paranal Observatory", in the proceedings of the *SPIE's International Symposium on Astronomical Telescopes and Instrumentation 2000, Munich, March 27-31, 2000*, SPIE publications.

Donaldson, R., Bonaccini, D., Brynnel, J., Buzzoni, B., Close, L., Delabre, B., Dupuy, C., Farinato, J., Fedrigo, E., Hubin, N., Marchetti, E., Stroebele, S. and Tordo, S. (2000), "MACAO and its application for the VLT interferometer", in *Adaptive Optical Systems Technology, Munich, Germany, March 27-31, 2000*, proceedings of SPIE, **4007**.

Farinato, J. and Delabre, B. (2000), "Technical specification and statement of work for the MACAO WFS lenslet array", Doc. No. VLT-SPE-ESO-11640-2146.

Farinato, J., Fedrigo, E., Tordo, S., Marchetti, E. and Kasper, M. (2001), "MACAO for VLTI, system design analysis", Doc. No. VLT TRE-ESO-15600-2067, Issue 2.1.

Feutrier, P. and Dorn, R. J. (2000), "NAOS visible wavefront sensor", in the proceedings of the *SPIE's International Symposium on Astronomical Telescopes and Instrumentation 2000, Munich, March 27-31, 2000*, SPIE publications.

Fried, D. L. (1965), "Statistics of a geometric representation of wavefront distortion", in *J. Opt. Soc. Am.,* **55**, 1427-1435.

Fried, D. L. (1966), "Optical resolution through a randomly inhomogeneous medium for very long and very short exposures", in *J. Opt. Soc. Am.,* **56**, 1372-1379.

Geary, J. C. and Luppino, G. A. (1994), "New circular radial-scan fram-storage CCDs for low-order adaptive optics wavefront curvature sensing", in *Adaptive Optics in Astronomy*, proceedings of SPIE, **2201**, 588-595.

Glindemann, A. (1997), "Beating the Seeing Limit -Adaptive Optics on Large Telescopes", Habilitationsschrift Universität Heidelberg.

Glindemann, A. and Rees, N. P. (1994), "Photon Counting versus CCD Sensors for Wavefront Sensing - Performance Comparison in the Presence of Noise", in *Advanced Technology Optical Telescopes V*, proceedings of SPIE 2199, 824-834.

Graves, J. E. and McKenna, D. (1991), "University of Hawaii adaptive optics system III: wavefront curvature sensor", in *Active and Adaptive Optics*, San Diego (California), July 22-24, 1991, ed. Ealey, M.A., proceedings of SPIE, **1542**, 262-72.

Graves, J. E., Roddier, F. J., Northcott, M. J. and Anuskiewicz, J. (1994), "University of Hawaii adaptive optics system IV: a photon-counting cuvature wavefront sensor", in *Adaptive Optics in Astronomy*, Kona, March 17-18, 1994, eds. Ealey, M.A. and Merkle, F., proceedings of SPIE, **220-1**, 502-7.

Haddad, N. and Sinclaire, P. (1997), "PULPO: Temperature, vacuum, shutter, LN2 level, all in one box", in *ESO Workshop on Optical Detectors for Astronomy*, eds. Beletic, J.W. and Amico, P., Kluwer Academic Publishers.

Hardy, J. W., Lefebvre, J. E. and Koliopoulos, C. L. (1977), in *J. Opt. Soc. Amer.*, **67**, 360.

Hardy, J. W., Mac Govern, A. J. (1987), "Shearing interferometer: A flexible technique for wavefront measurment", in *SPIE proceedings of Interferometric Metrology*, **816**, 180-195.

Horwitz, B. A. (1990), "Multiplex techniques for real-time shearing interferometry", in *Opt.Eng.*, **29**, 1223-1232.

Ichikawa, K., Lohmann, A. W. and Takeda, M. (1988), "Phase Retrieval based on the Irradiance Transport Equation and the Fourier Transform Method: Experimentes", in *Applied Optics*, **27**, 3433-36.

Janesick, J., Elliot, T. (1987)," Spurious potentials pockets and pixel nonuniformity in CCDs", in *9th Santa Cruz workshop in Astronomy and Astrophysics*: Instrumentaion for ground based optical Astronomy (Lick Observatory, July 1987).

Janesick, J., Klaasen, K., Elliot, T. (1987), "CCD charge collection efficiency and the photon transfer technique", in *Optical Engineerings*, Vol. **26**, No.10.

Janesick, J., Elliott, T., Bredthauer, R., Chandler, C., Burke, B. (1988), "Fano-noise limited CCDs", in proceedings of SPIE **982**, 70-85.

Janesick, J. (1993), "Locating electron traps in a CCD", NASA Tech. Briefs Vol. 17 No. **9**, pp. 51.

Janesick, J. (2001), "Scientific Charge Coupled Devices", in *SPIE press*, **PM83**, 2001, International Society for Optical Engineering.

Kasper, M. et al. (2000), "ALFA: Adaptive optics for the Calar Alto Observatory", in *Experimental Astronomy*, **10** (I), 49-73.

Kim, C. K., Early, J. M. and Amelio, G. F. (1972), "Buried channel charge coupled devices", in NEREM, Bostion, *Record of Tech. Papers*, **1**, 161-164.

Kolmogorov, A. N. (1961), "The Local Structure of Turbulence in Incompressible Viscous Fluids for Very Large Reynolds' Numbers", in *Turbulence, Classical Papers on Statistical Theory*, eds. Friedlander, S.K. and Topper, L., 151-155.

Koliopoulos, C. L. (1980), "Radial grating lateral shear heterodyne interferometer", in *Appl.Opt.*, **19**, 1523-8.

Lizon, J.L. (1997)," New cryostats for scientific CCD systems in the VLT era", in *The ESO messenger*, **88**, 6-7.

Mackay, C. D., Tubbs, R. N., Bell, R., Burt, D., Moody,I. (2000),"Sub Electron noise at MHz pixel rates" in proceedings of SPIE 43061.

Mahajan, V. M. (1994), "Zernike annular polynominals and optical aberrations od systems with annular pupils", in *Opt. Phot. News*, **5**, Engng Lab Notes

Mahajan, V. M. (1994), "Zernike annular polynominals and optical aberrations od systems with circular pupils", in *Opt. Phot. News*, **5**, Engng Lab Notes.

Merkle, F., Kern, P., Una, P., Rigaut, F., Fontanella, J. C., Rousset, G., Boyer, C., Gaffard, J. P. and Jagourel, P. (1989), "Successful tests of adaptive optics", in *ESO Messenger*, **58**, 1-4.

Noll, R. J. (1976), "Zernike polynoninals and atmospheric turbulence", in *J. Opt. Soc. Am.*, **66**, 207-211.

Noethe, L. (2000), "Active optics in modern large telescopes", in *Progress in Optics*, VVV, ed. Wolf, E., in press.

Northcott, M. J. (1999), private communication.

Obukhov, A. M. (1949), Izv. Akad. Nauk S.S.S.R., in *Ser Geograf. Geofiz*, **13**, 58.

Ragazzoni R. (1999), "Adaptive optics for giant telescopes: NGS vs. LGS", in *ESO workshop*, **57**, 175.

Ragazzoni, R., Ghedina, A., Baruffolo, A., Marchetti, E., Farinato, J., Niero, T., Crimi, G. and Ghigo, M. (2000), "First adaptive optics compensation of a star by means of a pyramidic wavefront sensor", submitted to *Astronomy &Astrophysics*.

Ragazzoni, R. (1996), "Pupil plane wavefront sensing with an oscillating prism", in *Journal of Modern Optics*, **43**, 289.

Ragazzoni, R. and Farinato, J. (1999), "Sensitivity of a pyramidic wavefront sensor in closed loop adaptive optics", in *Astronomy & Astrophysics*, **350**, 23.

Rajkanan, K., Singh, R., and Shewchun, J. (1979) "Absorption coefficient of silicon for solar cell calculations", in *Solid-State Elec.* Vol. **22**, 793-795.

Riccardi, A. (1996), Degree Thesis, University of Florence, Italy.

Riccardi, A., Bindi, N., Ragazzoni, R., Esposito, S. and Stefanini, P. (1998), "Laboratory characterization of a 'Focault-like' wavefront sensor for adaptive optics", in *SPIE*, **3353**, 941.

Rigaut, F., Ellerbroek, B. L., Northcott, M. J. (1997), "Comparision of curvature-based and Shack-Hartmann-based adaptive optics for the Gemini telescope", in *Applied Optics*, Vol.36, 13.

Roddier, F. J. (1987), "Curvature sensing: a diffraction theory", in *NOAO R&D Note*, No. 87-93.

Roddier, F. J. (1988), "Curvature sensing and compensation: a new concept in adaptive optics", in *Applied Optics*, **27**, 1223-5.

Roddier, F. J. (1999), ed. (with 11 contributors), "Adaptive Optics in Astronomy", Cambridge University Press, Cambridge (UK).

Roddier, F. J. and Rigaut, F. (1999), "The UH-CFHT systems", in *Adaptive Optics in Astronomy*, ed. Roddier, F. J., Cambridge University Press, Cambridge (UK), 205-34.

Roggemann, M. C. and Welsh, B. M. (1996), Imaging through Turbulence, CRC Press, Boca Raton.

Rousset, G. (1999), "Wavefront sensors", in *Adaptive Optics in Astronomy*, ed. Roddier, F.J., Cambridge University Press, Cambridge (UK), 91-130.

Rousset, G. et al. (2000), "Status of the VLT Nasmyths Adaptive Optics System (NAOS)", in the proceedings of the *SPIE's International Symposium on Astronomical Telescopes and Instrumentation 2000, Munich, March 27-31, 2000*, SPIE publications.

Sechaud, M. (1999), "Wavefront compensation devices", in *Adaptive Optics in Astronomy*, ed. Roddier, F.J., Cambridge University Press, Cambridge (UK), 57-91.

Stroebele, S. (2000), "A new machine for planitary measurements of CCDs and mosaics of CCDs", in *ESO workshop on Optical Detectors for Astromony II*, eds. P. Amico, P. and Beletic, J.W., Kluwer Academic Publishers.

Teague, M. R. (1982), "Irradiance Moments: Their Propagation and Use for Unique Phase Retrieval", in *J. Opt. Soc. Am.*, **72**, 1199-1209.

Teague, M. R. (1983), "Deterministic Phase Retrieval: A Greens Function Solution", in *J. Opt. Soc. Am.*, **73**, 1434-1441.

Tulloch, S. (1997), "Design and Use of a Light Source for Linearity Measurement in CCD Cameras", *Royal Greenwich Observatory*, Technical note 111.

Tyson, R. K. (1991), "Principles of adaptive optics", Academic Press, San Diego.

Walden, R. H., Krambeck, R. H., Strain, R. J., McKenna, J., Schryer, H. L. and Smith, G.E. (1972), "The buried channel charge coupled device", in *Bell Syst. Tech. J.*, **51**, 1635-1640.

Wyant, J. C. (1974), "White light extended source shearing interferometer", in *Appl. Opt.*, **13**, 200-202.

Zernike, F. (1934), Physica 1, 689.